이학박사 학위논문

Highly Controlled Synthesis and Optical Properties of Cubic Plasmonic Nanostructures

큐빅 플라즈모닉 나노 구조체의 고도로 제어 된

합성 및 광학 특성

February 2018

서울대학교 대학원

화학부 무기화학

박 정 은

Thesis advisor

Jwa-Min Nam

Author

Jeong-Eun Park

Highly Controlled Synthesis and Optical Properties of Cubic Plasmonic Nanostructures

Abstract

Plasmonics is a field of studying and exploiting extremely confined light using plasmonic materials, based on their strong light-matter interactions. When light is irradiated to a plasmonic nanomaterial with a dimension smaller than the wavelength of the light, the interaction between the metal with a large density of free electrons and light allows a resonant and coherent oscillation of electrons, which is referred as localized surface plasmon resonance (LSPR). LSPR endows plasmonic nanostructures with numerous unique and potent properties. Among many plasmonic metal nanostructures, anisotropic metallic nanocubes are plasmonically and chemically promising. However, gold nanocubes have not been widely utilized mainly due to the lack of methods for fine structural tuning and high-yield synthesis that allow reliable generation of plasmonic properties. For useful employment, high-yield synthesis of plasmonic nanostructures with precise structural controllability is of great importance with their LSPR properties primarily depending on their morphology.

This thesis presents progress in understanding and controlling the synthesis of cubic plasmonic nanostructures, and modulating and/or enhancing their optical properties. I first introduce basics of metal-based plasmonics, a synthesis, and

photoluminescence of plasmonic nanostructures. Next, I present a synthetic strategy to form gold nanocubes with controlled structure (particularly, cube size and corner sharpness) in a very high yield. The strategy is based on fine tuning of surface-protecting agents during shape evolution and following flocculation process to maximize the synthetic yield. Remarkably, single-particle far-field and near-field results show that each of synthesized cubes can scatter light in a highly reproducible and controllable manner. Furthermore, plasmonic cube-in-cube nanoparticles with a controllable interior nanogap were synthesized. They have shown the highest PL intensity and quantum yield ever reported for metallic nanostructures. We proposed the super-radiant mechanism for photoluminescence enhancement of metal nanostructures for the first time and based on the plasmon hybridization theory, the optical properties of the cube-in-cube were analyzed.

Keywords: plasmonics, Au nanocube, corner sharpness, cube-in-cube nanoparticle, photoluminescence, super-radiant

Student Number: 2010-23090

Contents

Citations to Previously Published Work

A portion of Chapter 1 have appeared in or modified from the following paper:

"Non-Noble Metal–Based Plasmonic Nanomaterials: Recent Advances and Future Perspectives", S. Kim[†], J.-M. Kim[†], J.-E. Park[†] and J.-M. Nam, *Advanced Materials,* in press (2017)

"Emerging Plasmonic Nanostructures for Controlling and Enhancing Photoluminescence", J.-E. Park, J. Kim and J.-M. Nam, *Chemical Science* 8, 4696 (2017)

"Golden Opportunities: Plasmonic Gold Nanostructures for Biomedical Applications based on the Second Near-Infrared Window", J.-E. Park[†], M. Kim[†], J.-H. Hwang[†] and J.-M. Nam, *Small Methods* 1, 1600032 (2017)

Most of Chapter 2 have appeared in the following paper and its supplementary online material:

"Ultra-Precisely Synthesized Gold Nanocubes with Single-Particle-Level Reproducibility in Rayleigh and Surface-Enhanced Raman Scattering", J.-E. Park[†], Y. Lee[†] and J.-M. Nam, *submitted* (2017)

And Chapter 3, in its entirety, has appeared in the following paper and its supporting online material:

"Highly Controlled Synthesis and Super-Radiant Photoluminescence of Plasmonic Cube-in-Cube Nanoparticles", J.-E. Park, S. Kim, J. Son, Y. Lee and J.-M. Nam, *Nano Letters* 16, 7962 (2016)

† represents equal contribution.

iv

“ 나는 종종 표류했지만

항상 떠 있었다 ”

Chapter 1

Introduction

1.1. Fundamentals of Metal-Based Plasmonics

Plasmonics has allowed the achievement of numerous applications such as sensing, imaging, theranostics, photocatalysis, metamaterials, nonlinear optics and energy harvesting.[1-12] It would benefit from strong light-matter interactions. When light is radiated to a plasmonic nanomaterial with a dimension smaller than the wavelength of the light, the electric field of incident light pushes large density of free electrons of it. Restoring force between the electric field and an induced dipole pushes electrons to inverse way, generating a collective oscillation of electron gas, known as a plasmon. When the strong, resonant and coherent non-propagating oscillation occurs in a nanoparticle, we called it as localized surface plasmon resonance (LSPR). The oscillating charge decays by emitting the electromagnetic radiation in all directions; this is called as a scattering and scattering consists of charge excitation and re-radiation. When the wavelength of scattered light is same with that of incident one, we call it as Rayleigh scattering whereas the other is Raman scattering. The energy of incident photons can be also transformed into non-radiative one; this corresponds to an absorption. The sum of scattering and absorption is extinction as both remove energy from an electromagnetic wave and attenuate the incident light.

Optical behavior such as scattering from spherical particles can quantitatively be explained by Mie theory that is an analytical solution of Maxwell's equations. Mie theory requires dielectric function of the particle and the surroundings as input parameters. Wavelength-dependent dielectric function describes the ability of material to resist an electric flux, the degree of light-matter

_____

interaction in other words. The dielectric function, $\varepsilon(\omega)$, as a function of the incident light frequency ω, can be represented by a combination of three components: dielectric constant for infinite frequency (ε_∞), intraband transition contribution ($\varepsilon_{intra}(\omega)$), and interband transition contribution ($\varepsilon_{inter}(\omega)$):

$$\varepsilon(\omega) = \varepsilon_\infty + \varepsilon_{intra}(\omega) + \varepsilon_{inter}(\omega) \quad (1)$$

The intraband transition of the metal is an electron transition within the conduction band whereas the interband transition is the electron transition between the valence band and the conduction band. The former can be briefly described by the Drude model, where the conduction electrons are described as a free electron gas, and the latter can be explained by a Lorentz oscillator. Based on these models, the dielectric function can be written as

$$\varepsilon(\omega) = \varepsilon_\infty - \frac{\omega_p^2}{\omega(\omega + i\gamma)} + \frac{G_0\omega_0^2}{\omega_0^2 - \omega^2 - i\Gamma\omega} = \varepsilon_r(\omega) + i\varepsilon_i(\omega) \quad (2)$$

, where ω_p is the Drude plasma frequency, γ is the Drude damping constant, G_0 is the oscillator strength, ω_0 is the resonance frequency, and Γ is the Lorentz damping constant. This can eventually be expressed in a combination of $\varepsilon_r(\omega)$ which corresponds to the real part of the dielectric constant, and $\varepsilon_i(\omega)$ which corresponds to the imaginary part. The real part of the dielectric function represents the degree of metal polarization induced by the external electric field, and the imaginary part of the dielectric function describes the phase shift of this polarization

including the loss and absorption of metal. The losses in intraband transition arise from electron-electron and electron-phonon interactions and from scattering at the defects in solids. The interband transition mainly contributes to the significant losses especially in shorter wavelengths. These losses in metal are detrimental to the efficient plasmonic behavior.

According to the Mie theory, the quasistatic extinction cross-section (C_{ext}) of a spherical particle is given by

$$C_{ext}(\omega) = \frac{12\pi\omega R^3 \varepsilon_m{}^{3/2}}{c} \frac{\varepsilon_i(\omega)}{(\varepsilon_r(\omega)+2\varepsilon_m)^2+\varepsilon_i(\omega)^2} \qquad (3)$$

, where ε_m is the dielectric constant of the medium, c is the speed of light, and R is the particle radius. Thus, the strongest optical extinction of a spherical metal nanoparticle arises at the dipolar resonance condition at $\varepsilon_r(\omega) = -2\varepsilon_m$. The efficient plasmonic extinction of a nanoparticle is generated with large negative $\varepsilon_r(\omega)$ and small $\varepsilon_i(\omega)$ values. The free electrons in metal give rise to the negative real dielectric function that is critical for the plasmonic property. The spectral LSPR position of plasmonic resonance of metal is determined by the real part of the dielectric function, while the imaginary part determines the spectral line width.

As described above, the intrinsic dielectric function of the metal determines the plasmonic and optical properties of nanoparticles. Metal nanoparticles exhibit a negative real dielectric function over a wide frequency range due to containing a large number of free electrons, showing plasmonic responses in UV to near-infrared range. Au exhibits negative $\varepsilon_r(\omega)$ above 480 nm and relatively small $\varepsilon_i(\omega)$

_____

window from 500 nm to 800 nm for exhibiting plasmonic properties. Au suffers from relatively high $\varepsilon_i(\omega)$ at wavelengths below 500 nm due to the occurrence of interband transitions. Ag enables effective plasmonic behavior throughout the visible region because of the negative $\varepsilon_r(\omega)$ and small $\varepsilon_i(\omega)$ values above 320 nm. In this context, Au and Ag can be two representative plasmonic metals with high-quality-factor plasmonic performance in the visible range.

1.2. Synthesis of Plasmonic Nanoparticles

The structure of plasmonic nanoparticle is of paramount importance to exploit plasmonic response since size and shape primarily and significantly affects the LSPR properties. Plasmonic nanostructures using gold and silver allow plentiful ways of forming diverse morphologies because of their readily tunable reduction. One of the representative methods is bottom-up approaches that depend on surfactant-aided metal precursor reduction. The reaction for nanoparticle growth consists of metal precursors, reducing agents, and surfactants. Some reducing agents can act as surfactants at the same time, but usually, a reducing agent with the appropriate reducing power is added separately with the surfactants.

The LaMer mechanism offers insight in nanoparticle growth for homogeneous particle synthesis (Fig. 1.1).[13] According to the mechanism, the entire growth process is composed of three stages depending on the monomer concentration. In stage I, a monomer, which is the smallest subunit of bulk crystals, is dissolved in solution and provided until the concentration reaches supersaturation level. In stage II, after exceeding the supersaturated concentration (C_{min}), the

monomers are given a significant energy to overcome reduction barrier. By the results of the burst nucleation events, small particles, seeds, usually having a size of 1-3 nm are formed and the concentration of monomer goes back below C_{min}. In final stage III, reduced concentration of monomer cannot give further nucleation. When sufficiently stable seeds are present, newly reduced metal atoms are directly deposited onto the seed. During the growth, Ostwald ripening is further processed during growth to allow larger particles to grow further, sacrificing relatively small nanoparticles with higher surface energies due to larger surface-to-volume ratios. The LaMer mechanism describes the seed-less particle growth mechanism, and explains that the burst nucleation is important for homogeneous particle synthesis. Thus, a two-step growth mechanism that separates burst nucleation process and slow particle growth process enables higher degree of structural controllability and/or synthesis of difficult-to-synthesize nanoparticles. Beyond the thermodynamic products, whose growth can be reasonably described by the LaMer plot, kinetic products can be synthesized as well. Although exposed facets of kinetic products are not thermodynamically most stable facet, those facets can be stabilized and favorably exposed with the aid of selective surface protection agents. Usually employment of specific surfactant or halide ions can selectively stabilize specific facet which are thermodynamically unfavorable.

Representative plasmonic Au nanostructures include nanospheres and nanorods. For gold nanospheres, size tunability from 1 nm to tens of nanometer with monodisperse size distribution can be implemented by a successive growth of single-crystal gold nanospheres (Fig.1.2a).[14] A few years ago, highly spherical gold nanospheres can be prepared by a cyclic process of growth followed by oxidative

etching (Fig.1.2b).[15] The oxidative etching selectively removes atoms at edges and/or vertices, yielding ultra-smooth gold nanospheres instead of pseudospherical particles. In case of the nanorods, their anisotropicity allow two distinct LSPR peaks; one from transverse mode in the visible region and the other from longitudinal mode in lower energy region. In particular, the LSPR peak at lower energy red-shifts according to the increase of the aspect ratio, providing flexible tuning of the LSPR throughout the visible to NIR range (Fig.1.3a).[16] Recently, Zhang *et al.* discovered that the facets of gold nanorods can be precisely controlled by the competition between cuprous ions and cetyltrimethylammonium bromide, which serve as surface capping agents (Fig.1.3b).[17] Furthermore, diversiform of polyhedron nanostructure have been developed based on the seed-mediated synthesis according to surface facets and crystallinity (Fig. 1.4).[18] The crystallinity is primarily defined in the initial nucleation stage of particle formation, while exposure of specific types of surface facets occurs during the growth of the particle. By adopting certain conditions, we can choose the synthesis of specific morphology of plasmonic nanoparticles, such as octahedron, cube, and plate. The seed-mediated approach, yet, usually suffers from the intrinsic heterogeneity of pre-formed seed particles, resulting relatively low synthetic yields. Mirkin group solved the problem of initial distribution of seed through iterative reductive growth and oxidative etching reaction. Despite the development of universal gold nanoparticle seed can provide much higher particle uniformity, practical methods for size and shape-controlled high-yield synthesis of plasmonic nanostructures are required.

Another key factor for successful nanostructures synthesis is stabilization of the synthetic products. Nanoparticle with high surface energy tends to

7

agglomerate, which often brings irreversible coalescence since particle aggregation allows lower the surface-to-volume ratio. Thus, particles require a certain protection against agglomeration. The surface energy of nanoparticles is often regulated by the stabilizing agents, which include numerous charged molecules and surfactants; citrate, cetyltrimethylammonium bromide or chloride, and sodium dodecyl sulfate, etc. In electrostatic repulsion-based stabilization, nanoparticles with same charge induced by the surfactant repel each other. However, once the charge balance is broken, such as exposed surface or double charge layers, particles tend to aggregate even with the surfactants. Another approach is based on the steric hindrance, where usually larger and high molecular weight molecules, such as polymers, are employed to physically prevent particle agglomeration.

1.3. Plasmonic Nanostructures for Controlling and Enhancing Photoluminescence

The unique light-matter interaction of plasmonic nanoparticles enables sub-wavelength localization of the electromagnetic field, endowing these nanoparticles with extraordinary properties, including photoluminescence (PL) enhancement ability and photothermal/photocatalytic activity.[8] Among these properties, PL enhancement is particularly interesting, being potentially applicable in photonics and nanobiotechnology.[19-22] Surface-enhanced fluorescence (SEF) denotes a representative phenomenon of plasmon-induced PL enhancement, with the first report of a metal-fluorophore interaction dating back to 1974.[23] Plasmonic nanostructures can efficiently enhance fluorescence by modifying the brightness and

photostability of fluorophores in the near field. These phenomena are ascribed to changes in the emitter radiative decay rate, with decreased emitter lifetime often resulting in enhanced fluorophore photostability and higher photodegradation resistance.[24,25] This coupling of fluorescence enhancement with increased photostability has attracted the attention of researchers from various fields, including the detection of chemical/biological analytes and understanding of microenvironments, offering opportunities to control and enhance fluorescence in an efficient manner. The PL of metals, first observed in 1969 by Mooradian,[26] does not suffer from photoblinking or photobleaching, which distinguishes it from that of organic dyes and quantum dots. However, this phenomenon was rarely studied prior to 2000 due to its low quantum yield and limited understanding. Since then, the PL of plasmonic nanostructures, particularly of nanorods, has attracted increased attention, and its relationship to LSPR has been recognized.

Principle of Surface-enhanced fluorescence

The origin of SEF is the fluorophore-LSPR interaction, with the corresponding energy transfer at short distances being mainly dominated by dipole-dipole interactions, which is known as the Förster resonance energy transfer (FRET) (Fig. 1.5a). When LSPR bands overlap with the fluorophore absorption spectrum, FRET induces enhanced plasmon-to-fluorophore (or vice versa) energy transfer, resulting in a slight increase of fluorescence intensity (the top scheme in Fig. 1.5a). If the LSPR energy matches that of fluorophore emission, FRET results in fluorescence quenching due to the intrinsically large plasmon absorption cross-section, with a typical distance to avoid signal quenching exceeding 5 nm. At longer

distances, the effect of FRET becomes insignificant, since its efficiency decays as $1/r^6$ (where r denotes the plasmon-fluorophore separation distance), resulting in the domination of the Purcell effect, which scales with $1/r^3$ (the bottom scheme in Fig. 1.5a). The Purcell factor, i.e., the enhancement of the spontaneous emission rate of a fluorescent molecule by its environment, originates from the strong local near field, so-called hot spots, generated by neighboring plasmonic nanostructures. Since the local density of optical states (LDOS) is proportional to the square of the local electric field strength, dipoles experiencing a strong local near field can emit more photons in this mode, which corresponds to the wavelength of the LSPR peak maximum. Thus, the fluorescence emission rate is eventually enhanced due to LDOS alteration, and the Purcell effect can be maximized if the LSPR band overlaps with the fluorescence emission band. Notably, the above effect, characterizing the total spontaneous emission rate, involves only radiative decay, explaining why recent studies report the quantum yield as well as the Purcell factor.[27] For an in-depth description of the underlying mechanism, please refer to previously published reviews.[20,28]

Fundamentals of Plasmonic Nanostructure Photoluminescence

When excitation energy is matched with the intrinsic interband transition energy of metals, the above transition occurs, with d-band electrons excited into the sp-band (Fig. 1.5b, pathway (i)).[26,29] For metallic gold, the direct recombination of sp-band electrons with d-band holes preferentially occurs near the L (center of a hexagonal face) and X (center of a square face) symmetry points of the Brillouin zone of its face-centered cubic (fcc) crystal structure, resulting in luminescence at

~510 and ~650 nm, respectively.[30] However, the excited electrons mainly decay via non-radiative relaxation processes such as electron-phonon and phonon-phonon scattering, thereby yielding a very low quantum efficiency (~10^{-10}). Although local field enhancement by a rough metal surface was reported to enhance PL,[31] photoluminescent metal nanoparticles have begun to attract attention only recently. Au nanorods show PL intensities several orders of magnitude higher than those of other metals due to the lightning rod effect, which is interpreted as local field enhancement by mechanisms such as SEF and surface-enhanced Raman scattering (SERS).[32] In particular, Au nanospheres with different maximum scattering wavelengths exhibit PL spectra where the peak positions of PL and scattering shift similarly.[33] Based on these results, one can exclude the previous assumption that PL spectra of plasmonic nanostructures directly reflect the joint density of states of *d*-band holes and *sp*-band electrons, and propose a new mechanism, in which excited *d*-band holes recombine with *sp*-band electrons and excite particle plasmons that subsequently undergo radiative decay (Fig. 1.5b, pathway (ii)). Lithographically defined gold nanostructures such as nanodisks, nanotriangles, and nanorods exhibit shape-dependent PL spectra.[34] Since the direct recombination of *d*-band holes and *sp*-band electrons is affected by material nature and temperature, but not by its shape, a similar mechanism was suggested. When LSPR energy matches that of the interband transition, both this transition and LSPR excitation occur (with the relative contributions of these processes being unknown), and excited plasmons emit light. In some cases, the excitation energy does not overlap with that of the interband transition, which can be rationalized in a number of ways, e.g., by electronic Raman scattering (also denoted as electronic inelastic scattering), which postulates the

11

excitation of an *sp*-band electron to a virtual state with subsequent relaxation (Fig. 1.5b, pathway (iii)).[35-37] Temperature-dependent SERS measurements allowed the anti-Stokes backgrounds in the corresponding spectra to be analyzed, with thermally activated inelastic light scattering proposed as a result. In contrast to wavelength-independent electronic Raman scattering, another model proposes wavelength-dependent intraband transitions of *sp*-band electrons to explain excitation-wavelength-dependent PL spectra (Fig. 1.5b, pathway (iv)).[38] Despite the fact that, unlike inelastic scattering, the intraband transition is forbidden for metal surfaces, it is believed that the breakdown of symmetry and selection rules for momentum in metal nanoparticles allows more efficient intraband recombination. Still plasmons play an important role, helping spatially localize electrons to surface areas around strong near-field regions or out-couple the radiation to the far field.[35] Although the exact underlying mechanism of PL cannot be clarified further, the crucial role of LSPR in plasmonic nanostructure PL has now been recognized. Initially, most studies focused on determining quantum yields of simple nanoparticles or modulating PL spectra by controlling polarization angles or excitation wavelengths. Currently, further investigations of the PL mechanism and plasmon-enhanced PL phenomena are underway.

Engineering the Direct Photoluminescence of Plasmonic Nanostructures

The precise modulation or further enhancement of the direct PL of plasmonic nanostructures is a subject of ongoing debate. Owing to the highly tunable LSPR and the lightning rod effect, Au nanorods are the most widely studied nanoparticles, exhibiting the strong PL with a quantum efficiency of $\sim 10^{-6}$.[38-41]

Therefore, when studying the PL of other nanoparticles, the observed PL intensity is often compared with that of Au nanorods to confirm signal enhancement. The aspect ratio of the rod or the excitation wavelength can also be adjusted to obtain a PL signal of the desired wavelength. Au nanobipyramids show quantum yields one order of magnitude higher than those of Au nanorods, which is attributed to local field enhancement around the sharper ends, supposedly causing a more pronounced lightning rod effect (Fig. 1.6a).[41] In a similar way, the local field enhancement and better PL-LSPR spectral overlap of Au nanocubes were reported to result in PL quantum yields exceeding those of Au nanorods upon irradiation at the same excitation wavelength.[42] PL enhancement has been also studied for plasmonically coupled nanostructures obtained by attaching a single nanostructure to a metal film to form gap plasmons or cavities. When an Au nanoparticle was placed on an Al_2O_3-coated Au film, a significantly increased signal near the gap-plasmon resonance was detected for excitation at 633 nm, as compared to the case when these nanoparticles were absent (Fig. 1.6b).[43] Irradiation at 633 nm efficiently excited the gap plasmon mode, inducing a strong electric field near the particle-substrate junction together with interband absorption near the X point of the Brillouin zone. Hence, this enhancement was explained in terms of cooperation between plasmon-enhanced e−h pair generation and the wavelength-dependent emission rate enhancement. In the same way, although Ag nanowires and Au films exhibit weak PL on their own, their combination (featuring a 6-nm dielectric spacer) resulted in an intensified PL signal.[44] Polarization studies demonstrated that light perpendicularly polarized along the nanowire direction generated stronger PL, with the observed dependence resembling that observed for scattering spectra. Taking into account the similarity

13

between scattering and PL spectra, a PL mechanism featuring radiative damping of gap plasmons was proposed, with the Ag nanowire acting as an efficient antenna for enhanced laser absorption and PL emission. PL enhancement has also been achieved as a result of photon emission by deliberate inelastic tunneling.[45] For instance, upon laser illumination, the small gap between the sharp Au tip and the Au substrate used in scanning tunneling microscopy activates hot electron tunneling to enhance PL. Based on the analysis of the total photon emission profile, the contributions of ordinary light-induced electron-hole recombination and radiative plasmon decay to PL can be distinguished, revealing the dominance of photon emission by hot electrons slightly above the Fermi level via plasmonic modes created by inelastic tunneling.

Some studies have shown that plasmonic coupling has no effect on PL enhancement, or stronger coupling actually decreasing the PL signal. Au nanodimers composed of two nanospheres were prepared, and their PL was compared with that of the monomeric structure. The dimer showed two distinct PL peaks, with wavelengths similar to those observed in the corresponding scattering spectrum, even though the lower-energy peak showed a much higher intensity in the latter case. Interestingly, the increase in the PL signal mirrored the corresponding increase in absorption, and therefore, the quantum yield of the dimer was found to be similar to that of its constituent monomers (Fig. 1.6c).[46] Thus, despite the formation of a strong local electric field between two nanoparticles, a similar quantum yield was obtained for dimeric and monomeric structures, contradicting the results of previous studies that ascribed increased PL to local field enhancement. When the distance between the tips of two Au nanobipyramids was varied using AFM, the scattering signal

intensity increased with decreasing interparticle distance, while the PL intensity concomitantly decreased (Fig. 1.6d).[47] This anticorrelation was interpreted by a theoretical model describing intrinsic *d*-band hole recombination probabilities and the field strength inside nanostructures. The effect of near-field coupling on PL was systematically investigated using sparse arrays of gold nanoparticles with varying size and separation fabricated by electron beam lithography.[48] The emission wavelengths, line shapes, and quantum yields were distinctly dependent on particle size and separation, which was attributed to different LSPR modes. Reduction of the edge-to-edge interparticle separation of 100-nm nanoparticles from 300 to 100 nm decreased PL intensity due to increased non-radiative LSPR losses. Notably, this coupled array system exhibits a much larger coupling distance than systems mentioned earlier. Although coupling strength may affect PL enhancement, the overlap of excitation wavelength with that of the interband transition and LSPR is critical to PL enhancement, necessitating the exploration and verification of this phenomenon under various conditions.[30,33]

1.4. Applications of Plasmonic Nanostructures

The plasmonic nanostructures are employed in a wide variety of fields ranging from nanoantenna, sensing, biomedical applications to catalysis, metamaterials, energy. Among them, chemical or biomedical applications has been extensively explored for several decades. The gold nanoparticles offer a suitable platform especially for biomedical applications owing to their chemical/biological inertness and low cytotoxicity in a variety of cell and animal models. The gold

nanoparticles also exhibit versatile and straightforward surface-functionalization with a wide range of biological ligands such as oligonucleotides, proteins, and antibodies by forming stable bonding pairs such as Au-thiol bonds for specific/selective recognition to biological targets or organs.[49-51] The strong absorption and scattering of light make gold nanoparticles fascinating candidates for biological sensing and imaging applications such as naked eye-based *in vitro* target detection assay[52,53] or SERS-based ultrasensitive imaging systems[54,55]. SEF or PL properties from plasmonic nanostructures can also be used to detect a target of interest. Fluorescence quenching due to the absorption of neighboring plasmonic nanoparticles within proximity and its recovery can be applied to a system that recognizes the existence of target, including ions and biomolecules.[56,57] Signal enhancement can be achieved by bringing the dye close to the nanoparticles, with the presence of targets. While lithographically fabricated systems can be used as substrates or chips for *in vitro* signal enhancement[58], nanoparticles offer the advantages of easy delivery, excellent biocompatibility, and multi-functionality, showing potential for further utilization. As for direct PL, the plasmonic nanostructure itself can act as a label-free sensor. For example, the monitoring of catalytic reactions on the surface of plasmonic nanostructures has been reported at a single-nanoparticle level.[59] Also, biological molecule binding can be efficiently detected based on optical refractive index changes occurring in the vicinity of nanostructures, which induces a shift of PL peak wavelength.[60] The nanostructure such as Au nanocubes, which is known to exhibit relatively strong PL signal, has been utilized as optical labels in cell imaging.[42] Furthermore, the plasmonic property of the gold nanoparticles makes them potential therapeutic agents. Once one excite

the LSPR, gold nanoparticles transfer their absorbed energy to the metallic lattice and the surrounding medium in the form of thermal energy during the plasmon relaxation process, called as the photothermal effect.[61] During the treatment of cancer, the specifically accumulated gold nanoparticles near the cancerous cell generate localized heating under external light irradiation, resulting in cell death.[62,63] Since gold nanoparticles show different pharmacokinetic properties (absorption, distribution, metabolism, and excretion) according to their size, morphology, and surface moieties, they are highly promising materials for *in vivo* studies and customized practical purposes.[64-66]
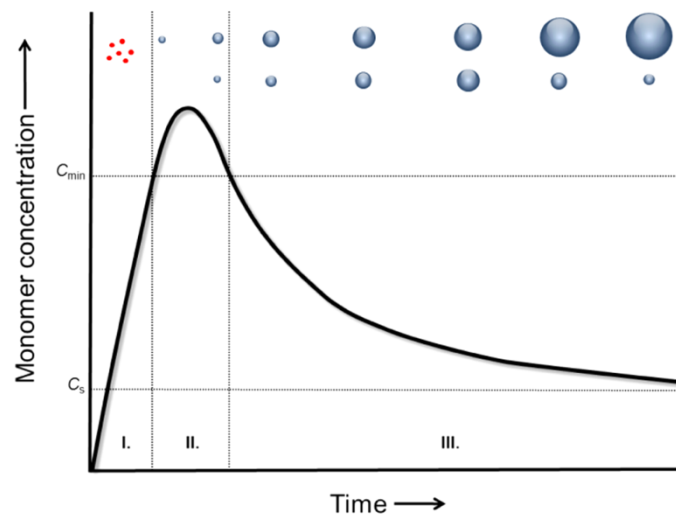
Figures

Figure 1.1. Simplified band diagram of gold showing a possible electronic transition for direct PL.[67]
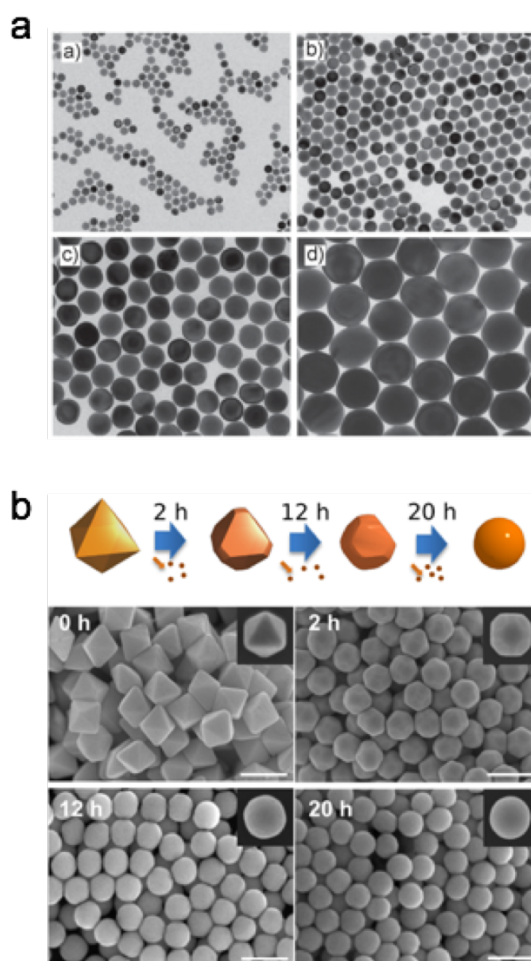
Figure 1.2. Representative examples of gold nanosphere synthesis. (a) gold nanospheres in various sizes[14]; (b) ultra-smooth gold nanosphere by oxidative etching and slow reductive growth[15].
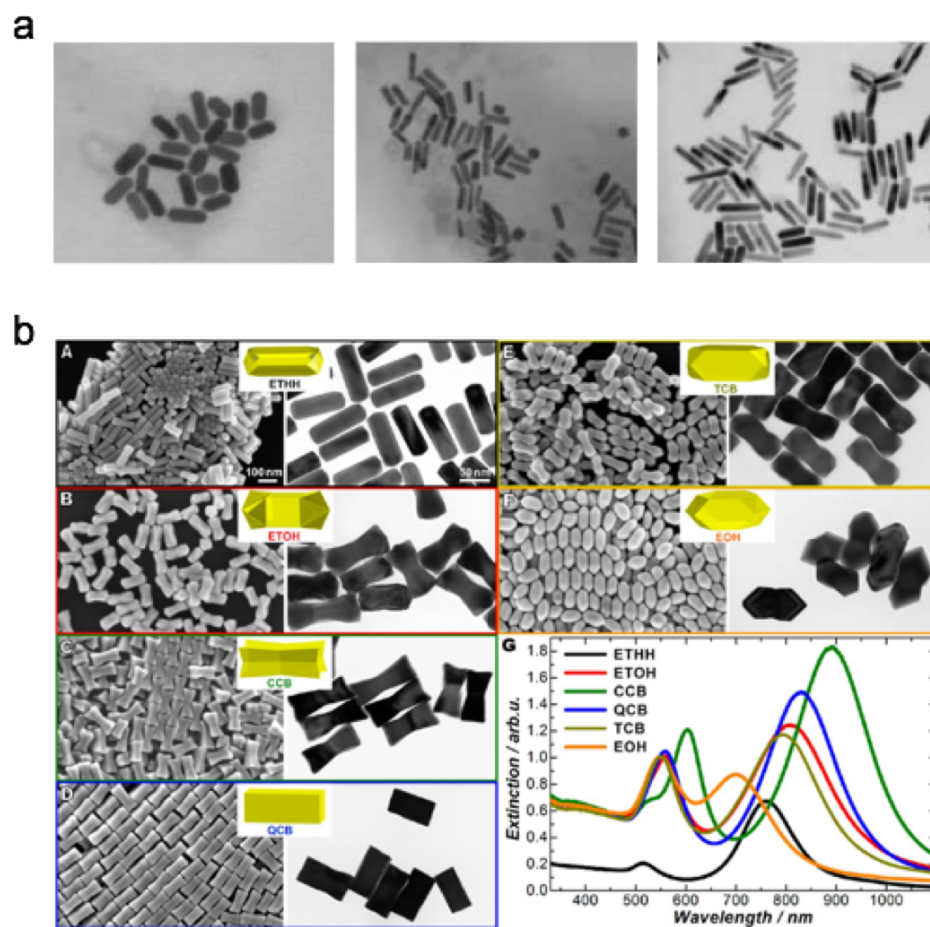
Figure 1.3. Representative examples of gold nanorod synthesis. (a) gold nanorod with varied aspect ratio[16]; (b) facet-controlled gold nanorods[17].
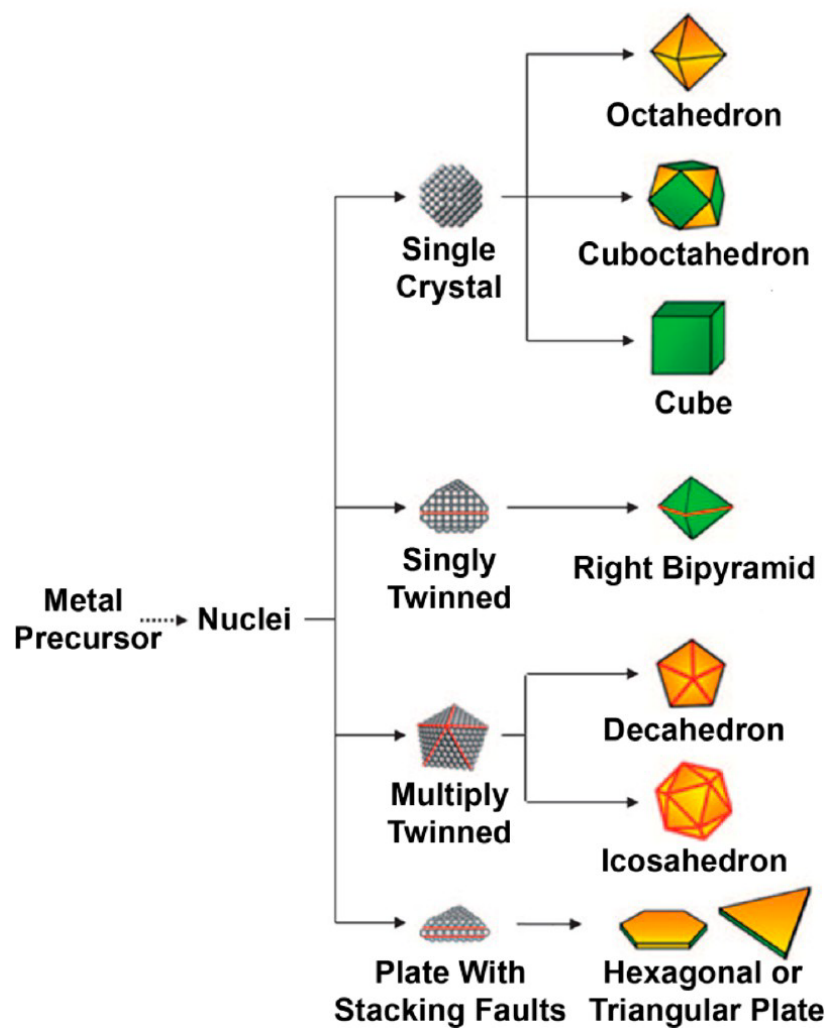
Figure 1.4. Growth of noble-metal nanoparticles with various seeds and surface facets.[18] Yellow and green indicates (111) and (100) surface facets, respectively.
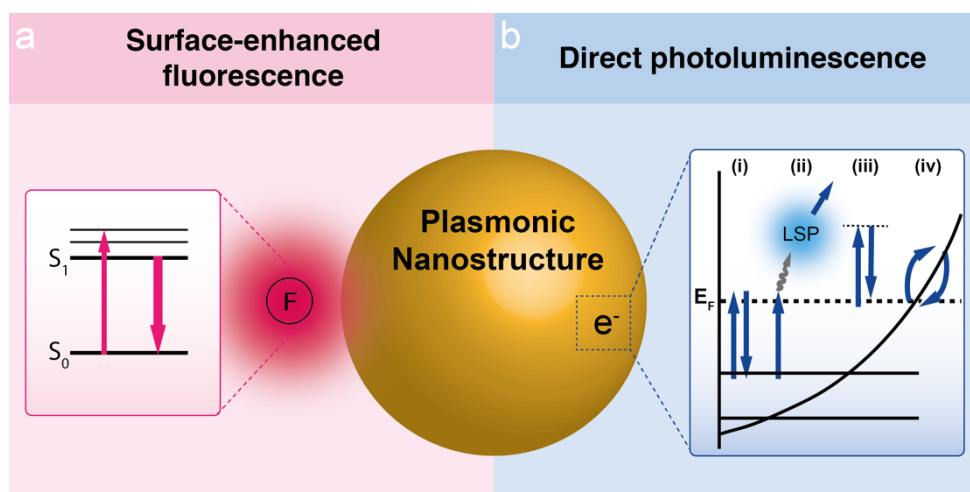
_____

Figure 1.5. Schematic illustration of controlling and enhancing PL with plasmonic nanostructures. (a) Jablonski diagram illustrating fluorescence signal changes when emitters are close to or at a short distance from plasmonic nanoparticles. (b) Simplified band diagram of gold showing a possible electronic transition for direct PL.[68]

_____
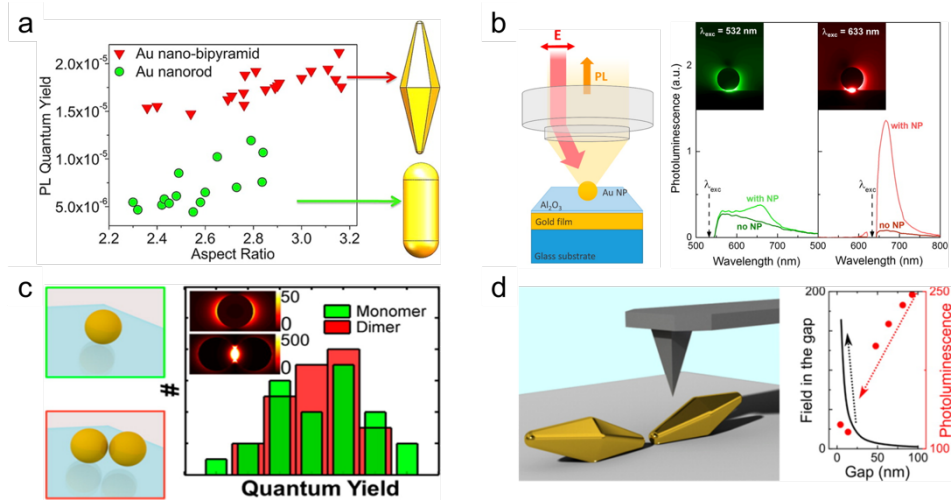
Figure 1.6. Plasmonic nanostructures for direct one-photon PL. (a) Au nanobipyramid and nanorod[41]; (b) Au nanoparticle coupled with Au film with an interstitial Al_2O_3 layer[43]; (c) Au nanoparticle dimer with close tips[46]; (d) Au nanobipyramid dimer assembled edge-to-edge[47].

Chapter 2

Ultra-Precisely Synthesized Gold Nanocubes with Single-Particle-Level Reproducibility in Rayleigh and Surface-Enhanced Raman Scattering

_____

2.1. Introduction

The localized surface plasmon resonance (LSPR) is a unique feature of plasmonic metal nanostructures that enables numerous applications including sensing,[69,70] imaging,[63] therapeutics,[8] nonlinear optics,[71] and catalysis[72-74]. Since LSPR is primarily affected by the size and shape of plasmonic nanostructures, plentiful studies have been conducted on creation of new structures and precise structural controlling strategies. Among many plasmonic metal nanostructures, metallic nanocubes (NCs) have been heavily studied and utilized.[42,75-81] The anisotropy of cubic nanostructures allows different field localization effects according to the morphology. In particular, corners with high curvature generate hot spots with significantly enhanced local field around individual nanoparticles or between coupled nanoparticles, which can be employed in diverse areas including fundamental optics and plasmon-enhanced spectroscopy.[42,75-78,80] Furthermore, owing to its flat surface, it is often used as a building block for assembly or as a template for further synthesis.[79,80] Thus, synthesizing metal NCs with high reproducibility and controllability is of great importance in the field of materials science, optics and nanotechnology. It should be noted that silver nanocubes (AgNCs) have been utilized much more heavily than gold nanocubes (AuNCs) due to their strong and tunable plasmonic properties in the visible region as well as the availability of facile synthetic methods for AgNCs.[82-84] Nevertheless, AuNCs are more beneficial than AgNCs in that they offer better chemical stability, better capabilities in surface modification and conjugation chemistries and better

_____

biocompatibility. Further, AuNCs display different plasmonic properties and cover different spectral regions from AgNCs. However, the synthesis of structurally controlled AuNCs in a high yield is highly challenging, and the use of AuNCs has been limited due to the lack of reliable synthetic strategies. For the synthesis of AuNCs, a seed-mediated growth approach is typically used, but limited structural controllability and reproducibility are major hurdles for wider and more reliable use of these nanostructures. Many existing methods use surfactants as a facet-directing agent, rather than adopting additional facet-directing agents, and it is difficult to form a targeted particle morphology over a large number of particles. The low yield could be partially resolved by universal gold nanoparticle seeds acquired through an iterative oxidative dissolution and re-growth reaction.[85] However, the intricate, laborious and time-consuming seed-preparation process compromises practical synthesis of AuNCs. Further, the accurate control in structural features such as corner sharpness for AuNCs has not been achieved so far.

Here, we report a synthetic strategy to form structurally controlled AuNCs, ranging from 17 to 78 nm in diameter, in a very high yield (98.3 ± 0.7%). The corner sharpness of AuNCs was precisely controlled via anisotropic growth facilitated by the quantitative modulation of surface-feature-selective protection, and the synthetic yield of a targeted cube structure was improved by centrifugation-driven depletion-induced flocculation. Single-particle-level Rayleigh scattering spectrum results show that the synthesized AuNCs generate strong and tunable scattering signals in a highly reproducible and quantifiable manner. Bulk UV−vis spectral analysis for different batches of AuNCs further prove that the optical signals from AuNCs are

_____

quite reproducible over a large number of particles. AuNC dimers with 1.1 ± 0.3-nm gap were formed, and single-particle-level SERS signals were measured from these dimers. Significantly, the polar plots from the dimers are highly symmetric along particle axes, and the average SERS enhancement factor (EF) values from these AuNC dimers were higher than 10^7. Notably, the EFs of sharp-cornered cube dimers are distributed within one-order-of magnitude. The strategy and results in this study open up controllable high-yield synthesis of metal NCs and reproducible, quantitative plasmonically enhanced signals including SERS from metal nanostructures.

2.2. Experimental Section

Materials

Hexadecyltrimethylammonium bromide (CTAB), Benzyldimethyldodecyl-ammonium chloride (BDAC), ascorbic acid, gold chloride trihydrate ($HAuCl_4 \cdot 3H_2O$), sodium bromide, sodium iodide, and 1,4-benzenedithiol (BDT) were purchased from Sigma-Aldrich. Sodium borohydride and sodium chloride were obtained from DaeJung Chemicals & Metals. Hexadecyltrimethylammonium chloride (CTAC) was purchased from Tokyo Chemical Industry (TCI). Deionized water (DIW; Milli-Q, >18.0 MΩ) was used in all experiments. All chemicals were used as received.

Synthesis of 10-nm nanosphere seed

───

CTAC-capped 10-nm gold nanospheres were synthesized according to a known protocol.[14] All solutions were based on DIW. First, we prepared 1-2 nm CTAB-capped seed. To synthesize these seeds, 9.75 mL of 100 mM CTAB solution was mixed with 250 µL of 10 mM $HAuCl_4$ solution inside a 50 mL round-bottom flask. Subsequently, 600 µL of freshly made ice-cold 10 mM $NaBH_4$ solution was added quickly. The solution was mixed with a stirring bar for 3 min and stored at 27 ºC for 3 h before the next step. Next, 10-nm gold nanospheres were synthesized with the aforementioned seeds. 2 mL of 200 mM CTAC, 1.5 mL of 100 mM ascorbic acid, and 50 µL of the previously prepared CTAB-capped seed solution were mixed sequentially inside a 10 mL vial. 2 mL of a 0.5 mM $HAuCl_4$ solution was injected with one shot while the solution was being mixed with constant speed. The solution was incubated at room temperature for 15 min with constant mixing at 300 rpm. It was centrifuged twice, first redispersed in 1 mL DIW and then in 1 mL of a 20 mM CTAC solution for future use (20600 g, 30 min).

NC synthesis

The synthesis was performed in 20 mL glass vials. The vials were cleaned with acetone and DIW before use. 6 mL of 100 mM CTAC was mixed with 30 µL of sodium bromide with the appropriate concentration (described below). The previously prepared 10-nm seed solution was diluted to 5.6 O.D., and a defined volume was added (described below). 390 µL of a 10 mM ascorbic acid solution was added and mixed thoroughly. Finally, 6 mL of a 0.5 mM $HAuCl_4$ solution was added

with one shot while the solution was being mixed with a stirring bar at 500 rpm. The solution was incubated for 25 min with mixing, followed by centrifugation and redispersion in DIW twice, respectively.

Sample	Seed volume	Bromide concentration
18R	300 μL	20 mM
17S	300 μL	120 mM
37R	30 μL	2 mM
32S	30 μL	40 mM
41R	9 μL	5 mM
41S	9 μL	20 mM
54R	6 μL	6 mM
53S	6 μL	20 mM
78R	2 μL	2 mM
/72S	2 μL	13 mM

The effect of halides on AuNC synthesis

Overall procedures were same as described in NC synthesis. Seed volume was kept constant, while 20 mM of NaCl, NaBr and NaI were used, respectively.

NCs with varied corner sharpness

Overall procedures were same as described in NC synthesis. Seed volume was fixed to 6 μL, while bromide concentration was varied (0, 1, 40, and 200 mM).

_____

NC refinement

The synthesized nanocubes were precipitated by centrifugation (Eppendorf, eppendorf 5424, Germany). It was redispersed in a 10 mM CTAB solution. The calculated amount of the stock solution of BDAC and DIW was added to make the appropriate final BDAC concentration for each sample with a volume that is twice the volume of NC solution, making final CTAB concentration as 5 mM (described above). DIW was added first to prevent unwanted flocculation. The solution was mixed and centrifuged according to the appropriate condition. Since 18R and 17S were too small to be flocculated, they were excluded from purification. 37R and 32R were centrifuged at 1000 g for 10 min. Other samples were centrifuged at 500 g for 5 min. The supernatants were removed with a micropipette, and the remaining sediments were redispersed in DIW. *32S AuNCs have flocculation potentials similar to those of their byproducts, providing relatively lower yields of ~90%.

Sample	BDAC concentration	Yield (n > 400)
18R	N.A.	-
17S	N.A.	-
37R	100 mM	98.0%
32S*	60 mM	90.0%*
41R	60 mM	99.5%
41S	50 mM	98.4%
54R	40 mM	98.0%
53S	32 mM	97.2%

_____

78R	24 mM	99.0%
72S	17 mM	98.2%

Size analysis

All particle sizes were analyzed with ImageJ software from the TEM image. Edge length and corner radius of 100 particles were measured for each AuNC.

DF measurement (image and spectrum)

Dark-field (DF) images were taken with a 40× objective. 78R and 72S AuNCs had an exposure time of 80 ms, while 41R AuNCs had an exposure time of 120 ms. DF spectra were obtained using an inverted microscopy system (Ntegra, NT-MDT). An oil condenser with NA 1.3 was used for DF measurements. An air objective (UNPLAN,60x, NA 0.90) was used to obtain scattering spectra. Cleaned glass was prepared by sonication in acetone and DIW for 5 min each. The samples were prepared by drop casting AuNCs on cleaned glass and spin coating with a microcentrifuge. The prepared glass samples were rinsed with DIW and ethanol afterwards to remove extra surfactants. Spectra were acquired from randomly selected particles observed in DF with an exposure time of 3 s in the case of 54R, 53S, 78R, and 72S samples and 20 s in case of 41R and 41S samples. The latter were normalized to the 3-s case under the assumption that the signals increase linearly with exposure time.

_____

Dimer sample preparation

First, we prepared purified 78R and 72S AuNCs dispersed in 0.1 mM CTAB and 20 mM 1,4-benzenedithiol (BDT) dissolved in EtOH, separately. Then, 1 μL of BDT was added to 19 μL of AuNC solutions, following which it was incubated for 30 min with mixing. After centrifuging it at 5000 rpm for 3 min, pellets were redispersed with DIW. 1.5 μL of the sample was loaded on a silicon-dioxide support film (Tedpella, 21530-10) and dried. Finally, we washed the grid with EtOH to remove excess BDT. The dimer position was mapped with TEM at a low magnification (×6000). After measuring the Raman signal, we additionally acquired high-magnification images of dimers. Only face-to-face dimers with uniform <2-nm gap were analyzed.

Raman measurement

Raman measurements were conducted using an inverted microscopy system (Ntegra, NT-MDT) and objective lens (UNPLAN,100×, NA 1.3, oil). Nanoparticles were identified by correlation of the Rayleigh scattering image with the TEM image. Each Raman signal was acquired by exposure on linearly polarized 785-nm lasers (230 μW) for 30 s. The signals were detected by a charge-coupled device (CCD) cooled to -70 ºC (Andor Newton DU920P BEX2-DD). Enhancement factor was calculated by comparing signals from 2.5 mM BDT bulk solution in 6 M NaOH with low magnification objective lens (Olympus, 10×, NA 0.25, air), as we could not detect Raman signal from bulk BDT with the objective lens we used (Olympus, 100×, NA 1.4, oil). The spectra were acquired by exposure to a linearly polarized

_____

785-nm laser (17.6 mW) for 180 s. To compare the signal intensity between two lenses, we obtained Raman signals of 1 mM Rhodamine 6G with both lenses and converted the signal with 10x on the assumption that the ratio of two measurements to be same with the case of BDT. The bulk signal was then normalized on the assumption that the Raman signal is proportional to the laser power and acquisition time. Spot size was measured carefully by using knife-edge method with silicon wafer. The focal volume is assumed to be cylindrical and calculated to be 28 fL. One BDT molecule on gold is assumed to have a volume of 4.1×10^{-28} m^3, calculated from a height of SAM layer, 7.6×10^{-19} m and a molecular footprint, 5.4×10^{-19} m^2.[86,87] Hot spot volume was defined in the form of box, having area of the flat surface of AuNC and height of the gap distance. Number of the molecules in gap were obtained by dividing hot spot volume by the calculated volume of one BDT molecule. The enhancement factor is calculated using the following equation:

$$EF = \frac{I_{SERS} N_{Bulk}}{I_{Bulk} N_{Gap}}.$$

Simulations

Finite-element method (FEM) simulations were conducted using commercial software (COMSOL) in the scattered-field mode. Linearly polarized plane-wave excitation was used. The AuNC dimer model was based on TEM image analysis. The gap between the cube structures was 1.1 nm. Both cubes were modeled as gold. The surrounding medium, including the gap, was modelled in air.

───

Instruments

TEM and SEM images were obtained by JEM-2100 (JEOL) and Helios NanoLab 650 (FEI) systems, respectively, at the National Center for Inter-University Research Facilities (NCIRF), Korea.

2.3. Results and Discussion

In a typical experiment, first, we performed selective surface-protection-directed anisotropic growth of AuNCs (Fig. 2.1a). The morphology of nanocrystals is determined by the ratio between growth rates of different facets. In order to induce an anisotropic growth of cubic nanostructures, the growth rate along [100] needs to be reduced while manipulating the rates along [110] and [111] to be higher. For facet-dependent protection, we introduced bromide ions which are favorably adsorbed on the (100) facet.[88] The adsorption of bromide ions on Au surface induces the density of CTA^+ passivation ions, stemming from cetyltrimethylammonium chloride (CTAC), to be higher on (100) than (111)/(110).[89] Given the different density of passivation molecules on each facet, the difference in accessibility of Au precursors induces the growth-rate difference between (100) and the other facets, resulting in AuNCs.[89] In this step, the bromide concentration-controlled growth kinetics governs the corner sharpness of AuNCs (Fig. 2.1b). Utilization of two different reagents, CTAC and NaBr, enables precise modulation of the growth rate of each facet, and allows for the precise adjustment of the amount of bromide ion as surface-directing agent at a fixed amount of CTA^+. At the bromide densities less than ~100 ions/nm^2,

_____

the number of adsorbed bromide ions is insufficient to block the (100) facet

completely. Hence, the relative growth-rate difference between [100] and [111]/[110]

is not significantly changed, producing round-cornered AuNCs. When a sufficient

number of facet-directing agents (~300 ions/nm^2) is provided, effective and

preferential binding to the (100) facet decreases the reduction rate, while the

(111)/(110) facet are less affected by bromide ions, maximizing the growth-rate

difference between [100] and the other two facets. Consequently, sharp-cornered

AuNCs are produced. If the bromide concentration is excessive, bromide ions can

be additionally adsorbed on (111)/(110) surfaces as well as (100), decreasing the

overall growth rate and rate difference between facets. The possibility of reduction

rate change due to ligand exchange of Au-halide complexes is excluded, based on

the result of absorption spectra (Fig. 2.2). As the ratio of chloride to bromide was

very high, ranging from 200: 1 to 10000:1, the amount of halide ligand exchange

from chloride to bromide was minimal, showing no noticeable changes in the

spectrum. The effect of other halide ions was also studied (Fig. 2.3), demonstrating

bromide ions are proper surface-protecting agents for controlled AuNC synthesis.

We then employed the shape-selective refinement strategy to maximize the

synthetic yields for AuNCs (Fig. 2.1c). The method is based on centrifugation-driven

depletion-induced flocculation, which consists of the flocculation of AuNCs using

surfactant micelles and reversible redispersion of the sediment. When particles are

dispersed in the surfactant solution above the critical micelle concentration, the

exclusion of micelle molecules from the space between AuNCs results in an osmotic

pressure, inducing inter-particle flocculation. The flocculation has been applied to

───

select nanorods or nanobipyramids among mixtures of nanoparticles and typically takes more than 10 h to make nanoparticles settle down.[90-92] In this study, we dramatically shortened the time by adopting a brief centrifugation step. After centrifuging the nanoparticles in the surfactant micelle solution, effective flocculation can occur with a relatively low depletion potential in a very short time (Note 1). During the centrifugation, centrifugal force pushes particles close to each other, giving extra driving force to flocculation. Since the attractive force between two particles is proportional to the surface areas facing each other, AuNCs with flat surfaces are advantageous compared to those with curved surfaces, such as rods, spheres and bipyramids. In this fashion, we achieved the synthetic yield for AuNCs of >97% by adjusting the micelle concentration to induce AuNC flocculation selectively.

Next, we obtained similarly sized AuNCs with different corner sharpnesses (Fig. 2.4a and Fig. 2.5). While the amounts of CTAC, seed, precursor and ascorbic acid were kept constant, the bromide concentration was varied from 0 to 200 mM. To characterize the structural features of each AuNC based on the transmission electron microscopy (TEM) images, we defined the edge length as the distance between the two closest faces of AuNCs and the corner radius as the radius of the circle that perfectly matches the corner curvature. We coined a term called corner sharpness index (CSI) to characterize corner sharpness quantitatively (Fig. 2.4b). Sharper NCs have CSI values closer to 1. As shown in Fig. 2.4c, the corner sharpness initially increased and then decreased with increasing bromide concentration. This could be explained by the growth rate changes through adsorbed bromides on each

_____

facet, as illustrated in Fig. 2.1a. To investigate the mechanism of corner-sharpness control, we explored the growth kinetics during shape evolution by UV−vis spectroscopy with three selected bromide concentrations (1, 40 and 200 mM). After adding Au precursors, we started to monitor the changes in extinction intensity at 10-s intervals at each maximum LSPR wavelength of the fully-grown structures (Fig. 2.4d). The slowest increase of extinction for 200 mM NaBr suggests that increasing the bromide concentration slows the reduction, supporting the synthesis mechanism proposed in Fig. 2.1a. While other synthetic methods for AuNCs usually employ cetyltrimethylammonium bromide (CTAB), a reagent containing equal amounts of two components that function as surface stabilizers and selective facet-directing agents, our method induces anisotropic AuNC growth with an excessive amount of CTA^+ from CTAC and a small amount of bromide ions from NaBr. As we utilized two different reagents, precise modulation of direct surface-protecting agent bromide is possible with a sufficient amount of CTA^+ passivation ions (Fig. 2.6).

To substantiate the above principles, we adopted the simultaneous control of size and corner sharpness by changing the amounts of seed and bromide. The seed amount was adjusted by controlling the volume of seed solution (300, 30, 9, 6, and 2 μL). We also varied the bromide concentration to control the corner sharpness at a fixed seed amount. Following preparation, the AuNCs were dispersed in a mixture of benzyldimethyldodecylammonium chloride (BDAC) and small amount of CTAB solution and centrifuged for 5 min at 500 g. Since BDAC allows effective flocculation at a much lower concentration compared to CTAB because of the lower critical micelle concentration and lower number of surfactant molecules required to

_____

form a micelle, BDAC is more suitable to induce flocculation.[90] Based on the results obtained with varied flocculation conditions, we determined the optimum surfactant concentration for each NC size (Fig. 2.7 and Note 1). Since flocculation force has a positive correlation with the overlaid surface area between nanoparticles as well as the micelle concentration, the surfactant concentration required for flocculation decreases as AuNCs become larger. Fig. 2.8a show different sizes of refined AuNCs, and the insets show representative images for clear visualization of representative structures. Each column represents the result of adjusting the seed amount, and top and bottom rows correspond to round-cornered and sharp-cornered AuNCs, respectively. With decreasing the seed volume, the edge length increased from 17 to 78 nm (Fig. 2.9 and Table 1). The numbers in the labels indicate the edge length, and R and S correspond to round-cornered and sharp-cornered NCs, respectively. After refinement, the yield was improved to > 97% for all the AuNCs except the smallest two NCs and 32S (n > 400, Fig. 2.8b and Fig. 2.10 for larger scanning electron microscopy (SEM) images). It is more difficult to determine an appropriate surfactant condition to make smaller particles flocculated owing to their low surface area. Synthesizing AuNCs smaller than 25 nm by solution-based methods is challenging and has not been achieved nor reported before, because the self-diffusion distance of gold atoms (3−12 nm) is higher than those of other metals such as platinum (0.3−1 nm), inhibiting the effective exposure of flat faces by promoting the movement of gold adatoms from the corner of higher energy to face of lower energy.[93] Here, we successfully synthesized AuNCs with an edge length of 17−18 nm using our method. To our knowledge, this is the smallest size reported so far for

───

AuNCs. 32S AuNCs have flocculation potentials similar to those of their byproducts, providing relatively low yields of ~90%. While the CSI values of four large, sharp-cornered AuNCs are similar, that of 17S was lower than others (Fig. 2.11a), which can be mainly attributable to the high surface tension that prohibits smaller corner radius. To provide stoichiometric information for sharp-cornered AuNCs, we calculated the number of bromide ions required per AuNC (Fig. 2.11b). It is worth mentioning that this is not the number of ions adsorbed on the surface but rather the number of ions we added. The linear relationship between surface area and the number of added bromide ions reveals a uniform density of bromide ions of 305 ions/nm^2 regardless of size. Once the size of NCs is determined by the seed volume, one can readily estimate the required amount of bromide ion for the sharp-cornered or round-cornered NCs. Normalized UV−vis spectra for a series of AuNC solutions show a gradual red-shift as the corner sharpens and as the edge length increases, owing to the retardation effect (Fig. 2.11c). Narrower spectral linewidth and removal of shoulder peak at ~800 nm after refinement imply highly monodisperse AuNCs (Fig. 2.12). Finally, we discovered the extraordinary reproducibility of the AuNCs by synthesizing 9 different batches of 53S AuNCs and comparing their ensemble extinction spectra (Fig. 2.11d). The spectral information including the maximum peak position and linewidth suggest negligible batch-to-batch variations in the synthesized AuNCs.

Next, we explored the fine tunability and reproducibility in the optical signals of the AuNC structures. We measured the Rayleigh scattering signal at the single-particle level from individual particles using dark-field (DF) microscopy

───

(Ntegra, ND-MDT, Russia). The scattering properties of 18R, 17S, 37R, and 32S AuNCs could not be clearly measured owing to the low signal intensity caused by their small volume. The DF micrographs of six different AuNCs exhibit a uniform scattering intensity for each sample, and scattering colors were green, except for 78R and 72S AuNCs, which showed yellow color of scattering (Fig. 2.13a). The single-particle scattering spectra were then obtained from 25 different single AuNCs for each case. Remarkably, highly consistent spectra were obtained, reminiscent of the narrow size and shape distribution of the synthesized AuNCs (Fig. 2.13b). The representative spectrum of each sample is marked with a dotted box in Fig. 2.14. As the corner becomes sharper between AuNCs of similar sizes and the size increases, the average peak wavelength was red-shifted, which is mainly attributable to the retardation effect[94], along with increase in scattering intensity (Fig. 2.13c and 2.13d). The 72S AuNCs showed a slightly lower scattering intensity compared to that of 78R AuNCs owing to the increased radiative decay for the larger NCs, as the light scattering scales with the square of the particle volume in general. Notably, although the average peak position of 78R was 562 nm as in the 53S case, an increased contribution from wavelengths greater than 600 nm results in a distinct color difference in the micrograph, as shown in Fig. 2.13a. Analyzed spectral linewidths also manifest the uniform Rayleigh scattering property (Fig. 2.13e). When reference AuNCs synthesized according to the previously reported method[93] were compared to our AuNCs of a similar scattering intensity, our AuNCs showed linewidths with smaller deviations, implying the high homogeneity in particle structures synthesized with our method (Fig. 2.15).

40

───

To analyze the structural effect on near-field enhancement, particularly for plasmonically coupled nanostructures, we observed the SERS signal from AuNC dimers with two differently cornered AuNCs, 78R and 72S, respectively (Fig. 2.16a). 1,4-Benzenedithiol (BDT) was used as linker molecules to assemble the NCs. Fig. 2.16c shows two representative TEM images of dimers made from 78R and 72S AuNCs. From the analysis of 22 different dimers for each case, the average gap size was obtained as 1.1 ± 0.3 nm (Fig. 2.17). The polar plot of Raman signal from the BDT for incident laser polarization reveals that the maximum Raman enhancement occurs at the longitudinal mode of dimers (Fig. 2.16d). It should be noted that the assembled dimers generated highly symmetrical polar plot results, suggesting that the dimers were formed impeccably and symmetrically. The EF of 78R dimer is obtained as $\sim 8.0 \times 10^7$, while that of 72S is $\sim 1.6 \times 10^7$ (Fig. 2.16e and 2.16f). This trend is consistent with the electromagnetic-field simulation results (Fig. 2.16b). In this manner, the control of corner sharpness can be employed as one of the strategies for tuning the optical properties in assembled structures and not only in single particles. It is believed that the EF of $\sim 10^7$ is strong enough for single-molecule detection experiments.[95] Significantly, a very narrow distribution of SERS EFs was acquired with both 78R and 72S cube dimers (Fig. 2.16f and 2.16g). The SERS EFs for the entire dimers that we analyzed are very narrowly distributed and ranged from 1.6×10^7 to 3.1×10^8 for 78R cube dimers and from 5.4×10^6 to 4.9×10^7 for 72S cube dimers. It should be noted that the SERS EFs are distributed within one order of magnitude for the 72S cube dimer case. This is a remarkable advance in SERS, considering that uniformly formed Ag nanosphere arrays generated the SERS EF

───

values, widely distributed between 2.8×10^4 and 4.1×10^{10}.[96] The SERS EF values from 90% of single Au nanoparticles with ~1-nm interior gap are distributed from 1.0×10^8 to $> 1.0 \times 10^{10}$.[97] The results obtained in this study are remarkable considering the plasmonic coupling here is based on plasmonically coupled particles with an interparticle gap, and interparticle gaps between nanoparticles often generate highly uncontrollable hot spots and widely distributed EF values. Our NC dimer-based SERS EF results are reminiscent of ultra-high uniformity of AuNC structures, and can be also attributed to uniformly distributed electromagnetic field between AuNCs, particularly for sharp-cornered 72S cube dimers (Fig. 2.16g). A larger surface area for 72S cube dimers than 78R cube dimers that can form more uniform interfaces between particles and the smaller standard deviation of corner radius of 72S can lead to a higher homogeneity in SERS signals.

2.4. Conclusion

We have developed a straightforward, generally applicable synthetic strategy, based on particle surface modification chemistry and centrifugation-driven flocculation, to precisely control the size and shape of AuNCs and synthesize AuNCs with varying corner shapes, ranging from 17 to 78 nm in diameter, in a very high yield (~98-99%). The growth kinetics of the different facets of AuNCs was precisely controlled via the quantitative modulation of surface-feature-selective protection. Preferential bindings of bromide ions to (100) facets induce difference in growth rate between multiple facets, yielding sharp-cornered or round-cornered NCs in a highly

_____

selective manner. The ultrahigh structural precision for cube size and corner sharpness and > 98% synthetic yield enable the fine-tuning of plasmonic optical responses from AuNCs, allowing single-particle-level optical signal reproducibility over a large number of particles. Remarkably, single-particle SERS analysis for the AuNC dimers shows that a very narrow distribution of large SERS EF values can be obtained - all of the EFs for sharp-cornered AuNC dimers are distributed within one order magnitude! This could finally open the door to reliable, quantifiable SERS signal analysis and practical applications with metal nanostructures. We expect our work to lead to the development of practical and scalable synthetic methods for AuNCs and other cube structures with the potential for use as basic seeds for complex structures and building blocks for assembly as 1D, 2D or 3D materials with highly controlled structural features. Importantly, our rigorous single-particle-level optical signal analysis results for a large number of AuNCs and AuNC dimers suggest that our method and AuNCs open revenues for highly reliable surface-enhanced spectroscopic applications including SERS with high sensitivity and quantification capability in a controllable and predictable manner, which have been major hurdles for the wide and practical applications of nanostructure-based surface-enhanced spectroscopies.

Figures

a **Selective surface-protection-directed anisotropic growth of Au nanocube**

b **Bromide concentration dependent corner sharpness control of Au nanocube**

c **Au nanocube refinement by centrifugation-driven depletion-induced flocculation**
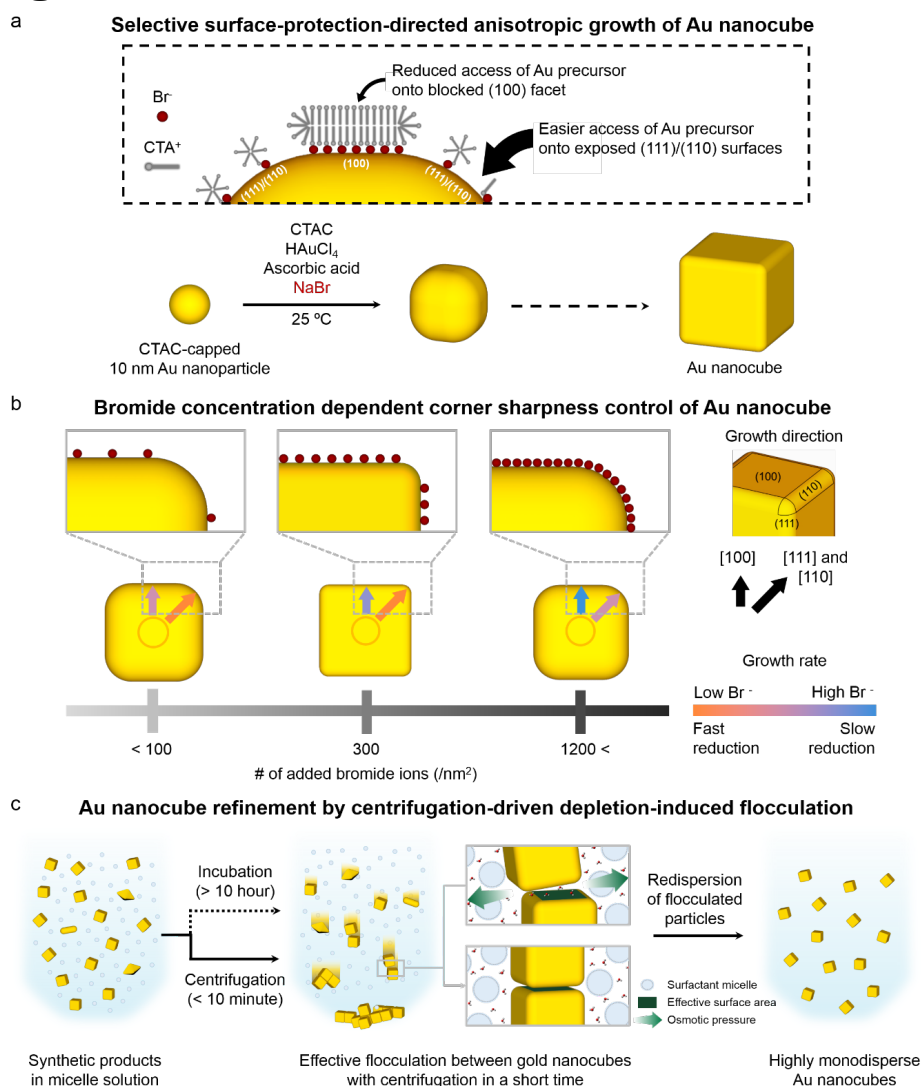
Figure 2.1. Synthesis and refinement of size and shape-controlled AuNCs. (a) Selective surface-protection-directed anisotropic growth of AuNC. The inset illustrates the difference in the Au reduction rate due to the difference in absorption of Br⁻ and CTA⁺. (b) Corner sharpness-controlled AuNCs with varied bromide densities. The proposed mechanism of modifying growth kinetics is based on the preferential adsorption of bromide ions on the (100) facet of AuNC. For clearness, the CTA⁺ layer is omitted. (c) Synthesized AuNC refinement by centrifugation-driven depletion-induced flocculation in surfactant micelle solutions and subsequent redispersion in DIW. Inset images show the attractive osmotic pressure between AuNCs, resulting in the flocculation.

_____
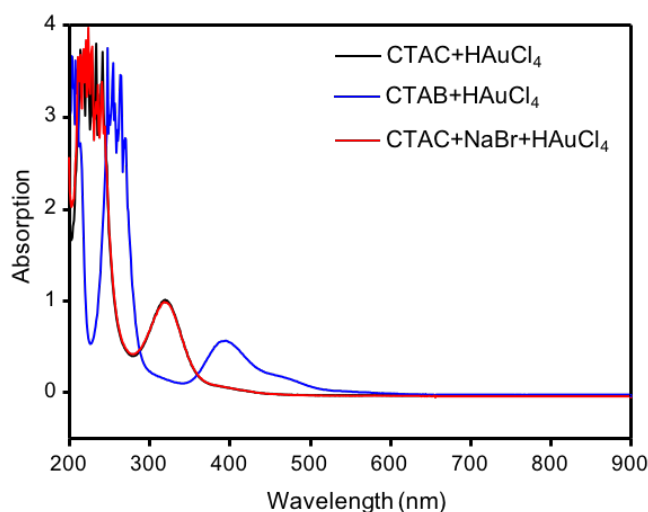
Figure 2.2. Absorption spectra of Au-halide complexes. The halide ions in a growth solution control the reduction rate by formation of Au−halide complex, modulating reduction potential, and by adsorption onto the surface of nanoparticles.[18] No spectral changes were shown in adding 10 μL of 10 mM Br⁻ to 4mL mixture containing 0.25 mM HAuCl₄ and 0.05 mM CTAC. Based on this result, the reduction rate changes originating from the halide ligand exchange (from chloride ion to bromide ion) was negligible. Therefore, we conclude that the main role of bromide ions is surface-directing agents.
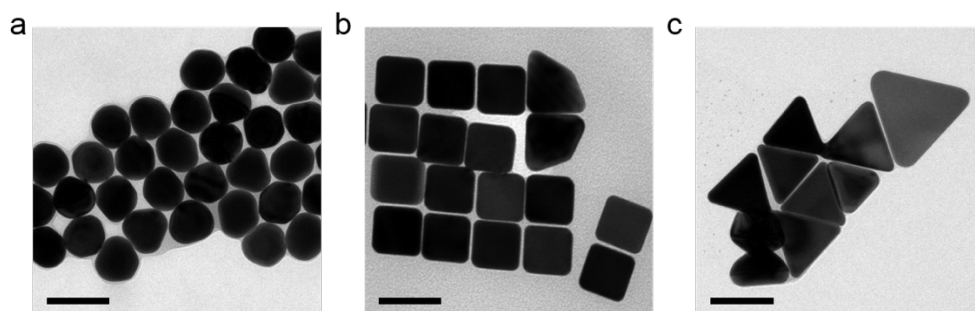
Figure 2.3. The effect of halides in AuNC synthesis. TEM image of nanoparticles synthesized by using same amount (20 mM, 10 μL) of (a) NaCl (b) NaBr (c) NaI. The scale bars in (a)-(c) indicate 100 nm.
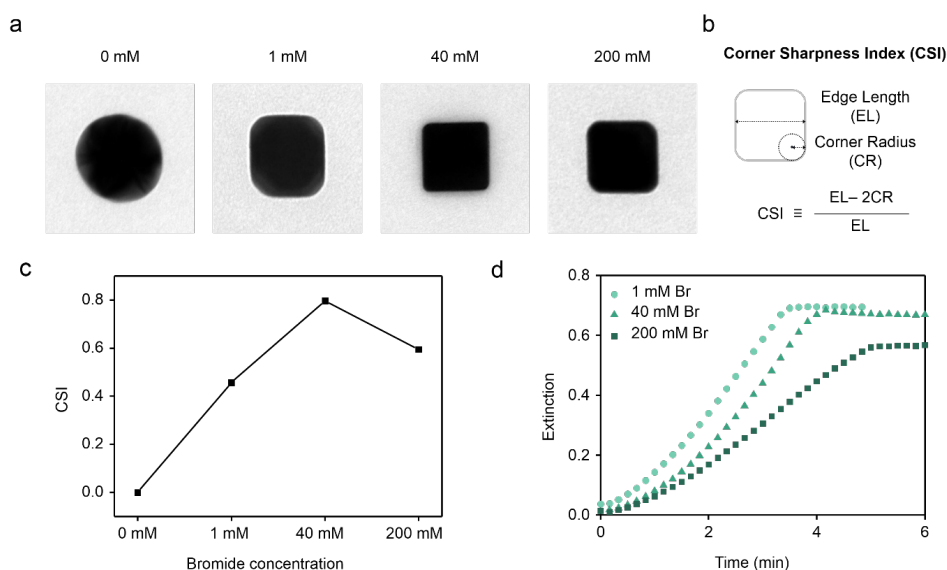
Figure 2.4. Corner sharpness control by bromide concentration. (a) Representative TEM images of AuNCs obtained by adjusting the concentration of bromide from 0 to 200 mM at the fixed amounts of seed and gold precursor. (b) Bromide-concentration-dependent growth kinetics. The results were obtained at each maximum LSPR wavelength using a UV−vis spectrophotometer. (c) Definition of edge length, corner radius, and corner sharpness index (CSI). (d) CSI value changes of AuNCs in varied bromide concentrations.
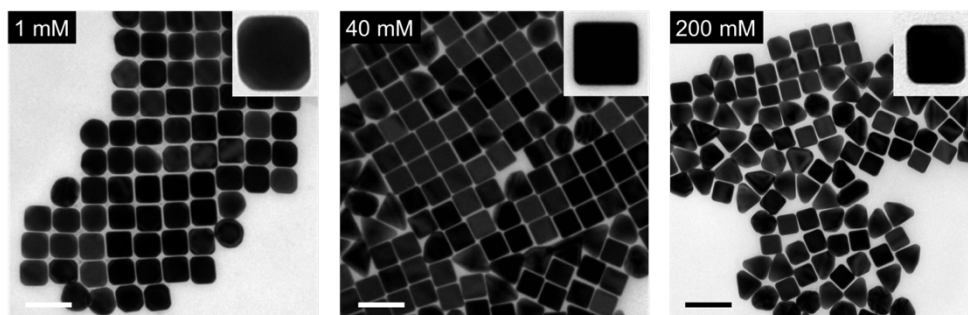
Figure 2.5. Sharpness control by bromide concentration. TEM images corresponding to AuNCs before refinement with a bromide concentration of 1, 40, and 200 mM from left to right, respectively. The scale bars indicate 100 nm.

a CTAC with NaBr

b Same CTA⁺ concentration by CTAB

c Same Br⁻ concentration by CTAB

100 mM CTAC 6 mL
+ 20 mM NaBr 30 μL

100 mM CTAB 6 mL
+ DIW 30 μL

DIW 6 mL
+ 20 mM CTAB 30 μL
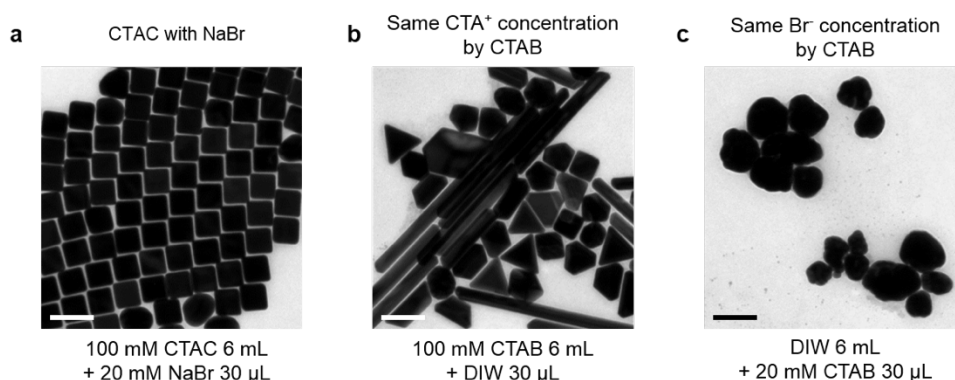
Figure 2.6. Comparison with conditions only using CTAB. (a) TEM image of nanoparticles synthesized by using CTAC and NaBr with our optimized condition, (b) using only CTAB in same concentration with CTAC in (a), and (c) using only CTAB in same concentration with NaBr in (a). The scale bars in (a)-(c) indicate 100 nm. If we match the concentration of CTAB with that of CTA^+, the bromide-ion concentration becomes excessively high. This results in poor selectivity to cube structures, creating many byproducts such as nanorods and nanoprisms. If we match the concentration of CTAB with that of Br^-, the concentration of CTA^+ becomes excessively low compared to our original condition. In this case, in addition to growth on the seed surface, direct self-nucleation occurs in solution. Consequently, irregular structures with undefined facets of different sizes are created.
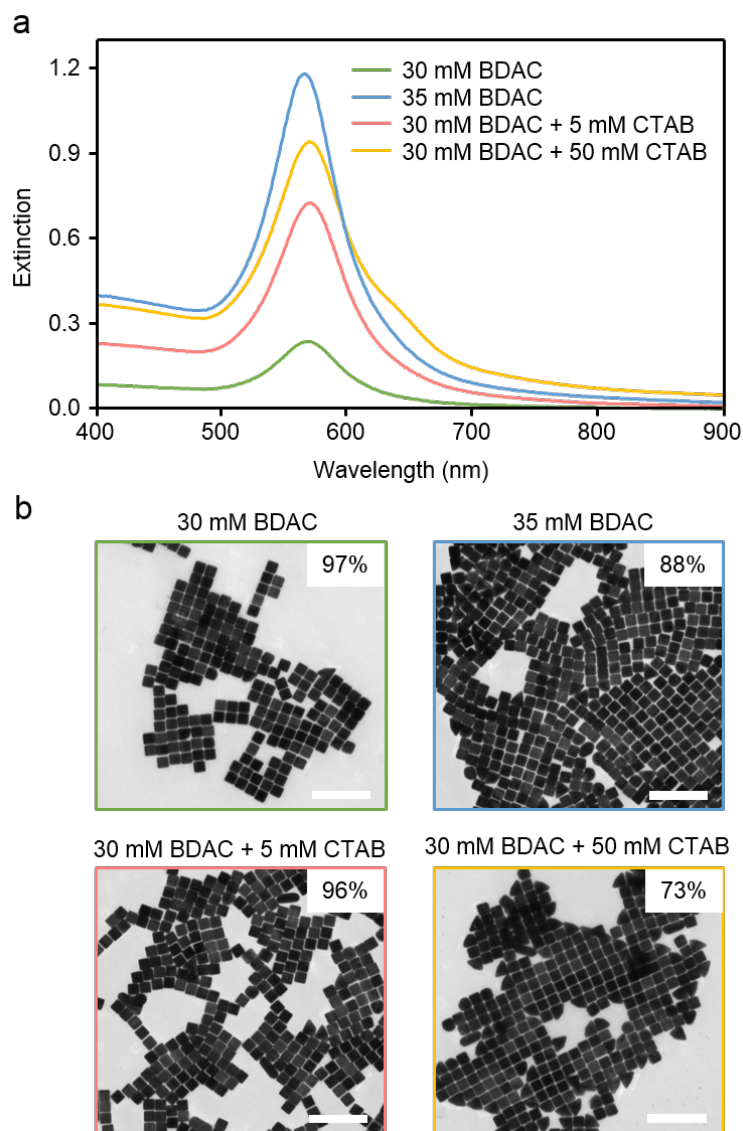
Figure 2.7. Comparison of various flocculation conditions. (a) Extinction spectra and (b) TEM images of AuNCs obtained under different flocculation conditions. The scale bars in (b) indicate 300 nm.
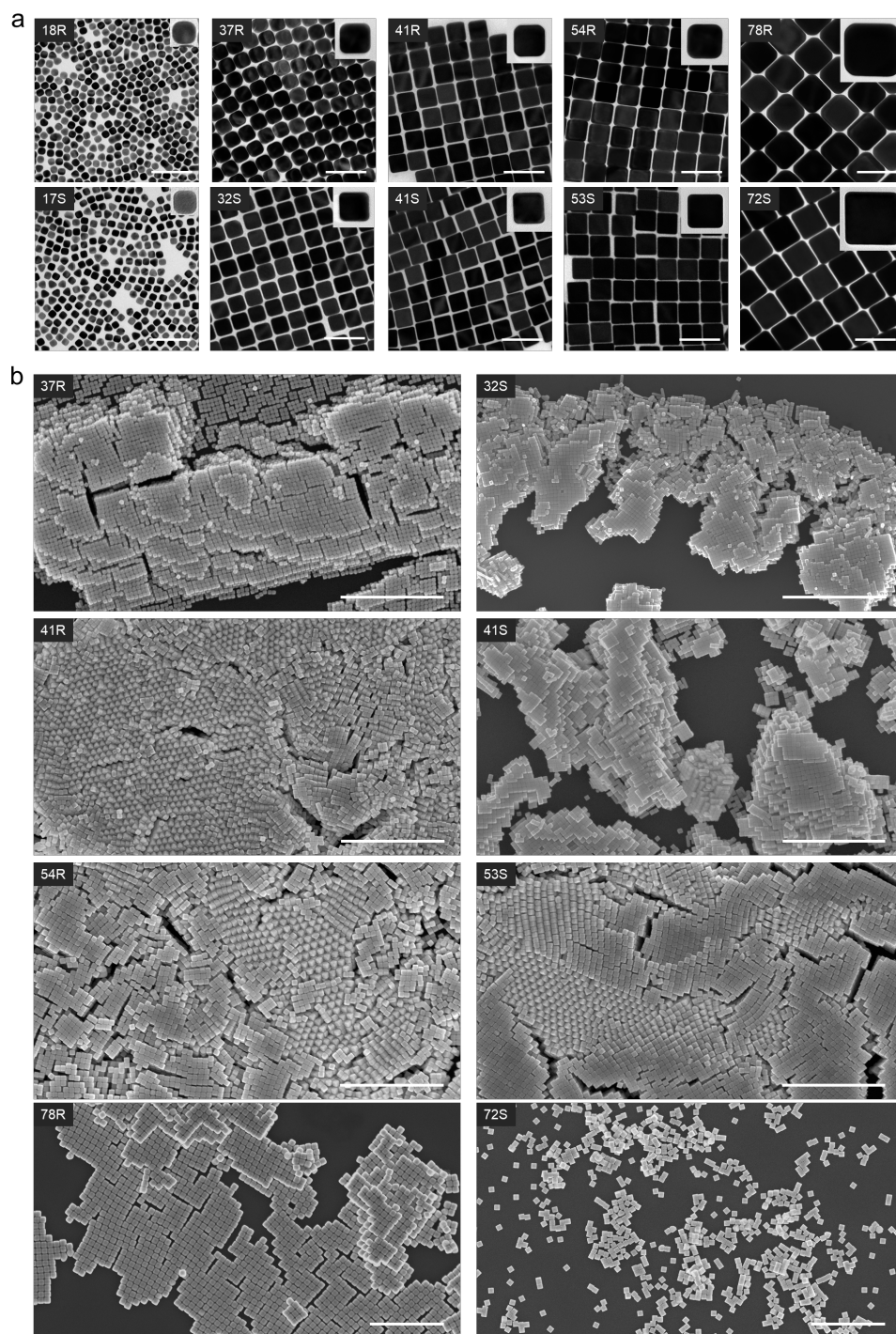
───

Figure 2.8. Shape-controlled AuNCs in a high yield. (a) TEM images of refined AuNCs with different amounts of seed and bromide; the insets show representative single-particle images to clearly visualize the sharpness difference. Numbers in the labels correspond to edge length, and R and S indicate round-cornered and sharp-cornered AuNCs, respectively. From left to right, each column was obtained with 300, 30, 9, 6, and 2 μL of seed solution at the same concentration, respectively. We also varied the bromide concentration at a fixed seed amount to control the corner sharpness, allowing R and S AuNCs. Compared to synthesis of sharp-cornered AuNCs, we applied a lower density of bromide to produce round-cornered AuNCs. (b) Low-magnification SEM images showing AuNCs in a high yield after refinement. The samples were prepared by drop casting AuNCs on silicon wafer. The image was taken at the boundaries where the particles were well-packed. The scale bars in (a) and (b) indicate 100 nm and 1 μm, respectively.
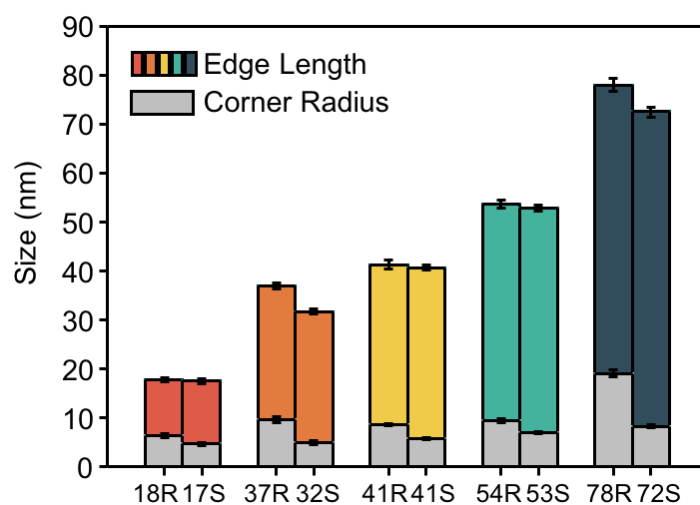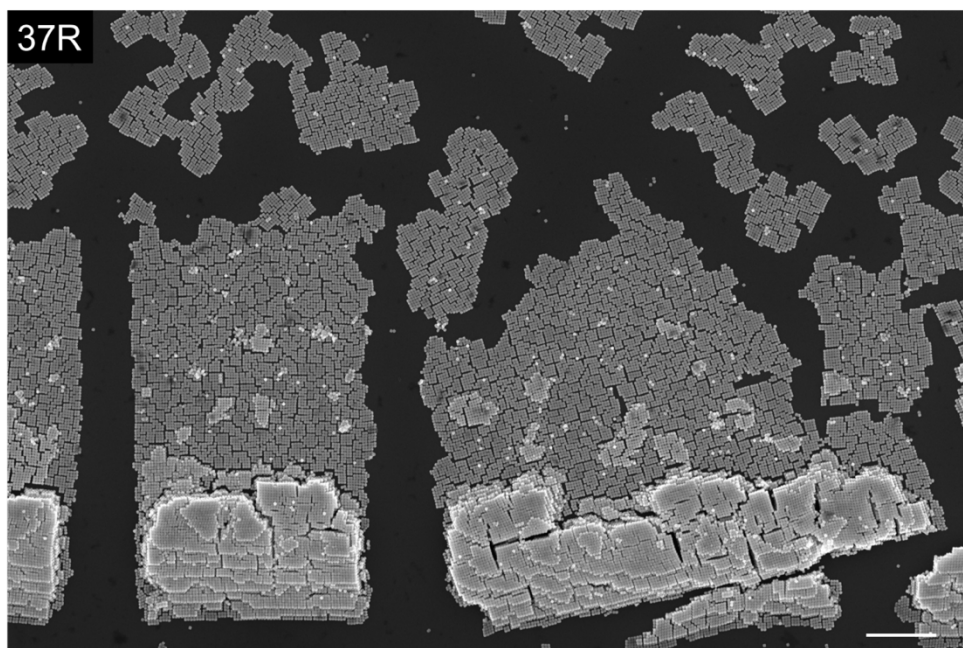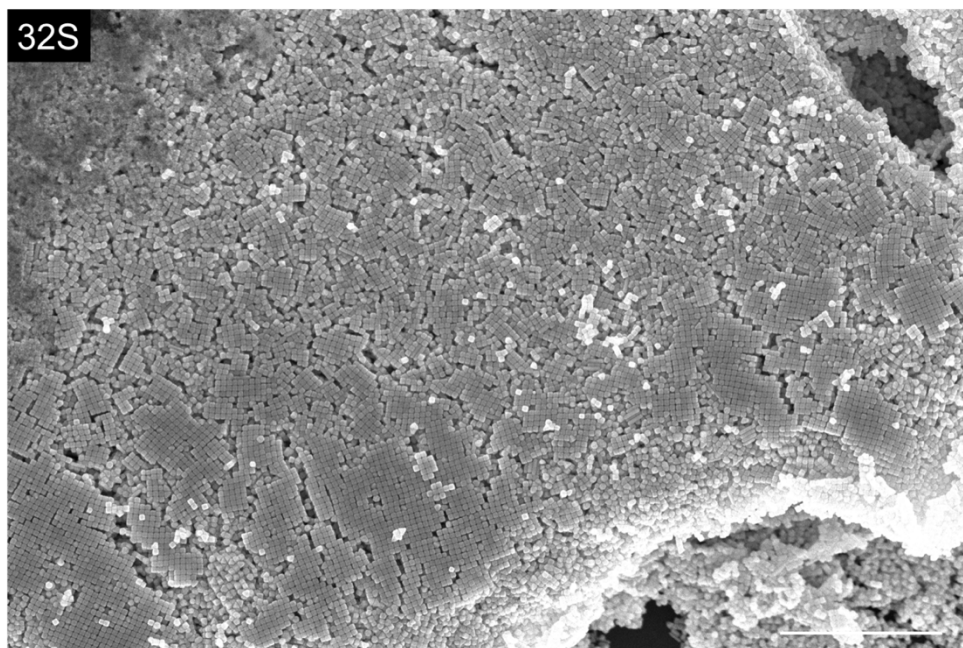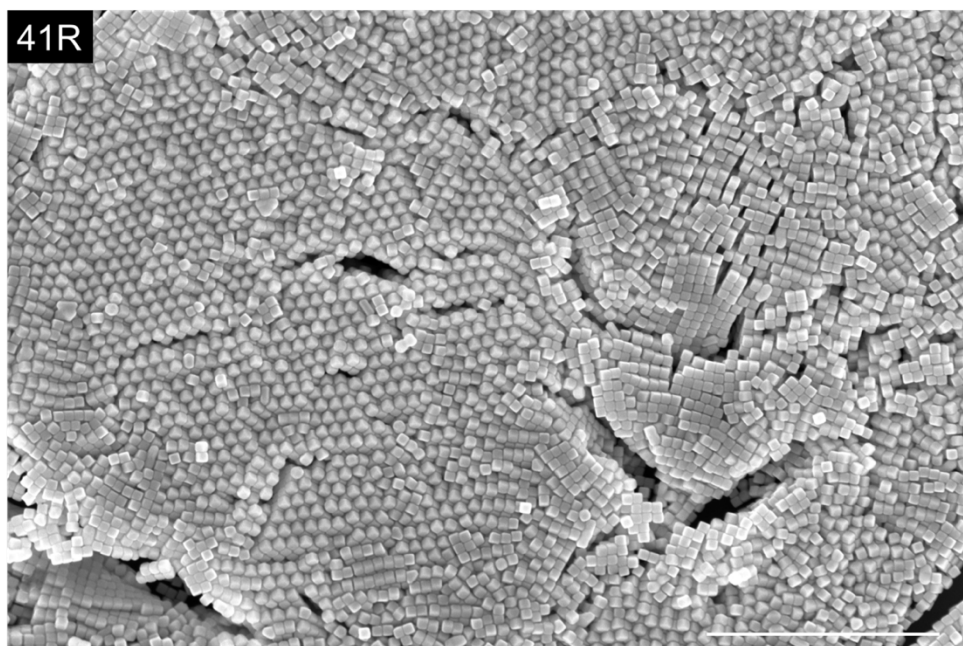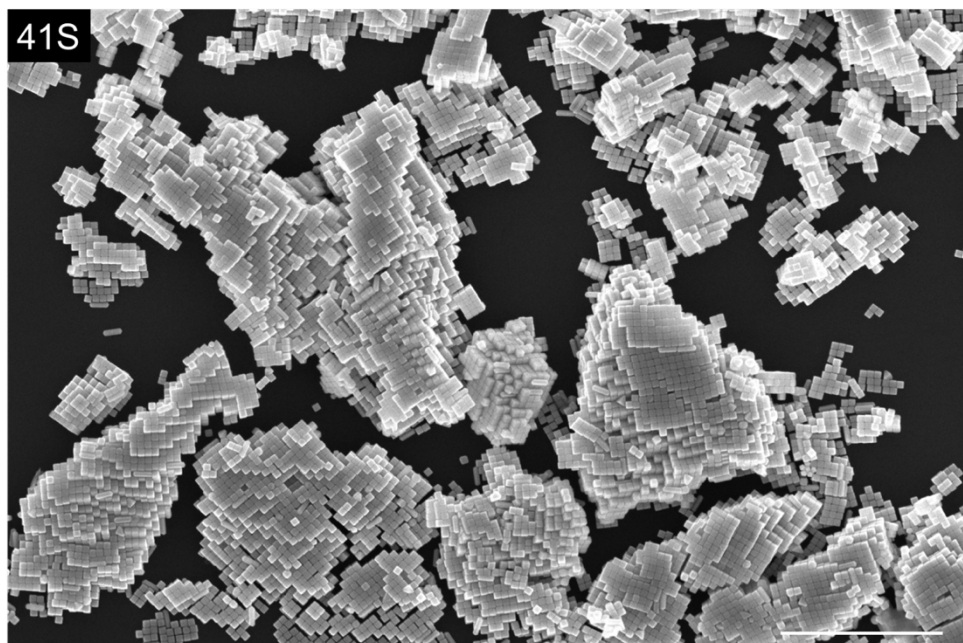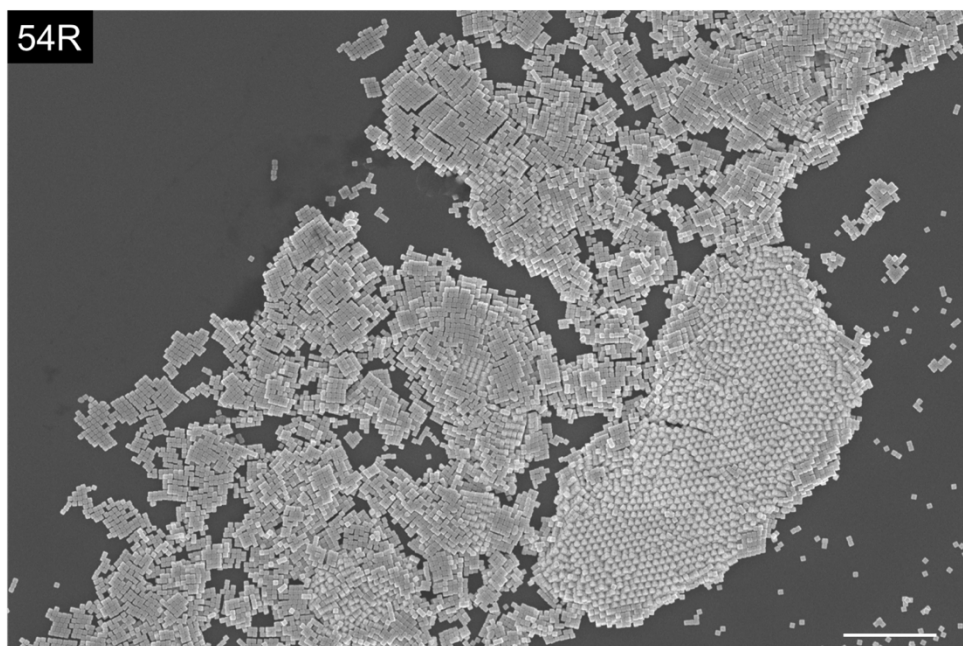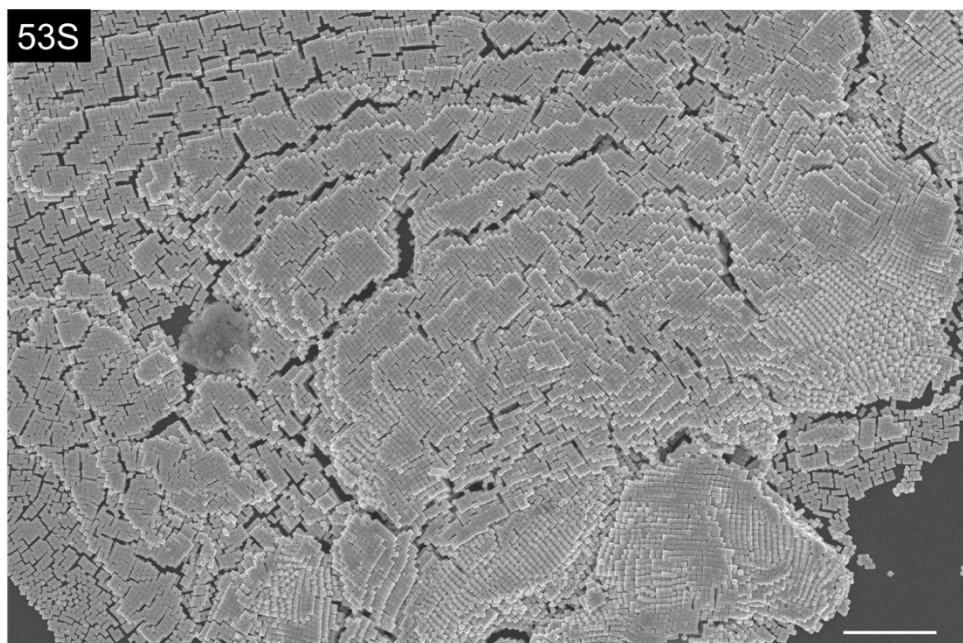
_____

Figure 2.9. Edge lengths and corner radii of AuNCs (n = 100). With decreasing seed volume from 300 μL to 2 μL, the edge length increased from 17 nm to 78 nm.
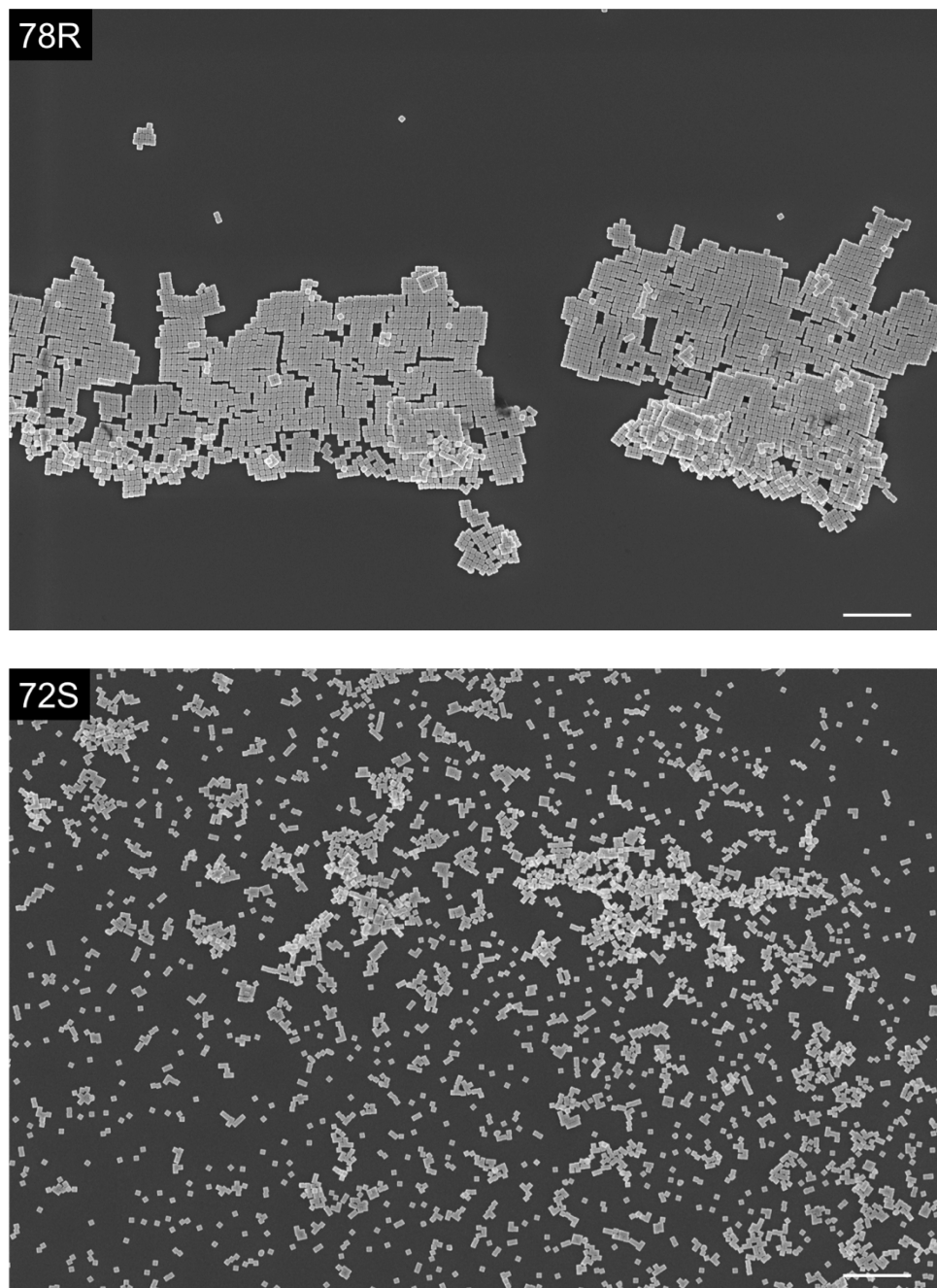
Chapter 2: Ultra-Precisely Synthesized Gold Nanocubes with Single-Particle-Level Reproducibility in Rayleigh and Surface-Enhanced Raman Scattering

──

_____

Chapter 2: Ultra-Precisely Synthesized Gold Nanocubes with Single-Particle-Level Reproducibility in Rayleigh and Surface-Enhanced Raman Scattering

_____

Figure 2.10. Low-magnification SEM images of 37R, 32S, 41R, 41S, 54R, 53S, 78R, and 72S AuNCs. The scale bars indicate 1 μm.

Chapter 2: Ultra-Precisely Synthesized Gold Nanocubes with Single-Particle-Level Reproducibility in Rayleigh and Surface-Enhanced Raman Scattering
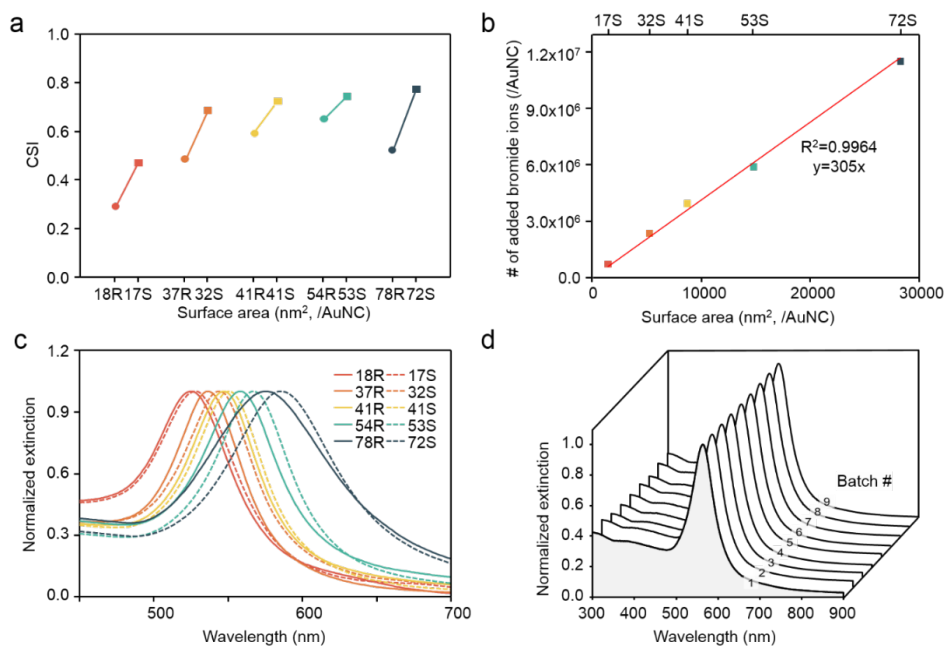
_____

Figure 2.11. Characterization of size and shape-controlled AuNCs. (a) CSI of AuNCs (n = 100). Size analysis on TEM images were implemented using ImageJ software. (b) Calculated number of the added bromide ions per AuNC for sharp-cornered AuNCs. (c) Normalized UV−vis spectra for a series of AuNC solutions. Solid and dashed lines correspond to round-cornered and sharp-cornered AuNCs, respectively. (d) Normalized extinction spectra of 9 different batches of 53S AuNCs after flocculation.
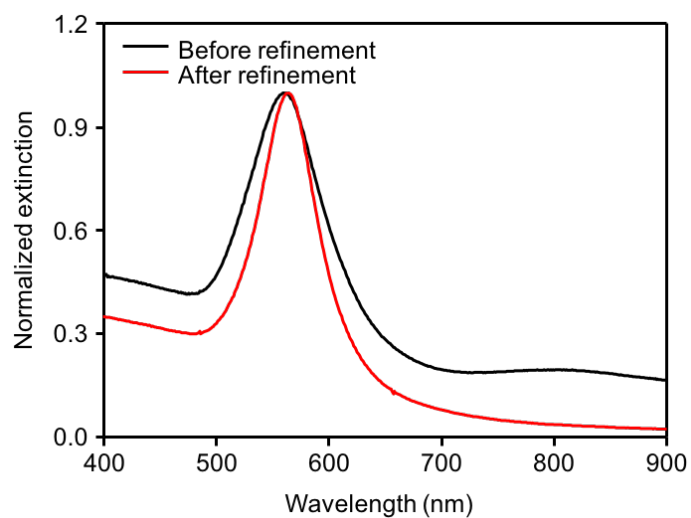
_____

Figure 2.12. Representative extinction spectra before and after refinement of 54R AuNCs.
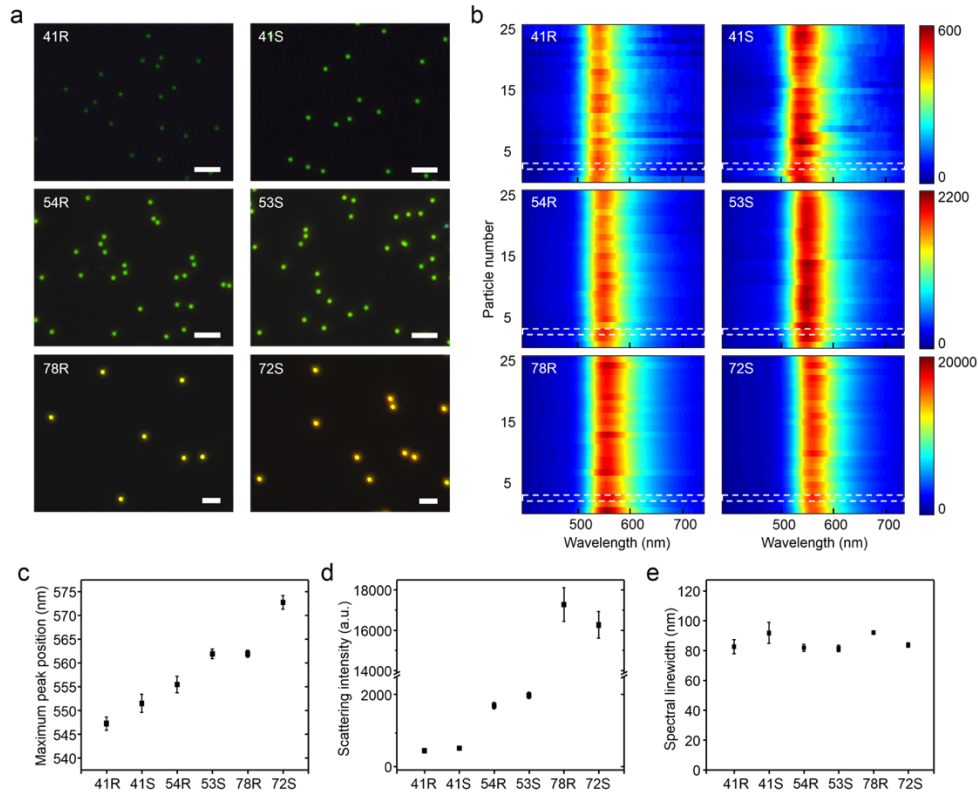
_____

Figure 2.13. Single-particle Rayleigh scattering analysis on AuNCs. (a) Dark-field microscope images and (b) Rayleigh scattering spectra of individual AuNCs. (c) Analyzed maximum peak position, (d) scattering intensity, and (e) spectral linewidth of each AuNC obtained from the analysis of (b). The samples were prepared by drop-casting AuNCs on a cleaned cover glass and spin coating particles with a microcentrifuge. The prepared glass samples were rinsed with DIW and ethanol to remove residual surfactants. The exposure times for acquisition of scattering images are 200 ms for 41R and 41S AuNCs, 120 ms for 54R and 53S AuNCs, and 80 ms for 78R and 72S AuNCs. The scale bars in (a) indicate 2 μm. The images in (a) were additionally adjusted to visualize the scattering signal while ensuring differences among each other. The scattering spectra in (b) were acquired from 25 different AuNCs. The relatively high noise level of scattering spectra for 41R and 41S AuNCs is from the decreased signal-to-noise ratio due to a relatively low scattering intensity. We acquired scattering spectra of 41R and 41S AuNCs with an exposure time of 20 s and those of 54R, 53S, 78R, and 72S AuNCs with an exposure time of 3 s in (b). The 20-s cases were normalized to the 3-s case under the assumption that the signals increase linearly with exposure time.
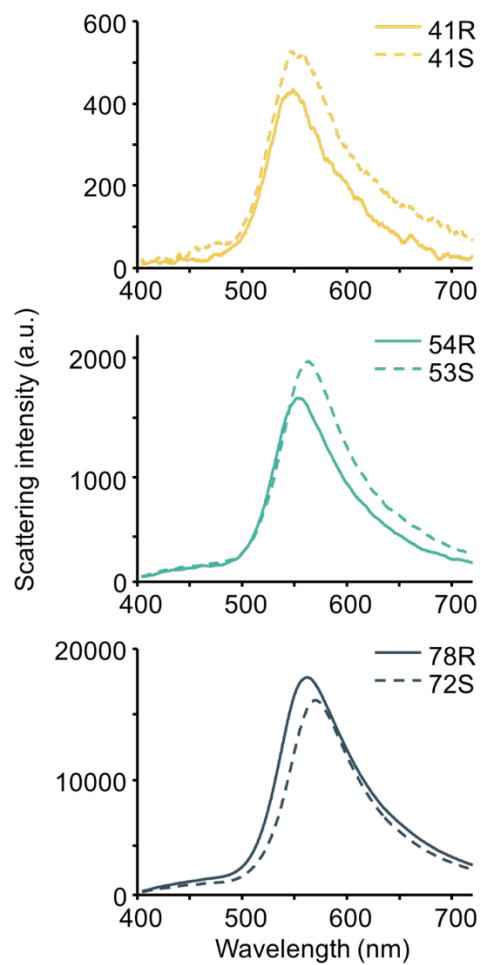
Figure 2.14. Representative Rayleigh scattering spectra of individual AuNCs marked with a white dotted box in Fig. 2.13b.

Chapter 2: Ultra-Precisely Synthesized Gold Nanocubes with Single-Particle-Level Reproducibility in Rayleigh and Surface-Enhanced Raman Scattering
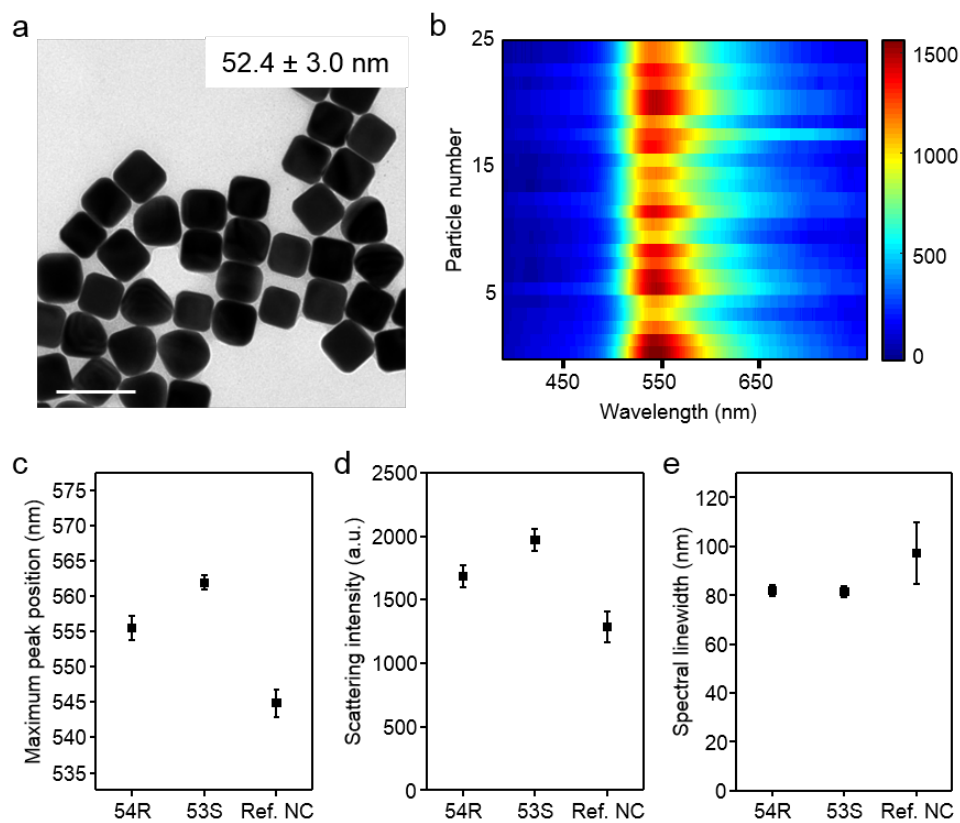
_____

Figure 2.15. Comparison with a previously reported AuNC synthesis. (a) TEM image and (b) Rayleigh scattering spectra of AuNCs prepared by a previously reported method.[93] Comparison of the maximum peak position (c), scattering intensity (d), and spectral linewidth (e) with 54R and 53S AuNCs. Scale bar in (a) indicates 200 nm.
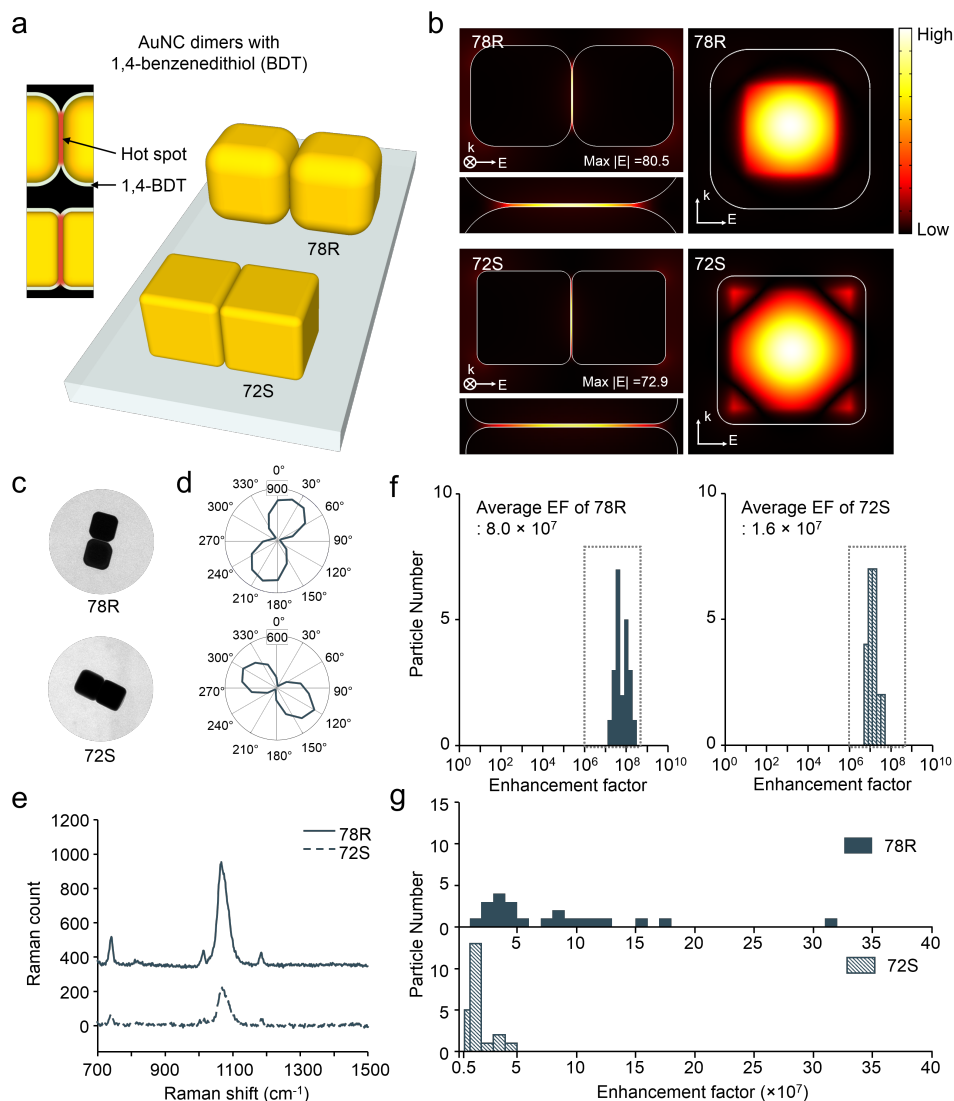
Figure 2.16. Single-particle polar plots, electromagnetic field distribution and single-particle surface-enhanced Raman scattering from AuNC dimers. (a) Schematic illustration of AuNC dimers (78R and 72S AuNC dimers) with 1,4-benzenedithiol. (b) Simulated near-field enhancement images of individual dimers, enlarged images of the gap [78R NC dimer (top) and 72S NC dimer (bottom)]. (c) Representative TEM images of 78R and 72S AuNC dimers and (d) the corresponding polar plots for the Raman peak at 1069 cm-1. The samples were prepared by drop-casting AuNCs on a silicon dioxide support grid. The dimer positions were located with a low-magnification TEM (×6000). After measuring the Raman signals, we additionally acquired the high-magnification images of dimers. (e) Representative Raman scattering spectrum from an individual AuNC dimer. (f

Chapter 2: Ultra-Precisely Synthesized Gold Nanocubes with Single-Particle-Level Reproducibility in Rayleigh and Surface-Enhanced Raman Scattering

───

and g) Single-particle SERS enhancement factor distributions [log scale (f) and linear scale (g) in the boxed regions in (f)] obtained from the measured Raman signal for 78R NC dimer (left) and 72S NC dimer (right), respectively (n = 22).
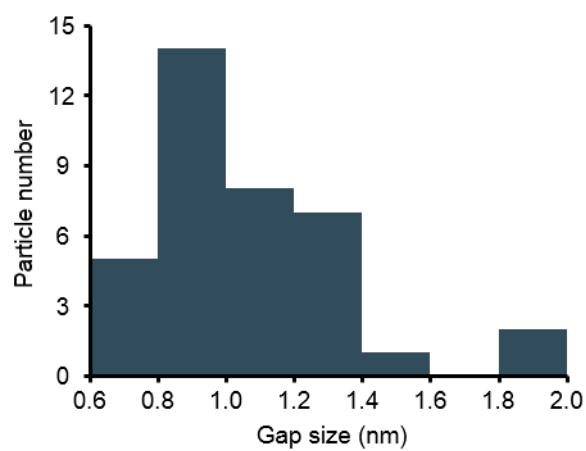
_____

Figure 2.17. Distribution of AuNC dimers gap size for 78R and 72S dimers.

_____

	Edge length (nm)	Corner radius (nm)
18R	17.82 ± 0.46	6.38 ± 0.43
17S	17.48 ± 0.59	4.64 ± 0.30
37R	36.98 ± 0.69	9.58 ± 0.57
32S	31.72 ± 0.52	4.99 ± 0.45
41R	41.30 ± 0.92	8.59 ± 0.27
41S	40.72 ± 0.55	5.81 ± 0.15
54R	53.65 ± 0.75	9.49 ± 0.36
53S	52.83 ± 0.65	6.98 ± 0.25
78R	77.98 ± 1.32	19.08 ± 0.74
72S	72.47 ± 1.02	8.27 ± 0.39

Table 2.1. AuNC dimensions obtained by TEM images analysis (n = 100).

───

Note

Note 1. Centrifugation-driven depletion-induced flocculation

The depletion potential energy U can be expressed as[90]

$$U = -V_e \cdot C_m N_0 k_B T,$$

where V_e is the excluded volume, $C_m = (c - c^*)/n$ is the micelle molar concentration, c is the molar concentration of the surfactant, c^* is critical micelle concentration, n is the number of surfactant molecules required to form a micelle, N_0 is Avogadro's number, k_B is Boltzmann's constant, and T is temperature. General colloidal flocculation without centrifugation is known to occur if the potential exceeds ~ 4-5$k_B T$. If potential becomes too high, selectivity in shape of particles decreases and the final yield reduces. For optimizing the flocculation condition, we used 53S AuNCs with varied surfactant conditions. Based on the above equation and known parameters ($c^*_{BDAC} = 0.0005$, $n^{BDAC} = 62$, $c^*_{CTAB} = 0.001$, $n^{CTAB} = 162$),[91] we obtained the depletion potential energy for 53S AuNCs in each calculation condition as follows.

Flocculation condition	Potential energy ($k_B T$)	Yield (%)
30 mM BDAC	2.60	97
35 mM BDAC	3.04	88
30 mM BDAC + 5 mM CTAB	2.73	96
30 mM BDAC + 50 mM CTAB	4.25	73

In our study, effective flocculation can occur with a relatively low depletion potential in a very short time. At the bottom of the centrifugal tube, centrifugal force pushes particles close to each other, giving extra driving force to flocculation. Taking into account the calculated potential energy, we can interpret the experimental results in Fig. 2.7. When AuNCs are in 30 mM BDAC solution, even though the potential is lower than the typical flocculation potential, AuNCs of 97% yield can be flocculated at a potential energy of 2.60 $k_B T$ with the aid of the external force of centrifugation. If we slightly increase the BDAC concentration to 5 mM, the excess potential results in the co-flocculation of byproducts, decreasing the yield to 88%. Adding the same concentration of CTAB instead of BDAC induces a marginal increase in potential energy, ensuring ~3 times larger amount of AuNCs to be flocculated while maintaining monodispersity (yield of 96%). If we add a larger amount of CTAB, the potential is significantly increased, decreasing the final AuNC yield to 73%. Even though we may expect to obtain high-quality AuNCs from a BDAC concentration of 31 mM with 2.69 $k_B T$, which corresponds to a potential between 2.60 $k_B T$ (yielding 97%) and 2.73 $k_B T$ (yielding 96%), it is conclusive that precise potential modulation is more easily accessible with the adoption of CTAB, which enables subtle control of potential. Besides this potential effect, since the surfactants of

68

───

AuNC are CTA$^+$, there may be other diverse roles of CTAB; further investigations are required to clarify the other roles. For refinement of the nanoparticle solution of which a volume that is not applicable to centrifugation, one can refine them by incubating the nanoparticles overnight, as in the previous method, but with a higher concentration of BDAC compared to that used for centrifugation-driven flocculation.

Chapter 3

Highly Controlled Synthesis and Super-Radiant Photoluminescence of Plasmonic Cube-in-Cube Nanoparticles

3.1. Introduction

While the direct PL of metals was first reported by Mooradian in 1969, it was not studied extensively for many years, owing to the low QY of metals.[26] After Boyd reported the local field enhancement of the PL from smooth and rough metal surfaces, it was demonstrated that metal NPs, more specifically, Au nanorods (AuNRs), exhibit significantly enhanced PL.[32,98] Over the past decades, PL signals from various nanostructures, including Au nanospheres and AuNRs, have been investigated.[34,38-42,99,100] It was reported that Au nanobipyramids exhibit a QY of ~10⁻⁵, which is one order-of-magnitude higher than that of AuNRs.[41] However, most of these studies focused on the correlation between PL and the localized surface plasmon resonance (LSPR) for different polarization angles or excitation wavelengths. It was shown that the PL spectrum can be tuned by varying the nanostructure geometry, as is the case for LSPs. In recent years, PL from plasmonically coupled nanostructures has been investigated extensively.[43,46,48,101] It was reported that the QY of Au dimers, composed of two spherical AuNPs, is similar to that of the constituent monomers, even though the local field between the dimer junctions is higher.[46] On the other hand, other research group have reported enhanced PL in the case of nanostructures located on thin Au films; this was attributed to gap plasmons.[43] Therefore, the effect of the plasmonic coupling on PL intensity remains to be clearly elucidated. Up to date, several mechanisms have been proposed to explain the observed phenomenon of PL in nanostructures: (1) e-h recombination after an interband transition, (2) radiative emission of LSPs excited by an interband transition, (3) intraband transition followed by e-h recombination, (4) inelastic

scattering of the *sp*-band electrons, and (5) direct excitation of the LSPR followed by radiative emission. However, the exact mechanism remains a matter of debate.[33,35,38,40,43,46,99-101] Until now, plasmonically coupled systems have mostly been limited to lithographically fabricated structures or simple nanostructures positioned on a metal film. PL from plasmonically coupled NPs while ensuring precise control over the nanometer scale has not yet been achieved. Importantly, NPs that exhibit both a strong PL signal and a high QY have not yet been designed nor synthesized.

Here, we designed and synthesized interior-nanogap-engineerable cube-in-cube (CiC) NPs that exhibit intense PL (Fig. 3.1a), and the mechanism in generating strong PL from these particles was studied. These interior gap-based plasmonic couplings are tunable and robust, and induce minimal signal fluctuations when compared between particles.[97] The AuNCs were chosen as the core material since they exhibit a higher QY than the QYs of nanospheres and AuNRs.[42] Further, well-defined faces, edges, and vertices result in a well-defined nanogap with a uniform electromagnetic field between the core and the shell. In order to form the outer shell from the core in the presence of interior gap, we developed a GVF process, composed of galvanic replacement/reduction and void formation steps (Fig. 3.1a). We were able to synthesize targeted nanostructures with high structural precision and high yield (~88%). The super-radiant PL mechanism is proposed for the plasmonic coupling-based PL enhancement from metal nanostructures for the first time in this study, and, based on this mechanism and the plasmon hybridization theory, the optical properties of the CiC NPs were analyzed. Significantly, the CiC NPs show highly enhanced PL intensity and higher QY than AuNCs, and the PL intensity and

QY from the CiC NPs are the highest values ever reported from metallic NPs.

3.2. Experimental Section

Materials

Cetyltrimethylammonium bromide (CTAB) and cetyltrimethylammonium chloride (CTAC) were purchased from TCI. Ascorbic acid, gold chloride trihydrate, and silver nitrate were purchased from Sigma-Aldrich. Sodium borohydride was purchased from DaeJung Chemicals & Metals. All the reagents were used as received. Deionized water (DIW) obtained using a Millipore system (> 18.0 MΩ, Milli-Q) was used in all the experiments.

Synthesis of AuNCs

The AuNCs were synthesized by the previously reported seed-growth method.[93] All the solutions used were prepared using DIW. To synthesize the Au seed solution, 7.5 mL of a 100 mM CTAB solution was prepared in a round-bottom flask inside a water bath heated to 30°C. Next, 250 µL of a 10 mM HAuCl$_4$ solution was added to the flask and the mixture was stirred using a stirring bar at 500 rpm. Then, 600 µL of an ice-cold 10 mM NaBH$_4$ solution was quickly added to the solution, turning the solution brown. The solution was then stirred for 2 min and was used as the seed solution in the next step after incubation at 30°C for a minimum of 1 h. Then growth was proceeded in 50 mL conical tubes. First, 1.6 mL of the 100 mM CTAB solution was mixed with 8 mL DIW. Next, 200 µL of the 10 mM HAuCl$_4$ solution and 950 µL of a 100 mM ascorbic acid solution were added to the mixture

73

sequentially. The solution became transparent after the addition of the ascorbic acid solution. Then, 5 μL of a 10-times-diluted seed solution was dripped down the tube wall and mixed gently with the prepared mixture using soft inversion mixing. The AuNCs were collected by performing centrifugation (5500 rpm, 10 min) twice after overnight incubation. After the supernatant had been removed, the particles were dispersed again in DIW for further use.

Ag shell coating on AuNCs

All the solutions used were prepared in DIW. We optimized a previously reported protocol to form the Ag shells.[102] First, 400 μL of a 10 pM AuNC dispersion was mixed with 400 μL of a 10 mM CTAC solution and 200 μL of a 50 mM ascorbic acid solution. After the two had been mixed, 40 μL of $AgNO_3$ solutions of different concentrations (0.5–5.0 mM) were added to the mixture and mixed using a vortex mixer. After incubation for 3 h at 60°C, the coated nanoparticles were collected by performing centrifugation twice (5000–6000 rpm, 10 min) and redispersed in DIW for further use.

Preparation of CiCs

All the solutions used were prepared in DIW. First, 400 μL of a 10 pM suspension of the Ag-shell-coated NCs was mixed with 400 μL of 100 mM CTAB and 87 μL of 100 mM ascorbic acid. The mixture was incubated for 3 min at 70°C while being stirred at 300 rpm. Then, 400 μL of a $HAuCl_4$ solution (0.06–0.15 mM) was injected into the mixture using a syringe pump at a speed of 20 μL/min. After

74

the completion of the injection process, the solution was incubated for 5 min more and centrifuged twice at 4500 rpm for 5 min. Finally, the solution was mixed with 400 μL of DIW. Next, it was mixed with 400 μL of 10 mM CTAB. Then, 400 μL of a HAuCl$_4$ solution (0.008–0.13 mM) was injected into the mixture all at once. The mixture was then incubated for 20 min at 30˚C. After the injection process, the solution was centrifuged twice (4500 rpm, 5 min) and the CiCs were dispersed in DIW.

Characterization of nanostructures

The TEM and SEM images are obtained using JEM-2100 (JEOL) and Helios NanoLab 650 (FEI) systems, respectively, at the National Center for Inter-University Research Facilities (NCIRF), Korea. The HAADF-STEM data (and the corresponding EDS maps) and the SAED patterns were obtained using a JEM-2100F (JEOL) system at the Research Institute of Advanced Materials (RIAM), Korea.

Electromagnetic calculations

We used FEM simulations, performed using the commercial software COMSOL Multiphysics, for the theoretical analysis. The model used was based on an analysis of the CiC structure as determined from the TEM and SEM images. The electric fields and extinction cross-sections were computed in the scattered-field mode under plane-wave excitation. The core was modelled as being of Au, while the shell was modelled as being of a Au-Ag alloy. The surrounding medium and the gap region between the core and the shell were modelled as water. The empirical

dielectric function reported by Hale and Querry[103] was used for water. For Au and the Au-Ag alloy, an analytical model[104] was used.

Optical measurements

The ultraviolet-visible (UV−Vis) spectra of the nanostructures were measured using an UV−vis spectrophotometer (Agilent 8453 spectrophotometer, USA). The PL measurements were performed with a HORIBA LabRAM ARAMIS Raman microscope. The excitation laser used was an ND:Yag laser (532 nm) equipped with 600 gr/mm gratings and a multichannel 1024 × 256 air-cooled charge-coupled device detector (pixel size: 26 × 26 μm). All the spectra were acquired using a 5× objective lens for a laser power of 5 mW and an exposure time of 10 s. Generally, 12 μL of a suspension of the nanostructure being tested was placed in a silicone isolator on a glass substrate for the measurements. Notch filters were used to prevent the direct scattering of the laser, which resulted in a significant decrease in the number of photocounts near the wavelength of the excitation laser in the spectra. The measured PL spectra were subtracted from those of a bare glass coverslip and DIW, which were used as the references. All the PL spectra were also corrected by subtracting the background signals for the glass and DIW and then smoothened further using the software Origin 8.0, in order to eliminate the noise. For the TIRF measurements, 1 μL of the CiC solution was spin-coated on a glass slide, which was then washed with ethanol and dried.

Calculation of I and QY

The absorption cross-sections at the excitation wavelength (an increase of 2 times from the 47-nm AuNCs to the CiCs) and the squares of the second time-derivative of the total dipole moment at the LSPR wavelength (an increase of 12.3 times from the 47-nm AuNCs to the CiCs) were calculated through FEM simulations.

$$\Phi_s = \frac{\varepsilon_r}{c_r} \times \frac{c_s}{\varepsilon_s} \times \Phi_r$$

The QYs of the nanostructures were obtained based on the equation above, where Φ, σ and c are the QY value, molar absorption coefficient at excitation wavelength and solution concentration, respectively. Suffixes s and r mean the term for the sample and Rhodamine 6G (R6G). We used 1.160×10^5 cm^{-1}M^{-1} and 0.95 for σ and c of R6G. The molecular absorption coefficient of AuNRs was taken from a previous study.[40]

3.3. Results and Discussion

In a typical experiment, first, ~47-nm AuNCs were synthesized and coated with a ~13-nm Ag shell with literature procedures [transmission electron microscopy (TEM) images; Fig. 3.1b-i, ii; see Supporting Information for synthetic details]. By precisely controlling the concentrations of the cetyltrimethylammonium chloride (CTAC) surfactant and the Ag precursor, the thickness and vertex sharpness of the Ag shell were controlled over a large number of particles (Fig. 3.1b-ii and Fig. 3.2). Next, the galvanic replacement/reduction step was performed with ascorbic acid at

70˚C. We used time-dependent TEM images to confirm the synthetic mechanism, namely, the oxidation of Ag atoms by Au precursor and the simultaneous co-reduction of Au and Ag ions by ascorbic acid (Fig. 3.1b-iii and Fig. 3.3). In particular, the synergistic effect of high temperature and the presence of the reducing agent resulted in the nearly seamless, solid, and robust cubic Au-Ag alloy shells (Fig. 3.4). In contrast, when the galvanic replacement reaction was performed at 25˚C and/or without the reducing agent, it resulted in rough or porous surfaces, which inhibit uniform, controllable plasmonic coupling.[105] The subsequent void formation step, performed in the absence of the reducing agent at reduced temperature, pushes away the residual inner Ag atoms and forms a clear void between the core and the shell (Fig. 3.1b-iv). Using scanning electron microscopy (SEM), we could confirm the vertex truncation as ~25% of edge length; the truncation was induced to minimize the total surface energy and produce (111) planes instead of less stable (100) ones (inset of Fig. 3.1c and Fig. 3.5).[105] It was also observed that connecting junctions were formed between the core and the shell (inset of Fig. 3.1b-iv and bottom right image of Fig. 3.1d). The obtained CiC NPs were homogeneous and had an edge length of 85.11 $\pm$ 1.07 nm (n = 50), a gap size of ~9 nm, and a shell thickness of ~10 nm. By analyzing 200 nanostructures, we could confirm that the synthetic yield was ~88% (Fig. 3.1c). Importantly, we synthesized the CiC NPs with different gap sizes by varying Ag shell thickness (Fig. 3.6). The gap distance was changed to ~1, 3 or 15 nm while keeping the outer-shell thickness constant at ~10 nm. In order to determine the elemental compositions of the nanostructures as well as the spatial distribution of each constituent element, we performed high-angle annular dark-field

scanning transmission electron microscopy (HAADF-STEM) and energy-dispersive X-ray spectroscopy (EDS) mapping. The obtained HAADF-STEM images yielded the information regarding the formation of the Au−Ag alloy shell with the presence of an interior nanogap (Fig. 3.1d). Most of Ag atoms were present mainly in the inner part of the shell, whereas Au atoms were distributed rather evenly in the core and the shell. These results support the proposed synthesis mechanism described above. The electron diffraction pattern of the CiC NPs was symmetric and indicative of a single-crystalline structure. More specifically, the pattern suggested that the preferential growth direction of the surfaces was along the fcc (100) facet, indicating epitaxial growth from the NCs to the CiCs, which can be attributed to low degree of lattice mismatch between Au and Ag (Fig. 3.1e).

We used the plasmon hybridization model to explain the coupling between the core and shell of the CiCs.[106] When the two dipolar parent modes of a cube and a truncated cubic shell are hybridized, they form two dominant plasmon modes, bonding dipolar and antibonding dipolar modes (Fig. 3.7a). The asymmetric hybridization originates from the phase-retardation effect.[106] Importantly, antibonding modes exhibit a super-radiant character with an increased total dipole moment while the bonding mode is sub-radiant with a reduced total dipole moment. The concept of super-radiance was first described in the field of fluorescence.[107] When the emitters interact and coherently interfere with each other, they exhibit cooperative emission, in contrast to the case for isolated scatterers. When the collective oscillation of the free electrons of a metal can be regarded as being analogous to an oscillating dipole, the radiative damping rate of such plasmon modes

is proportional to the square of the second time-derivative of the dipole moment.[108] As a plasmon mode becomes super-radiant, the degree of radiative damping increases dramatically.

The results of plasmonic coupling can be further explained by the extinction spectrum. The spectra obtained using the finite element method (FEM) simulations showed the energy level of each mode (Fig. 3.7b). The AuNCs exhibited an extinction peak in the visible region while the nanoshells showed a strong extinction peak in the near-infrared (NIR) region as well as a small shoulder related to the quadrupolar mode arising from their large size (Fig. 3.7b and Fig. 3.8). The calculated extinction spectrum of the coupled CiCs exhibited two main plasmon modes, as expected. The antibonding mode increased the line-width, which reflected the super-radiant character, whereas the sub-radiant character of the bonding mode was reflected in the sharpness of the line-width. It should be noted that the peak in the visible region was primarily attributable to scattering whereas the peak in the NIR region was indicative of strong absorption. Further, the smaller the gap distance, the stronger the coupling was between the core and the shell, resulting in a lowering of the energy of the bonding plasmon mode (Fig. 3.6). The experimentally determined extinction spectrum of the CiC NPs matched well with the calculated one, even though the residual Ag within the gap had not been taken into account in the FEM model, suggesting that the residual Ag atoms had a negligible effect on the far-field optical properties (Fig. 3.7c). The broadening seen in the empirical spectrum was attributed to the intrinsic heterogeneity of the nanostructures. The CiCs exhibited two distinctive peaks at ~1.45 eV (855 nm) and ~2.15 eV (577 nm).

The spectrum of the CiCs with 15-nm gap did not show any clear peaks owing to the large amount of residual Ag left over from the thick Ag shell after the galvanic replacement reaction (Fig. 3.6). This residual filled up the void between the core and the shell, thus inhibiting plasmonic coupling.

To clearly elucidate the effect of the interior nanogap on PL, we synthesized AuNCs of two different sizes. The size of the smaller AuNCs (size of 47 nm) was same as that of the core of the CiCs, while the larger AuNCs (size of 87 nm) had a size similar to that of the CiCs (Fig. 3.9a). The extinction spectra of the 47- and 87-nm AuNCs contained a single LSPR peak (Fig. 3.10a). The maximum LSPR wavelength of the 87-nm AuNCs was red-shifted compared to that of the smaller AuNCs, with the extinction intensity of the 87-nm AuNCs being the highest among those of the three nanostructures, owing to the large size of the AuNCs. Further, the calculated extinction spectrum of the 87-nm AuNCs was similar to the observed one (Fig. 3.9b). Based on the cross-sectional images of the electric field inside the metal, we concluded that the field intensity within the core of the CiCs is stronger than that within the shell in the visible region (Fig. 3.11). In the case of the peak in the NIR region, the strong electric field of the CiCs was distributed mainly in the shell area. Thus, we concluded that the peak in the visible region is core-dominated while that in the NIR region is shell-dominated.

The selection of the proper excitation laser source when studying the PL of nanostructures is important, since the PL intensity is maximized when the excitation wavelength overlaps with the LSPR wavelength of the nanostructure of interest.[34,43,100] In this study, we performed the PL measurements using a 532-nm

laser as the excitation source, and the PL intensity was measured in the ensemble

mode for wavelengths of 535–1000 nm. We verified that the inner-filter effect,

wherein re-absorption by the neighboring particles needs to be taken into account,

was negligible during the ensemble measurements (Fig. 3.12). The linear

relationship between the laser power and the PL intensity suggests that PL is one-

photon process (Fig. 3.13). The PL intensity of the CiCs with 9-nm gap differed

greatly from those of the two AuNCs as well as those of the CiCs with different gap

sizes (Fig. 3.10b). Significantly, the larger AuNCs exhibited PL with a markedly

lower intensity than that of the CiCs, suggesting that the inner nanogap of the CiCs

helped significantly enhance the PL signal. Since the nanostructures synthesized in

this study were obtained in a high yield, the differences in the PL intensities of the

various NPs can be primarily attributed to the differences in their structures. We

attribute the enhancement to the super-radiant character of the plasmon mode and to

the improved absorption ability. This is a first suggestion of the super-radiant PL

from plasmonic nanostructures, and the PL intensity, I_{PL}, can be written as shown in

equation (1).

$$I_{PL} \propto \sigma_{abs} \cdot \ddot{P}^2 \qquad (1)$$

When considering the absorption and emission steps related to the PL

process, the I_{PL} is proportional to the product of σ_{abs} and $\ddot{P}^2$, where σ_{abs} is the

absorption cross-section at the excitation wavelength and the $\ddot{P}^2$ is the radiative

damping rate, which can be described as the square of the second time-derivative of

the total dipole moment, P.[108] The radiative damping rate can be regarded as a QY in empirical value since both indicate the emission efficiency. Compared to the 47-nm AuNCs, we obtained the 1.9 and 12.3 times higher absorption cross-section and radiative damping rate for CiCs. Based on this, we determined the ratio of the total PL intensity of the CiCs to that of the 47-nm AuNCs to be 24.7, which is comparable to the experimentally obtained value of 31.3 (Fig. 3.14a). The enhancement factor can be calculated with greater precision if one takes other factors into account based on the PL mechanism, such as the relaxation parameter.[101] One possible explanation for the low PL intensity of the 87-nm AuNCs can be the relatively large energy mismatch between the excitation wavelength and their maximum LSPR wavelength[34] and the fact that the AuNCs exhibited ordinary and not super-radiative dipole oscillations.

Interestingly, the PL spectrum of the CiC NPs contained a single peak, even though their scattering spectrum had two LSPR peaks. This observation is not in keeping with previous studies, which have suggested that the PL spectra of nanostructures resemble their respective scattering spectra.[34,38-40,100,101] Further, many researchers consider local field enhancement to be the reason for the enhanced PL intensity of nanostructures. However, we did not observe a PL peak in the NIR region, even though the calculated electric field corresponding to the LSPR peak in the NIR region was stronger than that for the peak in the visible region, indicating that a stronger electric field does not always guarantee a higher PL intensity. Taking excitation energy relaxation and the sub-radiant character of the NIR peak into account can help interpret this phenomenon. The energy from the excitation laser

can be re-distributed and relaxed exponentially by electron-electron and electron-phonon coupling.[109,110] This decreases the probability of the excitation of the LSPR mode far from the excitation wavelength. In addition, the sub-radiant LSPR mode has a smaller chance to radiate.

Finally, we compared the QY and integrated total PL intensity, that is, the PL brightness, of the CiCs with those of other nanostructures as well as an organic dye (Fig. 3.14a, Fig. 3.15 and Table 3.1). Taking into account the calculated molar absorption coefficient at 532 nm and the total PL intensities, we determined the QY of each sample while using R6G as the reference. The QY of the CiC NPs was 4.38×10^{-4}, which was 16.2 and 12.3 times higher than those of the 47-nm and 87-nm AuNCs, respectively. The QY of the 47-nm AuNCs was determined to be 2.80×10^{-5}. The super-radiant character of plasmon mode, which arouse from the plasmon coupling, enables it to possess increased radiative damping, allowing an increase in the QY. To confirm the measured values, we used AuNRs as an internal reference; their measured QY of 7.53×10^{-6} agreed well with the recently reported data from a reference (Fig. 3.14a and Fig. 3.16).[38-41] The inclusion of increased QY and higher absorption cross-section provides 31.3 times higher PL intensity for CiC NPs than 47-nm AuNCs. Besides, CiCs have 13.5 times stronger PL than 87-nm AuNCs although they share similar absorption cross-section values, implying the significant role of super-radiant plasmon mode in enhancement of PL from plasmonic nanostructures. The total PL intensity of the CiCs was three orders of magnitude higher than that of the conventional organic fluorophore R6G for the same concentration. Importantly, the PL signal of the CiC NPs as measured using total

internal reflection fluorescence (TIRF) microscopy under continuous laser illumination at least for 1 h remained stable with neither photobleaching nor photoblinking occurring (Fig. 3.14b and Fig. 3.17). This confirmed that the PL observed indeed originated from the nanostructures and not the surrounding molecules, since the fluorescence from organic molecules bleaches after a while.

3.4. Conclusion

In this study, we designed and synthesized interior-nanogap-engineerable CiCs, which exhibited highly enhanced PL via the super-radiant plasmonic coupling in CiCs. The controlled two-step GVF reaction, composed of replacement/reduction and void formation steps, produced the CiCs with a uniform, controllable interior nanogap in a high yield. Importantly, we found the plasmonic coupling between the core and the shell resulted in a super-radiant LSPR mode, which significantly increase the radiative damping of the corresponding LSPs, providing highly enhanced PL from CiCs. The CiC NPs showed ~2 and ~16 times higher absorption cross-section and QY, respectively, resulting in ~31 times higher PL intensity than 47-nm AuNCs, and these are the highest PL intensity and QY reported for metallic nanostructures. Moreover, the total PL intensity of CiC NPs was 3 orders of magnitude higher compared to the organic fluorophore (R6G in this case). With the results, a designing strategy and a plasmon hybridization-based mechanism can be proposed for improving the PL from nanostructures. Further, various types of core−gap−shell nanostructures such as sphere-in-sphere or rod-in-rod can be also

synthesized by the controlled two-step GVF reaction, and their optical properties can be studied, tuned, and improved in a similar manner. Moreover, the wavelength of the PL from these plasmonic nanostructures can be controlled readily by tuning the LSPR of the nanostructures based on their structure and composition. The PL exhibited by metals is optically stable, which distinguishes it from the PL from organic fluorophores and quantum dots.[111] The strategy and results here open up the possibility of fully understanding, tuning, and enhancing PL signals from plasmonic nanostructures, which have many advantageous properties over SERS[97,112-115] and MEF[27,116-119] and use of PL nanoprobes based on plasmonic nanomaterials in a variety of applications including optics, biosensing, bioimaging, and energy applications. [55,120-123]

Figures
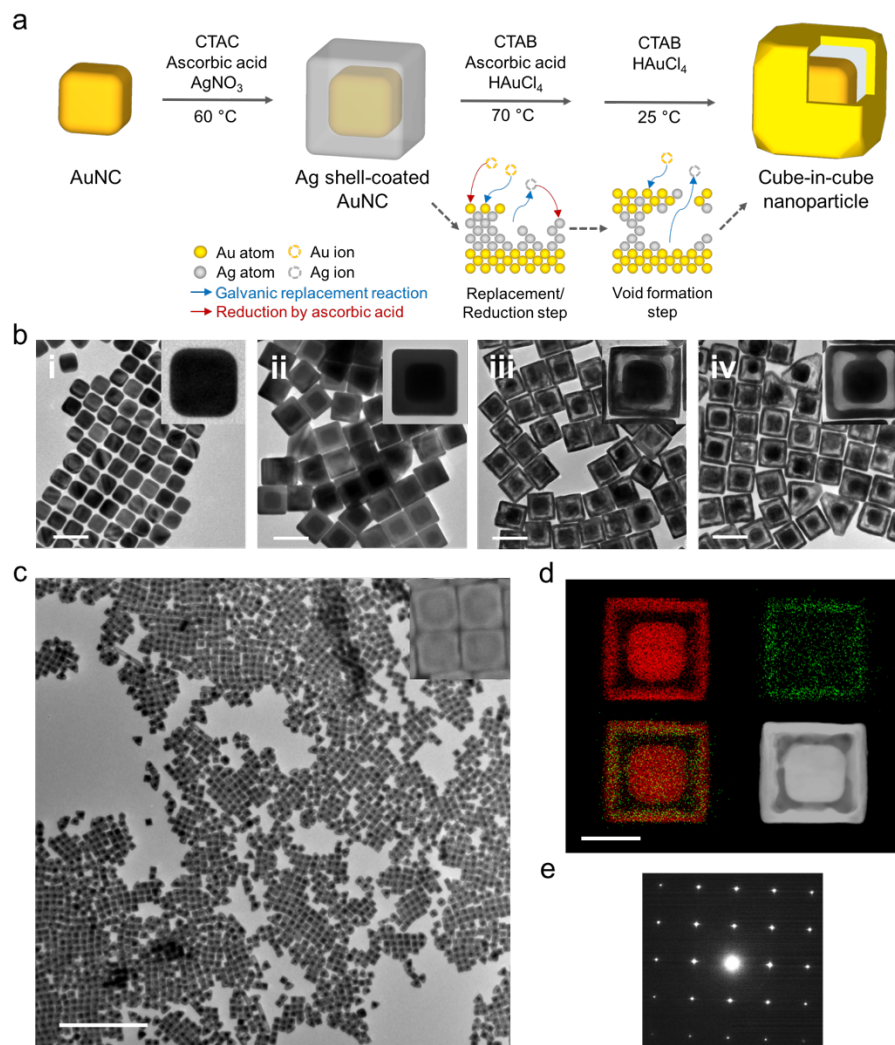
Figure 3.1. Synthesis and characterization of interior nanogap-engineerable CiC NPs. (a) Illustration of scheme for synthesizing CiC NPs through a controlled two-step GVF process. (b) TEM images corresponding to each step of synthesis procedure; the insets show representative single-particle images. The scale bar is 100 nm. (c) A large-area TEM image showing the final product in a high yield; the inset shows a representative SEM image of CiC NPs. The scale bar is 1 μm. (d) HAADF-STEM image (bottom right) and corresponding EDS maps. Red and green colors indicate elemental Au and Ag, respectively (images on top); the image on bottom left is a merged mapping image. The scale bar is 50 nm. (e) Electron diffraction pattern of a CiC NP showing the single-crystalline nature. The electron diffraction pattern was recorded by aligning the electron beam perpendicular to one face of the CiC NPs.

87
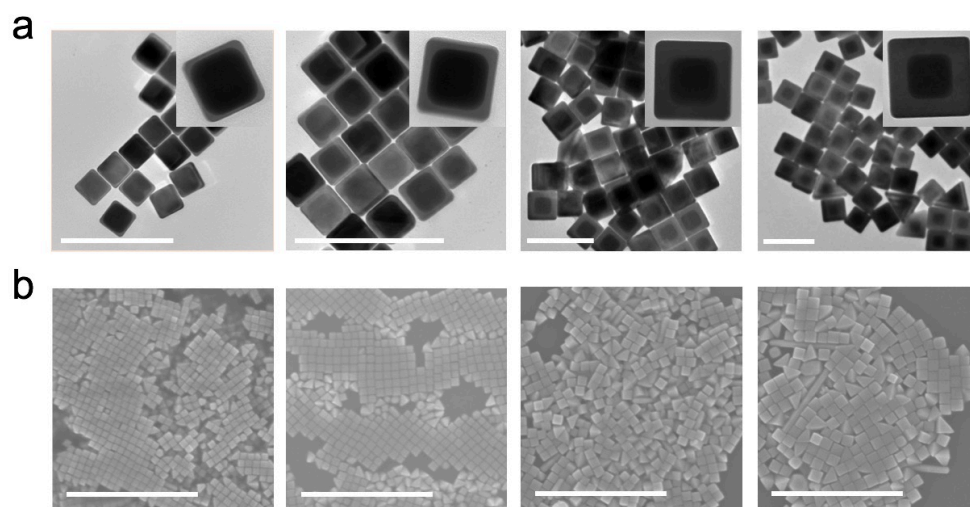
Figure 3.2. Precise control of Ag shell. TEM (a) and SEM (b) images of Ag shells with different thicknesses formed on AuNCs. Inset images show representative nanostructures. Scale bars in (a) and (b) are 200 nm and 1 μm, respectively.
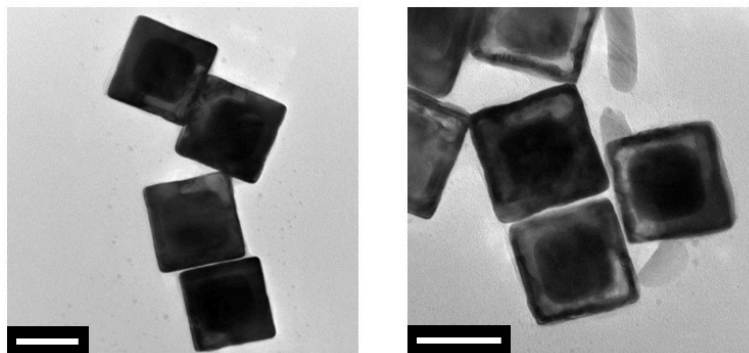
Figure 3.3. Observation of structural changes occurring during synthesis process. TEM images obtained after 4 min (left) and 8 min (right) from the start of the first galvanic replacement reaction. Scale bars are 50 nm.
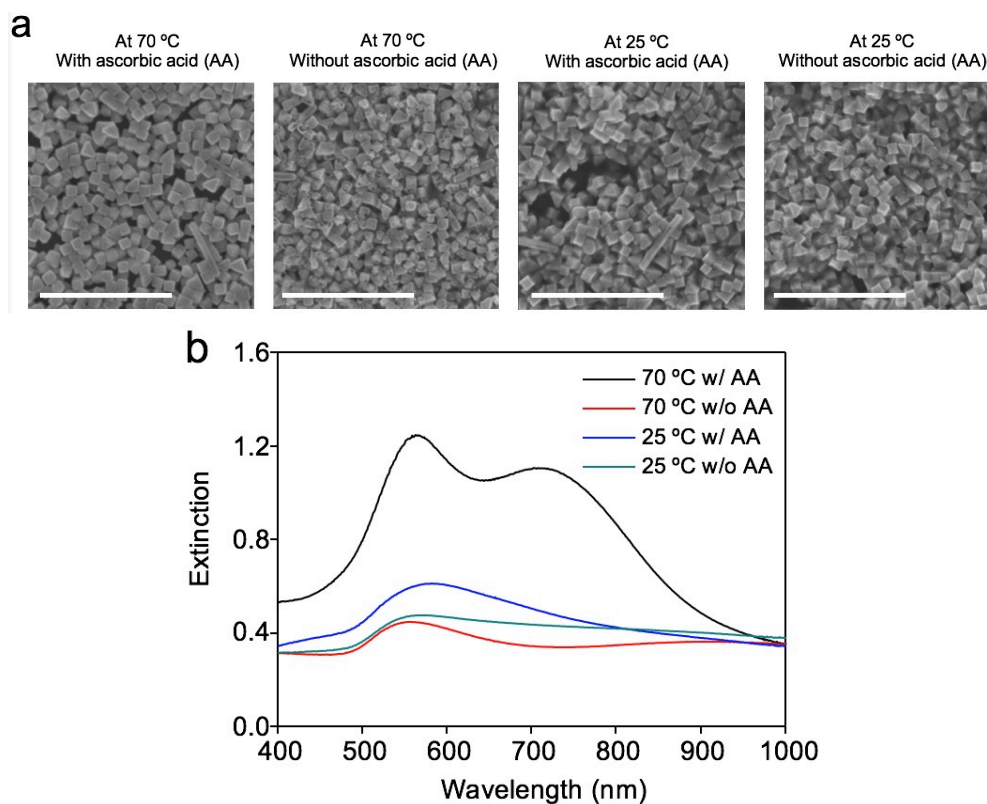
Figure 3.4. Effects of varying conditions on the controlled galvanic replacement reaction. (a) SEM images of products formed after the first galvanic replacement reaction under different conditions. Scale bars are 1 μm. (b) Corresponding UV−vis spectra.
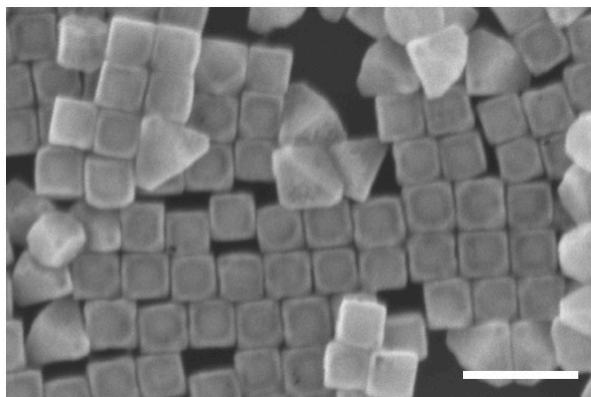
Figure 3.5. Structural morphology of CiCs with 9-nm gap. The SEM image shows slight truncations at the edges of the CiCs. Scale bar is 200 nm.
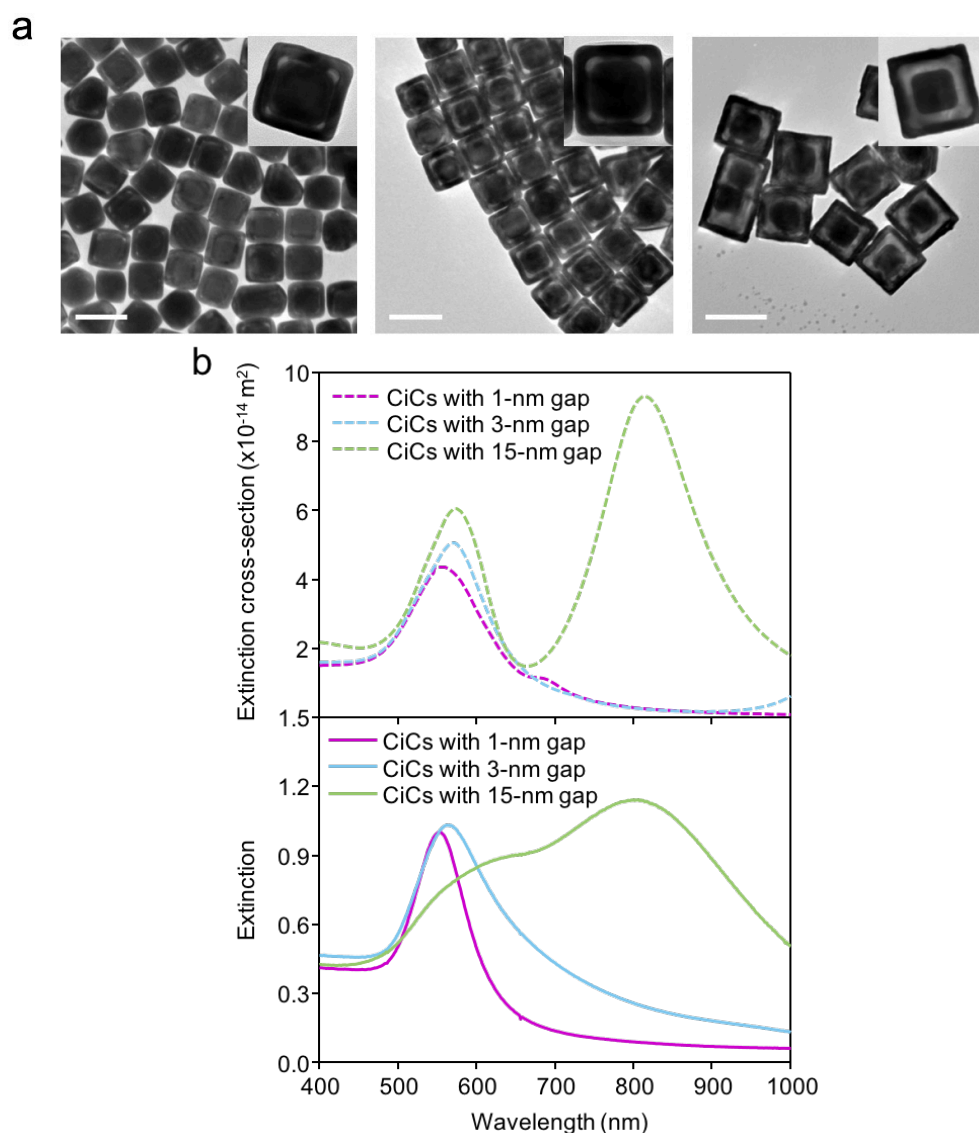
Figure 3.6. Controlling the interior gap of CiCs. (a) TEM images of different interior nanogap-engineered CiCs. Insets show representative images for each CiC type. Gap sizes are 1 nm (left), 3 nm (middle), and 15 nm (right), respectively. Scale bars are 100 nm. (b) Calculated (top) and experimental (bottom) extinction spectra of CiCs. In the case of the calculated spectrum for the CiCs with 3-nm gap, it is worth mentioning that these is an increase at approximately 1,000 nm, which is related to the bonding plasmon peak.
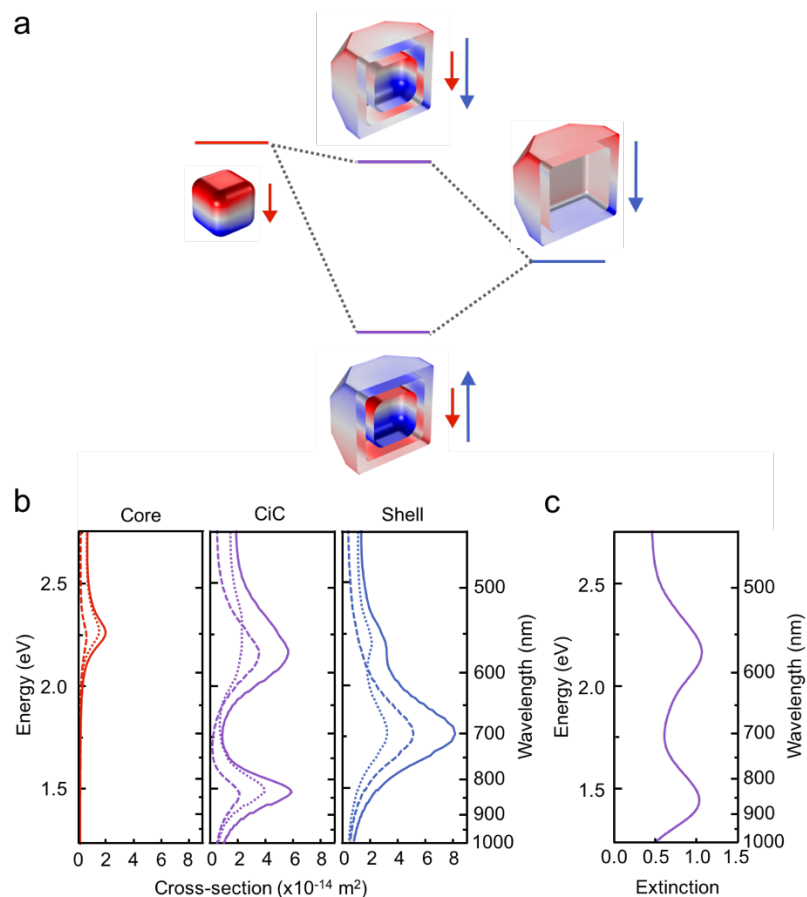
Figure 3.7. Plasmonic coupling model for CiC NPs. (a) A diagram of plasmon hybridization. Coupling between the elementary core and the shell generates two plasmon modes. Antiparallel coupling, which occurs at a lower energy level, exhibits a sub-radiant character, whereas parallel coupling shows a super-radiant character with an increased total dipole moment. Inset images are the surface charge distributions for the corresponding plasmon modes. (b) The calculated optical spectra of a core AuNC, shell, and CiC obtained via FEM simulations. Solid lines correspond to extinction, and dotted and dashed lines represent absorption and scattering, respectively. (c) Experimental UV−vis spectrum for 10 pM CiC suspension.
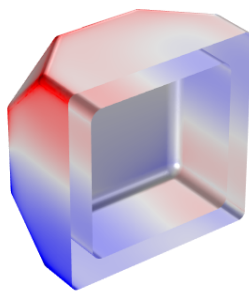
Figure 3.8. Surface charge distribution of the isolated shell corresponding to the shoulder peak at LSPR wavelength of ~560 nm.
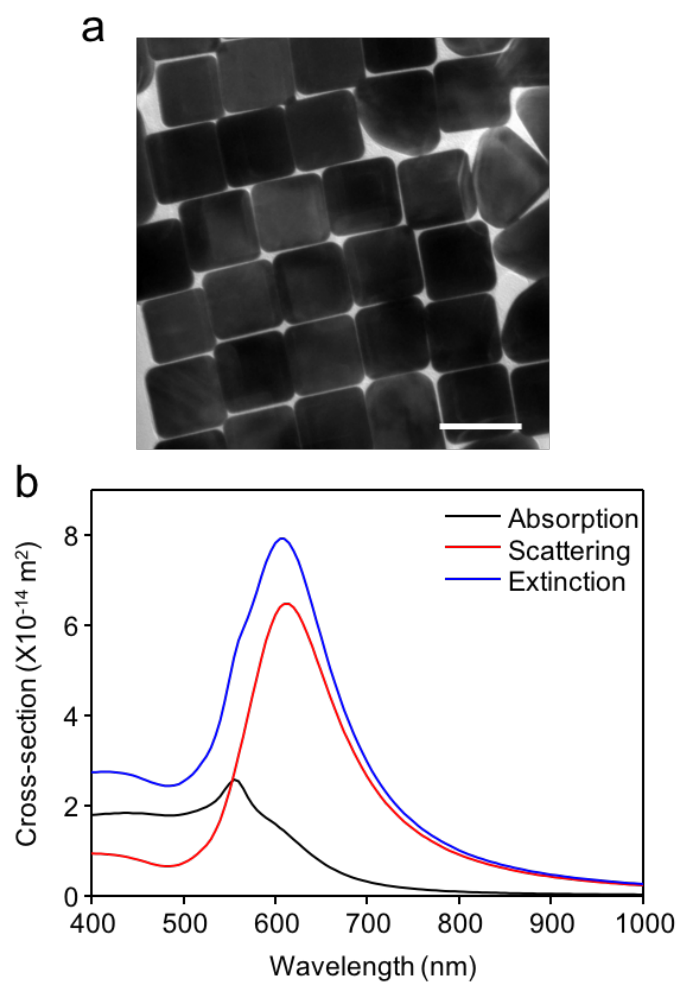
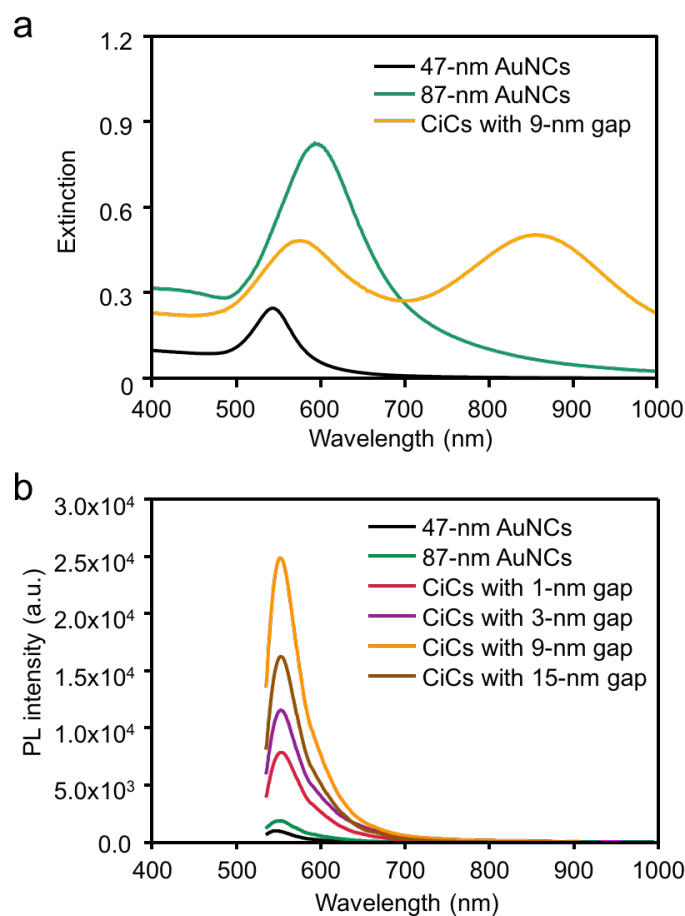**Figure 3.9.** TEM images (a) and calculated optical spectra (b) of 87-nm AuNCs. Scale bar is 100 nm.

Figure 3.10. Optical spectra of CiC NPs and two other AuNCs. (a) Extinction spectra obtained by UV−vis measurements. The edge lengths of 47 and 87-nm AuNCs coincide with those of the core cube of the CiCs and the CiCs, respectively. The concentration of the samples was fixed at 5 pM. (b) PL spectra of suspensions of 47 and 87-nm AuNCs and the CiCs with varying interior gap sizes measured using 532-nm excitation laser. All spectra were obtained for an exposure time of 10 s, 10× objective lens (N.A. 0.25), laser power density of 6.37×10^5 W/cm^2, and sample concentration of 10 pM.
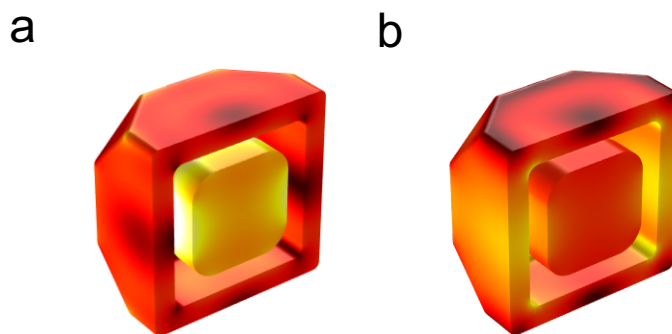
96

Figure 3.11. Cross-sectional images of electric field inside an CiC corresponding to the (a) visible peak and (b) near-infrared peak for each LSPR wavelength. The cross-section is perpendicular to the direction of light propagation. All figures use the same scale for the electric field intensity.
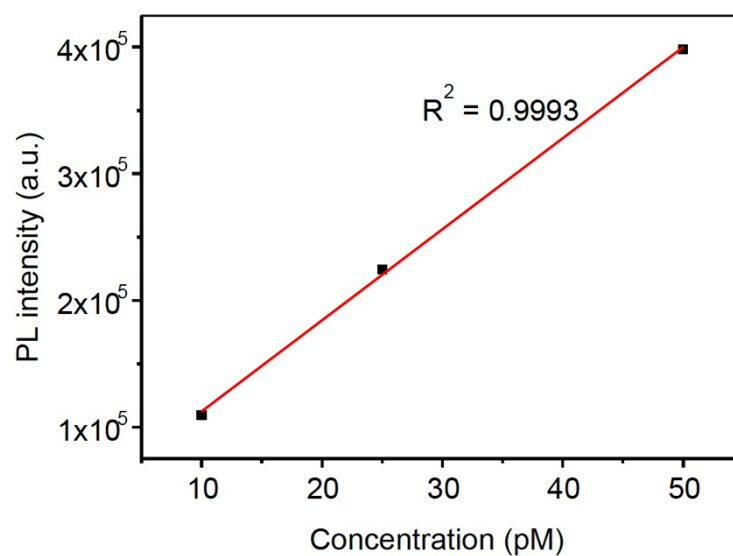
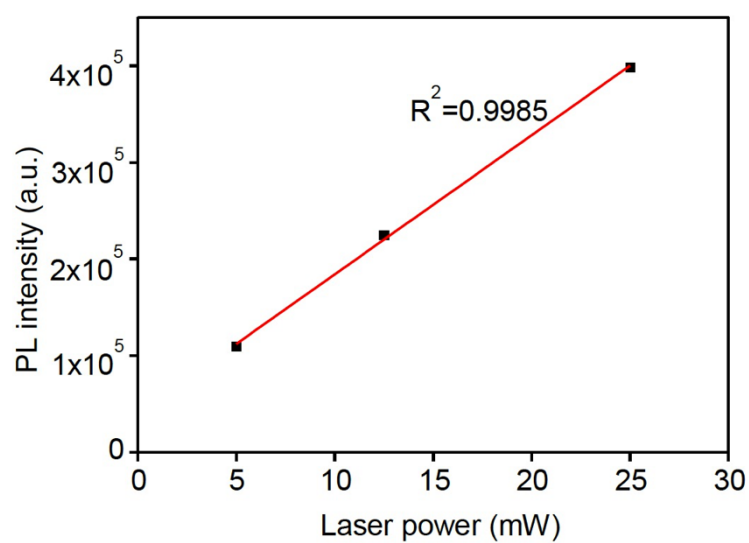**Figure 3.12.** Plot of photoluminescence intensity versus CiC concentration.

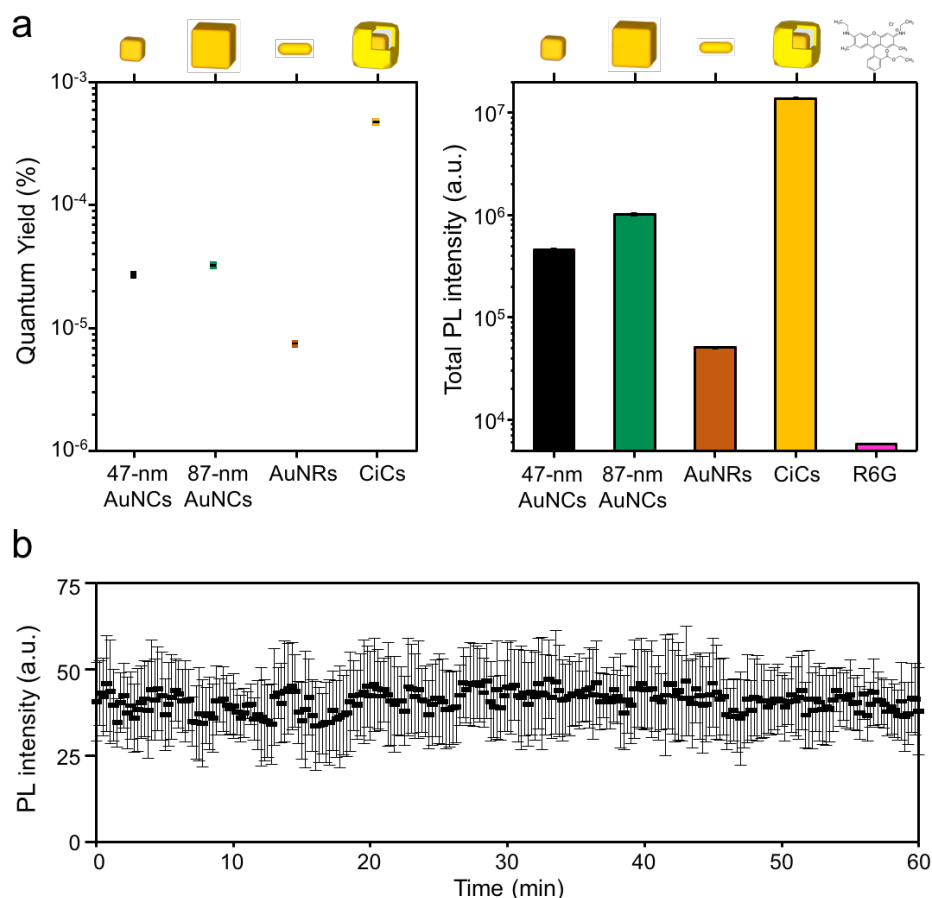**Figure 3.13.** Plot of photoluminescence intensity versus laser power.

Figure 3.14. Characteristics of the photoluminescence from the CiC NPs. (a) Comparison of the characteristics of the PLs from CiCs, 47 and 87-nm AuNCs, and AuNRs. The PL signals from ~13 × 46-nm AuNRs and R6G are shown as references. The QY and total PL intensity were obtained by integration from 535 to 1000 nm. The condition was same for all samples (the concentration was 10 pM). The spectra of the AuNRs and R6G were measured first using the concentrations of 300 and 100 pM, respectively, and then recalculated to the same concentration. Error bars are standard deviations for three independent measurements. (b) PL intensity for a single CiC measured using TIRF microscopy under continuous illumination from a 532-nm laser for 1 h. Images were taken every 30 s. The signal and error bars are averages for 20 nanoparticles.
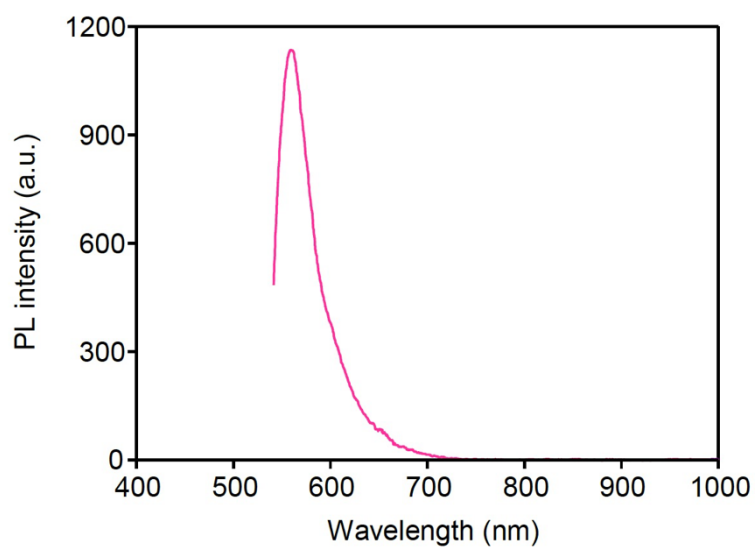
Figure 3.15. Photoluminescence spectrum of Rhodamine 6G. The conditions for measurements were similar to those for the CiCs; the exception was the concentration (100 pM).
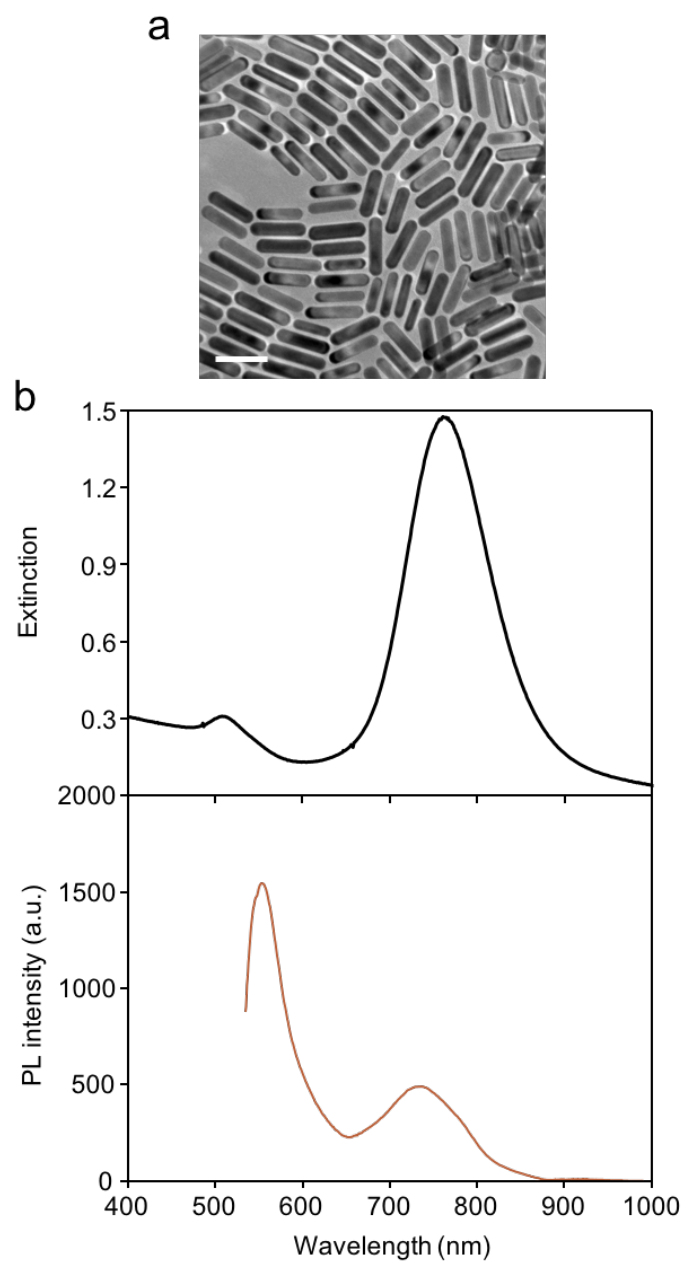
Figure 3.16. (a) TEM image of AuNRs. The dimension of AuNRs, determined from the TEM images, is 13 × 46 nm. Scale bar is 50 nm. (b) Extinction (top) and photoluminescence (bottom) spectra of AuNRs. The conditions for photoluminescence measurements were the same as those for the CiCs; the exception was the concentration (300 pM).
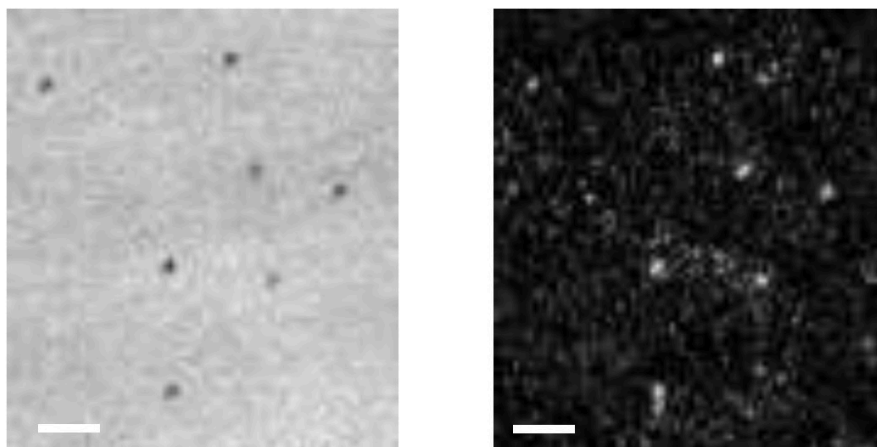
Figure 3.17. Images of CiCs obtained from the same area using (left) bright-field microscopy (left) and total internal reflection fluorescence microscopy (right). The CiCs in the two images match with each other. Scale bars are 2 μm.

Table

	I_{total} (a.u.)	Quantum Yield (%)
47-nm AuNC	$4.55 \times 10^{5} \pm 1.51 \times 10^{4}$	$2.73 \times 10^{-5} \pm 9.07 \times 10^{-7}$
87-nm AuNC	$1.02 \times 10^{6} \pm 1.89 \times 10^{4}$	$3.25 \times 10^{-5} \pm 6.02 \times 10^{-7}$
AuNR	$5.08 \times 10^{4} \pm 6.96 \times 10^{2}$	$7.53 \times 10^{-6} \pm 1.03 \times 10^{-7}$
CiC NP	$1.37 \times 10^{7} \pm 9.04 \times 10^{4}$	$4.78 \times 10^{-4} \pm 3.14 \times 10^{-6}$

Table 3.1. Molar absorption coefficient, integrated total photoluminescence intensities and QY values of various nanostructures. The standard deviations are based on three individual measurements.

Bibliography

1. Luk'yanchuk, B. *et al.* The Fano resonance in plasmonic nanostructures and metamaterials. *Nature Materials* **9,** 707–715 (2010).

2. Tittl, A. *et al.* Palladium-Based Plasmonic Perfect Absorber in the Visible Wavelength Range and Its Application to Hydrogen Sensing. *Nano Lett.* **11,** 4366–4369 (2011).

3. Linic, S., Christopher, P. & Ingram, D. B. Plasmonic-metal nanostructures for efficient conversion of solar to chemical energy. *Nature Materials* **10,** 911–921 (2011).

4. Kale, M. J., Avanesian, T. & Christopher, P. Direct Photocatalysis by Plasmonic Nanostructures. *ACS Catal.* **4,** 116–128 (2014).

5. Howes, P. D., Chandrawati, R. & Stevens, M. M. Bionanotechnology. Colloidal nanoparticles as advanced biological sensors. *Science* **346,** 1247390–1247390 (2014).

6. Li, J. *et al.* Plasmon-induced resonance energy transfer for solar energy conversion. *Nature Photonics* **9,** 601–607 (2015).

7. Park, J.-E., Kim, K., Jung, Y., Kim, J.-H. & Nam, J.-M. Metal Nanoparticles for Virus Detection. *ChemNanoMat* **2,** 927–936 (2016).

8. Kumar, A., Kim, S. & Nam, J.-M. Plasmonically Engineered Nanoprobes for Biomedical Applications. *J. Am. Chem. Soc.* **138,** 14509–14525 (2016).

9. Nam, J.-M., Oh, J.-W., Lee, H. & Suh, Y. D. Plasmonic Nanogap-Enhanced Raman Scattering with Nanoparticles. *Acc. Chem. Res.* **49,** 2746–2755 (2016).

10. Reguera, J., Langer, J., Jimenez de Aberasturi, D. & Liz-Marzán, L. M. Anisotropic metal nanoparticles for surface enhanced Raman scattering. *Chem. Soc. Rev.* **46,** 3866–3885 (2017).

11. Park, J.-E., Kim, M., Hwang, J.-H. & Nam, J.-M. Golden Opportunities: Plasmonic Gold Nanostructures for Biomedical Applications based on the Second Near-Infrared Window. *Small Methods* **1,** 1600032 (2017).

12. Bodelon, G., Costas, C., Pérez-Juste, J., Pastoriza-Santos, I. & Liz-Marzán,

L. M. Gold nanoparticles for regulation of cell function and behavior. *Nano Today* **13,** 40–60 (2017).

13. LaMer, V. K. & Dinegar, R. H. Theory, Production and Mechanism of Formation of Monodispersed Hydrosols. *J. Am. Chem. Soc.* **72,** 4847–4854 (1950).

14. Zheng, Y., Zhong, X., Li, Z. & Xia, Y. Successive, Seed-Mediated Growth for the Synthesis of Single-Crystal Gold Nanospheres with Uniform Diameters Controlled in the Range of 5-150 nm. *Part. Part. Syst. Charact.* **31,** 266–273 (2014).

15. Lee, Y.-J. *et al.* Ultrasmooth, Highly Spherical Monocrystalline Gold Particles for Precision Plasmonics. *ACS Nano* **7,** 11064–11070 (2013).

16. Huang, X., Neretina, S. & El-Sayed, M. A. Gold Nanorods: From Synthesis and Properties to Biological and Biomedical Applications. *Adv. Mater.* **21,** 4880–4910 (2009).

17. Zhang, Q. *et al.* Facet Control of Gold Nanorods. *ACS Nano* **10,** 2960–2974 (2016).

18. Personick, M. L. & Mirkin, C. A. Making Sense of the Mayhem behind Shape Control in the Synthesis of Gold Nanoparticles. *J. Am. Chem. Soc.* **135,** 18238–18247 (2013).

19. Dong, J., Zhang, Z., Zheng, H. & Sun, M. Recent Progress on Plasmon-Enhanced Fluorescence. *Nanophotonics* **4,** 1–19 (2015).

20. Li, M., Cushing, S. K. & Wu, N. Plasmon-enhanced optical sensors: a review. *Analyst* **140,** 386–406 (2015).

21. Kochuveedu, S. T. & Kim, D. H. Surface plasmon resonance mediated photoluminescence properties of nanostructured multicomponent fluorophore systems. *Nanoscale* **6,** 4966–19 (2014).

22. Zhou, C., Yang, S., Liu, J., Yu, M. & Zheng, J. Luminescent gold nanoparticles: A new class of nanoprobes for biomedical imaging. *Experimental Biology and Medicine* **238,** 1199–1209 (2013).

23. Drexhage, K. H. IV interaction of light with monomolecular dye layers. *Progress in optics* **12,** 163–232 (1974).

24. Geddes, C. D. & Lakowicz, J. R. Editorial: Metal-Enhanced Fluorescence. **12,** 121–129 (2002).

25. Li, J. *et al.* Spectral variation of fluorescence lifetime near single metal nanoparticles. *Sci Rep* **6,** 21349 (2016).

26. A, M. Photoluminescence of Metals. *Phys. Rev. Lett.* **22,** 185–187 (1969).

27. Akselrod, G. M. Probing the mechanisms of large Purcell enhancement in plasmonic nanoantennas. *Nature Photonics* **8,** 835–840 (2014).

28. Lakowicz, J. R. Radiative decay engineering 5: metal-enhanced fluorescence and plasmon emission. *Anal. Biochem.* **337,** 171–194 (2005).

29. APELL, P., MONREAL, R. & LUNDQVIST, S. Photoluminescence of Noble-Metals. *Physica Scripta* **38,** 174–179 (1988).

30. Ngoc, L. L. T., Wiedemair, J., van den Berg, A. & Carlen, E. T. Plasmon-modulated photoluminescence from gold nanostructures and its dependence on plasmon resonance, excitation energy, and band structure. *Opt. Express* **23,** 5547–5564 (2015).

31. BOYD, G. T., Rasing, T., Leite, J. R. R. & SHEN, Y. R. Local-field enhancement on rough surfaces of metals, semimetals, and semiconductors with the use of optical second-harmonic generation. *Phys. Rev. B* **30,** 519–526 (1984).

32. Mohamed, M. B., Volkov, V., Link, S. & El-Sayed, M. A. The `lightning' gold nanorods: fluorescence enhancement of over a million compared to the gold metal. *Chemical Physics Letters* **317,** 517–523 (2000).

33. Dulkeith, E., Niedereichholz, T., Klar, T. A. & Feldmann, J. Plasmon emission in photoexcited gold nanoparticles. *Phys. Rev. B* **70,** 205424 (2004).

34. Hu, H., Duan, H., Yang, J. K. W. & Shen, Z. X. Plasmon-Modulated Photoluminescence of Individual Gold Nanostructures. *ACS Nano* **6,** 10147–10155 (2012).

35. Hugall, J. T. & Baumberg, J. J. Demonstrating photoluminescence from Au is electronic inelastic light scattering of a plasmonic metal: the origin of SERS backgrounds. *Nano Lett.* **15,** 2600–2604 (2015).

36. Mertens, J., Kleemann, M.-E., Chikkaraddy, R., Narang, P. & Baumberg, J. J. How Light Is Emitted by Plasmonic Metals. *Nano Lett.* **17,** 2568–2574 (2017).

37. Lin, K.-Q. *et al.* Plasmonic photoluminescence for recovering native

chemical information from surface-enhanced Raman scattering. *Nature Communications* **8,** 14891 (2017).

38. Lin, K. Q. *et al.* Intraband Hot-Electron Photoluminescence from Single Silver Nanorods. *ACS ...* **3,** 1248–1255 (2016).

39. Yorulmaz, M., Khatua, S., Zijlstra, P., Gaiduk, A. & Orrit, M. Luminescence Quantum Yield of Single Gold Nanorods. *Nano Lett.* **12,** 4385–4391 (2012).

40. Fang, Y. *et al.* Plasmon Emission Quantum Yield of Single Gold Nanorods as a Function of Aspect Ratio. *ACS Nano* **6,** 7177–7184 (2012).

41. Rao, W., Li, Q., Wang, Y., Li, T. & Wu, L. Comparison of photoluminescence quantum yield of single gold nanobipyramids and gold nanorods. *ACS Nano* **9,** 2783–2791 (2015).

42. Wu, X. *et al.* High-photoluminescence-yield gold nanocubes: for cell imaging and photothermal therapy. *ACS Nano* **4,** 113–120 (2010).

43. Lumdee, C., Yun, B. & Kik, P. G. Gap-Plasmon Enhanced Gold Nanoparticle Photoluminescence. *ACS Photonics* **1,** 1224–1230 (2014).

44. Hu, H. *et al.* Photoluminescence via gap plasmons between single silver nanowires and a thin gold film. *Nanoscale* **5,** 12086–12091 (2013).

45. Wang, X. *et al.* Enhancement of Radiative Plasmon Decay by Hot Electron Tunneling. *ACS Nano* **9,** 8176–8183 (2015).

46. Huang, D. *et al.* Photoluminescence of a Plasmonic Molecule. *ACS Nano* **9,** 7072–7079 (2015).

47. Sivun, D. *et al.* Anticorrelation of Photoluminescence from Gold Nanoparticle Dimers with Hot-Spot Intensity. *Nano Lett.* **16,** 7203–7209 (2016).

48. Walsh, G. F. & Dal Negro, L. Engineering plasmon-enhanced Au light emission with planar arrays of nanoparticles. *Nano Lett.* **13,** 786–792 (2013).

49. Giljohann, D. A. *et al.* Gold Nanoparticles for Biology and Medicine. *Angew. Chem. Int. Ed.* **49,** 3280–3294 (2010).

50. Cobley, C. M., Chen, J., Cho, E. C., Wang, L. V. & Xia, Y. Gold nanostructures: a class of multifunctional materials for biomedical applications. *Chem. Soc. Rev.* **40,** 44–56 (2011).

51.   Murphy, C. J. *et al.* Gold Nanoparticles in Biology: Beyond Toxicity to Cellular Imaging. *Acc. Chem. Res.* **41,** 1721–1730 (2008).

52.   Xia, F. *et al.* Colorimetric detection of DNA, small molecules, proteins, and ions using unmodified gold nanoparticles and conjugated polyelectrolytes. *PNAS* **107,** 10837–10841 (2010).

53.   la Rica, de, R. & Stevens, M. M. Plasmonic ELISA for the ultrasensitive detection of disease biomarkers with the naked eye. *Nature Nanotech* **7,** 821–824 (2012).

54.   Qian, X.-M. & Nie, S. M. Single-molecule and single-nanoparticle SERS: from fundamental mechanisms to biomedical applications. *Chem. Soc. Rev.* **37,** 912–920 (2008).

55.   Qian, X. *et al. In vivo* tumor targeting and spectroscopic detection with surface-enhanced Raman nanoparticle tags. *Nat Biotechnol* **26,** 83–90 (2007).

56.   Niu, C., Song, Q., He, G., Na, N. & Ouyang, J. Near-Infrared-Fluorescent Probes for Bioapplications Based on Silica-Coated Gold Nanobipyramids with Distance-Dependent Plasmon-Enhanced Fluorescence. *Anal. Chem.* **88,** 11062–11069 (2016).

57.   Pang, Y., Rong, Z., Xiao, R. & Wang, S. 'Turn on' and label-free core−shell Ag@SiO2 nanoparticles-based metal-enhanced fluorescent (MEF) aptasensor for Hg2. *Sci Rep* **5,** 9451–8 (2015).

58.   Tabakman, S. M. *et al.* Plasmonic substrates for multiplexed protein microarrays with femtomolar sensitivity and broad dynamic range. *Nature Communications* **2,** 466 (2011).

59.   Zheng, Z. & Majima, T. Nanoplasmonic Photoluminescence Spectroscopy at Single-Particle Level: Sensing for Ethanol Oxidation. *Angew. Chem.* **128,** 2929–2933 (2016).

60.   Lu, G. *et al.* Plasmonic Sensing via Photoluminescence of Individual Gold Nanorod. *J. Phys. Chem. C* **116,** 25509–25516 (2012).

61.   Link, S. & El-Sayed, M. A. Shape and size dependence of radiative, non-radiative and photothermal properties of gold nanocrystals. *International Reviews in Physical Chemistry* **19,** 409–453 (2000).

62.   Dickerson, E. B. *et al.* Gold nanorod assisted near-infrared plasmonic

photothermal therapy (PPTT) of squamous cell carcinoma in mice. *Cancer Lett.* **269,** 57–66 (2008).

63. Loo, C., Lowery, A., West, J., Drezek, R. & Halas, N. J. Immunotargeted Nanoshells for Integrated Cancer Imaging and Therapy. *Nano Lett.* **5,** 709–711 (2005).

64. Song, J. *et al.* Ultrasmall Gold Nanorod Vesicles with Enhanced Tumor Accumulation and Fast Excretion from the Body for Cancer Therapy. *Adv. Mater.* **27,** 4910–4917 (2015).

65. Perrault, S. D., Walkey, C., Jennings, T., Fischer, H. C. & Chan, W. C. W. Mediating tumor targeting efficiency of nanoparticles through design. *Nano Lett.* **9,** 1909–1915 (2009).

66. Huff, T. B., Hansen, M. N., Zhao, Y., Cheng, J.-X. & Wei, A. Controlling the cellular uptake of gold nanorods. *Langmuir* **23,** 1596–1599 (2007).

67. Vreeland, E. C. *et al.* Enhanced Nanoparticle Size Control by Extending LaMer's Mechanism. *Chem. Mater.* **27,** 6059–6066 (2015).

68. Park, J.-E., Kim, J. & Nam, J.-M. Emerging plasmonic nanostructures for controlling and enhancing photoluminescence. *Chem. Sci.* **8,** 4696–4704 (2017).

69. Saha, K., Agasti, S. S., Kim, C., Li, X. & Rotello, V. M. Gold Nanoparticles in Chemical and Biological Sensing. *Chem. Rev.* **112,** 2739–2779 (2012).

70. Bodelon, G. *et al.* Detection and imaging of quorum sensing in Pseudomonas aeruginosa biofilm communities by surface-enhanced resonance Raman scattering. *Nature Materials* **15,** 1203–1211 (2016).

71. Kauranen, M. & Zayats, A. V. Nonlinear plasmonics. *Nature Photonics* **6,** 737–748 (2012).

72. Mukherjee, S. *et al.* Hot electrons do the impossible: plasmon-induced dissociation of H2 on Au. *Nano Lett.* **13,** 240–247 (2013).

73. Hou, W. & Cronin, S. B. A Review of Surface Plasmon Resonance-Enhanced Photocatalysis. *Adv. Funct. Mater.* **23,** 1612–1619 (2012).

74. Kim, M., Lin, M., Son, J., Xu, H. & Nam, J.-M. Hot-Electron-Mediated Photochemical Reactions: Principles, Recent Advances, and Challenges. *Advanced Optical Materials* **116,** 1700004 (2017).

75. Haggui, M. *et al.* Spatial confinement of electromagnetic hot and cold spots

in gold nanocubes. *ACS Nano* **6,** 1299–1307 (2012).

76. Lin, Q.-Y. *et al.* Strong Coupling between Plasmonic Gap Modes and Photonic Lattice Modes in DNA-Assembled Gold Nanocube Arrays. *Nano Lett.* **15,** 4699–4703 (2015).

77. Lee, D. & Yoon, S. Gold Nanocube–Nanosphere Dimers: Preparation, Plasmon Coupling, and Surface-Enhanced Raman Scattering. *J. Phys. Chem. C* **119,** 7873–7882 (2015).

78. Deeb, C. *et al.* Mapping the Electromagnetic Near-Field Enhancements of Gold Nanocubes. *J. Phys. Chem. C* **116,** 24734–24740 (2012).

79. Gao, B., Arya, G. & Tao, A. R. Self-orienting nanocubes for the assembly of plasmonic nanojunctions. *Nature Nanotech* **7,** 433–437 (2012).

80. Park, J.-E., Kim, S., Son, J., Lee, Y. & Nam, J.-M. Highly Controlled Synthesis and Super-Radiant Photoluminescence of Plasmonic Cube-in-Cube Nanoparticles. *Nano Lett.* **16,** 7962–7967 (2016).

81. Chikkaraddy, R. *et al.* How Ultranarrow Gap Symmetries Control Plasmonic Nanocavity Modes: From Cubes to Spheres in the Nanoparticle-on-Mirror. *ACS Photonics* **4,** 469–475 (2017).

82. Sun, Y. & Xia, Y. Shape-Controlled Synthesis of Gold and Silver Nanoparticles. *Science* **298,** 2176–2179 (2002).

83. Nicoletti, O. *et al.* Three-dimensional imaging of localized surface plasmon resonances of metal nanoparticles. *Nature* **502,** 80–84 (2013).

84. Tan, S. F. *et al.* Quantum plasmon resonances controlled by molecular tunnel junctions. *Science* **343,** 1496–1499 (2014).

85. O'Brien, M. N., Jones, M. R., Brown, K. A. & Mirkin, C. A. Universal Noble Metal Nanoparticle Seeds Realized Through Iterative Reductive Growth and Oxidative Dissolution Reactions. *J. Am. Chem. Soc.* **136,** 7603–7606 (2014).

86. Joo, S. W., Han, S. W. & Kim, K. Adsorption of 1,4-Benzenedithiol on Gold and Silver Surfaces: Surface-Enhanced Raman Scattering Study. *Journal of Colloid and Interface Science* **240,** 391–399 (2001).

87. Camargo, P. H. C., Rycenga, M., Au, L. & Xia, Y. Isolating and Probing the Hot Spot Formed between Two Silver Nanocubes. *Angew. Chem. Int. Ed.* **48,** 2180–2184 (2009).

88.   Peng, H.-C., Xie, S., Park, J., Xia, X. & Xia, Y. Quantitative Analysis of the Coverage Density of Br –Ions on Pd{100} Facets and Its Role in Controlling the Shape of Pd Nanocrystals. *J. Am. Chem. Soc.* **135,** 3780–3783 (2013).

89.   Meena, S. K. *et al.* The role of halide ions in the anisotropic growth of gold nanoparticles: a microscopic, atomistic perspective. *Physical Chemistry Chemical Physics* **18,** 13246–13254 (2016).

90.   Park, K., Koerner, H. & Vaia, R. A. Depletion-induced shape and size selection of gold nanoparticles. *Nano Lett.* **10,** 1433–1439 (2010).

91.   Lee, J.-H., Gibson, K. J., Chen, G. & Weizmann, Y. Bipyramid-templated synthesis of monodisperse anisotropic gold nanocrystals. *Nature Communications* **6,** 7571 (2015).

92.   Zhu, X. *et al.* Selective Pd Deposition on Au Nanobipyramids and Pd Site-Dependent Plasmonic Photocatalytic Activity. *Adv. Funct. Mater.* **23,** 1700016 (2017).

93.   Dovgolevsky, E. & Haick, H. Direct Observation of the Transition Point Between Quasi-Spherical and Cubic Nanoparticles in a Two-Step Seed-Mediated Growth Method. *Small* **4,** 2059–2066 (2008).

94.   Hartland, G. V. Optical studies of dynamics in noble metal nanostructures. *Chem. Rev.* **111,** 3858–3887 (2011).

95.   Le Ru, E. C., Blackie, E., Meyer, M. & Etchegoin, P. G. Surface enhanced Raman scattering enhancement factors: a comprehensive study. *J. Phys. Chem. C* **111,** 13794–13803 (2007).

96.   Fang, Y., Seong, N.-H. & Dlott, D. D. Measurement of the distribution of site enhancements in surface-enhanced Raman scattering. *Science* **321,** 388–392 (2008).

97.   Lim, D.-K. *et al.* Highly uniform and reproducible surface-enhanced Raman scattering from DNA-tailorable nanoparticles with 1-nm interior gap. *Nature Nanotech* **6,** 452–460 (2011).

98.   BOYD, G. T., YU, Z. H. & SHEN, Y. R. Photoinduced Luminescence From the Noble-Metals and Its Enhancement on Roughened Surfaces. *Phys. Rev. B* **33,** 7923–7936 (1986).

99.   Wackenhut, F., Failla, A. V. & Meixner, A. J. Multicolor Microscopy and

Spectroscopy Reveals the Physics of the One-Photon Luminescence in Gold Nanorods. *J. Phys. Chem. C* **117,** 17870–17877 (2013).

100. Cheng, Y. *et al.* Luminescence quantum yields of gold nanoparticles varying with excitation wavelengths. *Nanoscale* **8,** 2188–2194 (2016).

101. Yin, T. *et al.* Anomalous Shift Behaviors in the Photoluminescence of Dolmen-Like Plasmonic Nanostructures. **3,** 979–984 (2016).

102. Ma, Y. *et al.* Au@Ag Core-Shell Nanocubes with Finely Tuned and Well-Controlled Sizes, Shell Thicknesses, and Optical Properties. *ACS Nano* **4,** 6725–6734 (2010).

103. Hale, G. M. & Querry, M. R. Optical Constants of Water in the 200-nm to 200-µm Wavelength Region. *Appl. Opt., AO* **12,** 555–563 (1973).

104. Rioux, D. *et al.* An Analytic Model for the Dielectric Function of Au, Ag, and their Alloys. *Advanced Optical Materials* **2,** 176–182 (2014).

105. Sun, Y. & Xia, Y. Mechanistic Study on the Replacement Reaction between Silver Nanostructures and Chloroauric Acid in Aqueous Medium. *J. Am. Chem. Soc.* **126,** 3892–3901 (2004).

106. Prodan, E., Radloff, C., Nordlander, P. & Halas, N. J. A hybridization model for the plasmon response of complex nanostructures. *Science* **302,** 419–422 (2003).

107. Dicke, R. H. Coherence in Spontaneous Radiation Processes. *Phys. Rev.* **93,** 99–110 (1954).

108. Halas, N. J., Lal, S., Chang, W.-S., Link, S. & Nordlander, P. Plasmons in Strongly Coupled Metallic Nanostructures. *Chem. Rev.* **111,** 3913–3961 (2011).

109. Voisin, C., Christofilos, D., Loukakos, P. A. & Del Fatti, N. Ultrafast electron-electron scattering and energy exchanges in noble-metal nanoparticles. *Phys. Rev. B* **69,** 195416 (2004).

110. Varnavski, O. P., Goodson, T., Mohamed, M. B. & El-Sayed, M. A. Femtosecond excitation dynamics in gold nanospheres and nanorods. *Phys. Rev. B* **72,** 235405 (2005).

111. He, H., Xie, C. & Ren, J. Nonbleaching fluorescence of gold nanoparticles and its applications in cancer cell imaging. *Anal. Chem.* **80,** 5951–5957 (2008).

112. Cao, Y., Jin, R. C. & Mirkin, C. A. Nanoparticles with Raman spectroscopic fingerprints for DNA and RNA detection. *Science* **297,** 1536–1540 (2002).

113. Lim, D.-K., Jeon, K.-S., Kim, H. M., Nam, J.-M. & Suh, Y. D. Nanogap-engineerable Raman-active nanodumbbells for single-molecule detection. *Nature Materials* **9,** 60–67 (2009).

114. Li, J. F. *et al.* Shell-isolated nanoparticle-enhanced Raman spectroscopy. *Nature* **464,** 392–395 (2010).

115. Lane, L. A., Qian, X. & Nie, S. SERS Nanoparticles in Medicine: From Label-Free Detection to Spectroscopic Tagging. *Chem. Rev.* **115,** 10489–10529 (2015).

116. Pompa, P. P. *et al.* Metal-enhanced fluorescence of colloidal nanocrystals with nanoscale control. *Nature Nanotech* **1,** 126–130 (2006).

117. Bardhan, R., Grady, N. K., Cole, J. R., Joshi, A. & Halas, N. J. Fluorescence Enhancement by Au Nanostructures: Nanoshells and Nanorods. *ACS Nano* **3,** 744–752 (2009).

118. Ayala-Orozco, C. *et al.* Fluorescence enhancement of molecules inside a gold nanomatryoshka. *Nano Lett.* **14,** 2926–2933 (2014).

119. Abadeer, N. S., Brennan, M. R., Wilson, W. L. & Murphy, C. J. Distance and plasmon wavelength dependent fluorescence of molecules bound to silica-coated gold nanorods. *ACS Nano* **8,** 8392–8406 (2014).

120. McLeod, A. *et al.* Nonperturbative Visualization of Nanoscale Plasmonic Field Distributions via Photon Localization Microscopy. *Phys. Rev. Lett.* **106,** 037402–4 (2011).

121. Dasgupta, N. P. *et al.* 25th Anniversary Article: Semiconductor Nanowires - Synthesis, Characterization, and Applications. *Adv. Mater.* **26,** 2137–2184 (2014).

122. Tong, L., Wei, H., Zhang, S. & Xu, H. Recent Advances in Plasmonic Sensors. *Sensors* **14,** 7959–7973 (2014).

123. Dam, D. H. M. *et al.* Direct Observation of Nanoparticle–Cancer Cell Nucleus Interactions. *ACS Nano* **6,** 3318–3326 (2012).

초   록

플라즈모닉스는 플라즈모닉 물질을 사용하여 고도로 집중된 빛을 연구하고 이용하는 분야로 빛과 물질의 강한 상호 작용을 기반을 둔다. 빛의 파장보다 작은 크기의 플라즈모닉 나노 물질에 빛이 조사되면 금속의 자유 전자와 빛의 상호 작용으로 인해 국부적인 표면 플라즈몬 공명(localized surface plasmon resonance, LSPR)이라 불리우는 전자의 공명 운동이 일어나고 플라즈몬 나노 구조는 LSPR 특성에 강한 영향을 끼치기 때문에 플라즈몬 나노 구조를 효과적으로 이용하기 위해서는, 크기와 형태 제어가 가능한 고수율의 플라즈몬 나노 구조 합성이 중요하다. 금 나노 큐브는 비등방성의 구조체로 넓은 면과 뾰족한 꼭지점을 동시에 가지고 있어 화학적, 플라즈모닉 특성이 우수한 성질을 가지고 있다. 하지만 금 나노큐브의 플라즈모닉 특성을 재현적으로 생성하기 위해 필수적인 고수율의 합성법과 구조를 미세하게 조절하는 방법이 없었기 때문에 널리 사용되지 못했다.

이 논문은 큐빅 플라즈모닉 나노 구조의 합성을 이해, 제어하고 나아가 광학 특성을 조절, 향상시키는 과정을 소개한다. 우선 금속 기반 플라즈모닉스, 플라즈몬 나노 구조의 합성과 광 발광의 기초 등을 설명하고, 금 나노 큐브의 크기와 모서리 첨예도의 조절이 가능하며 매우 높은 수율로 형성하는 합성 방법을 보인다. 이 합성 전략은 나노입자 성장 과정에서 입자 표면 보호제를 미세하게 조정하여 원하는 구조를 합성하고 응집 과정을 이용해 합성 수율을 최대화하는 것에 기반한다. 나아가 강한 광발광 신호를 생성하는 플라즈몬 큐브 인 큐브 나노 입자 합성 결과를 소개한다. 큐브 인 큐브 나노 입자는 코어와 껍질의 플라즈모닉

115

커플링으로 인해 금속 나노구조를 이용해 보고된 결과 가운데 가장 강한 광발광 신호와 높은 양자 수율을 나타내었다. 마지막으로 우리는 플라즈몬 혼성화 이론을 기반으로 수퍼-래디언트 메커니즘을 제안하여 금속 나노 구조 내부의 플라즈모닉 커플링을 통한 광발광 강화를 설명하고 광학 특성을 분석하였다.